Novel Substrates for Graphene based Electronics

A Thesis Submitted to the University of Manchester for the Degree of Doctor of Philosophy in the Faculty of Engineering and Physical sciences

2012

By

Rashid Jalil

School of Physics and Astronomy

Contents

List of figures

List of Tables

Abstract

The application of the layered material hexagonal boron nitride for graphene based electronics is introduced and studied in this thesis. The by now well-known two dimensional material graphene is strongly considered a promising material for the future nano-world. An attractive feature of graphene is its very high electronic quality that is generally expressed by the mobility of its charge carriers. In this thesis, graphene devices were initially fabricated on oxidised silicon substrates. Transport measurements revealed no improvement in graphene's charge carrier mobility of ~ 5000-15,000 $cm^2V^{-1}s^{-1}$, which is far less than graphene's predicted intrinsic mobility of ~200,000 $cm^2V^{-1}s^{-1}$. This drew attention to use other, better, smoother and inert substrates for graphene to help improving the charge carrier mobility. Hexagonal boron nitride (hBN) has shown very remarkable first results in this regards. In the work presented here, boron nitride layers were isolated and identified successfully. Large boron nitride flakes were prepared on oxidized silicon by micromechanical cleavage, a conventional and routinely used technique for the fabrication of graphene and other two-dimensional materials and afterwards characterised by a number of techniques. Using optical microscopy, a low optical contrast of the thin and ultrathin boron nitride layers is observed. To allow for an unambiguous identification of the number of atomic layers, the use of optical filters and different thicknesses of oxide for the underlying oxidised silicon substrate are suggested to improve the optical contrast of these boron nitride layers. The thickness of boron nitride layers has been further studied by atomic force microscopy. Additionally, the use of Raman spectroscopy for counting the number of boron nitride is described. Raman studies show that the number of boron nitride layers is proportional to the corresponding Raman intensity. A characteristic Raman peak of boron nitride is observed at ~ 1366 cm^{-1}. The peak position and intensity for layers of various thicknesses with respect to bulk boron nitride is analysed carefully. An upward shift in frequency is seen in monolayer boron nitride whereas all other layers show a down shift. These thin boron nitride layers can be employed in making graphene boron nitride heterostruture. A precise flake transfer technique has been developed and is discussed in detail that has allowed for transferring graphene and other layered materials on any desired location with an accuracy of few microns. Two different flake transfer methods wet and dry were used for the fabrication of graphene heterostrutures. The graphene layers were successfully transferred on boron nitride substrate and TEM grids. Raman and AFM analysis of transferred flakes were also carried out to confirm the presence of graphene. A

comparison between wet and dry transfer methods and their possible applications in fabrication of artificial heterostrutures are discussed. The last part of this thesis deals with the study of micrometer ballistic transport in high mobility graphene samples at room temperature. The devices studied for this purpose were fabricated by transferring graphene on a hBN substrate and encapsulating it by another hBN crystal. Bend resistance measurements were employed to study the ballistic effects in our four terminal graphene boron nitride devices. A negative bend resistance is observed, showing that the devices exhibit room temperature ballistic transport over 1μm distance. A room temperature mobility of >100,000 $cm^2V^{-1}s^{-1}$ at $n \approx 10^{11}$ cm^{-2} is determined by analysing the field effect mobility. The role of diffusive scattering at the boundary of the samples in limiting the longitudinal conductivity of 1μm devices is described for higher $n \approx 10^{12}$ cm^{-2}. At low temperature, the mean free path reaches $l \approx 3$μm which translates into ultrahigh mobility for graphene. Our findings show a significant improvement in the mobility of graphene charge carriers when employing boron nitride substrates. Encapsulating the graphene devices with hBN is an even better addition, as it provides a barrier against environmental effects and can also serve as top dielectric for graphene boron nitride heterostrutures.

DECLARATION

No portion of the work referred to in the thesis has been submitted in support of an application for another degree or qualification of this or any other university or other institute of learning;

COPYRIGHT STATEMENT

i. The author of this thesis (including any appendices and/or schedules to this thesis) owns certain copyright or related rights in it (the "Copyright") and s/he has given The University of Manchester certain rights to use such Copyright, including for administrative purposes.

ii. Copies of this thesis, either in full or in extracts and whether in hard or electronic copy, may be made **only** in accordance with the Copyright, Designs and Patents Act 1988 (as amended) and regulations issued under it or, where appropriate, in accordance with licensing agreements which the University has from time to time. This page must form part of any such copies made.

iii. The ownership of certain Copyright, patents, designs, trade marks and other intellectual property (the "Intellectual Property") and any reproductions of copyright works in the thesis, for example graphs and tables ("Reproductions"), which may be described in this thesis, may not be owned by the author and may be owned by third parties. Such Intellectual Property and Reproductions cannot and must not be made available for use without the prior written permission of the owner(s) of the relevant Intellectual Property and/or Reproductions.

iv. Further information on the conditions under which disclosure, publication and commercialisation of this thesis, the Copyright and any Intellectual Property and/or Reproductions described in it may take place is available in the University IP Policy (see http://www.campus.manchester.ac.uk/medialibrary/policies/intellectual-property.pdf), in any relevant Thesis restriction declarations deposited in the University Library, The University Library's regulations (see http://www.manchester.ac.uk/library/aboutus/regulations) and in The University's policy on presentation of Theses

ACKNOWLEDGEMENTS

All praises for Allah the most Graceful and the most Beneficent. I am deeply grateful and humble to Him for blessing me with this opportunity of my academic career.

I am thankful to the University of Engineering & Technology, Lahore, Pakistan for supporting my PhD studies by awarding me scholarship under faculty development programme. Sincere thanks go to Prof. Khaleeq-ur-Rehman for his wise guidance and assistance in this regard. Without this scholarship, the completion of PhD project was impossible.

I want to express my deep gratitude to Prof. **Sir Andre Geim (Nobel Lauriat 2010),** my PhD supervisor for accepting me as his student, giving me a chance to work in his research group and world class Labs. I have learnt a lot from him, he is truly a role model for me. He has always been supportive, encouraging and kind to give his expert opinion regarding any problem I have faced during my studies.

I am thankful to my Advisor Prof. **Sir Kostantein Novoselov (Nobel Lauriat 2010)** for his valuable suggestion, guidance, support and care throughout PhD studies. He is an inspiring personality for me due to his hard work and dedication. His valuable guidance throughout the PhD studies are remarkable. Furthermore, I appreciate kind and helping response of my advisor Dr. Irina Grigorieva during my studies.

Sincere thanks go to Dr. Branson Belle, Dr. Soeren Neubeck, Dr. Rahul Raveendran-Nair, Dr. Peter Blake and Dr. Sasha Mayorov for proof reading this thesis.

I will like to extend my gratitude to all my group members especially Dr.Tariq Mohiuddin Mohammed Ghulam, Dr. Fredrik Schedin, Dr. Alexander Zhukhov, Dr. Branson Belle, Dr. Roman Gorbachov, Dr. Ibtsam Riaz, Dr. Rui Yang, Sheng Hu, Tu Jhih-Sian, Antonios Oikonomou, for their help and sharing their experimental skills in the clean room.

Further I am thankful to my wife Dr. Ibtsam Riaz for helping me at every step of my studies. Her patience and support were admirable and her efforts in this regards are tremendous. I love to thanks the support and prayers of my parents throughout this tenure. I must appreciate my son Muhammed Taha Jalil and my daughter Mariam Jalil for their love which was a continuous source of energy for me.

Last but not least I like to thank our family friends Mr. & Mrs. Ghulam Farid and Mr. & Mrs. Dr. Hafiz Muhammed Rafique for their moral support and cooperation during the stay in United Kingdom.

Chapter 1

Introduction

The discovery of graphene, a single layer of carbon atoms has added a new class of materials to the material family, that of one-atom thick two-dimensional materials. The isolation of two-dimensional graphene from the layered material graphite by using the simple and unusual method of repeated mechanical peeling by scotch tape has stunned the scientific world. The long debate about the existence of two dimensional materials has settled when scientists from the University of Manchester published their first paper about this novel material in 2004 [1]. This is one of the highly cited papers in the field of science and since then the number of published papers regarding graphene has increased until it reaches 4800 for year 2011 [2]. Due to the unique and remarkable properties of graphene not only materials science, particularly nanoscience and nanotechnology, but many other related fields of science and engineering have been attracted towards it, too.

The outstanding progress in graphene research and demonstration of proof-of-principle applications in short time has forced R&D organizations [3,4] and industries [5–8] to strongly focus on graphene in variety of areas. Graphene, the one atom thick material is easy to make and identify optically [9]. The method of micromechanical cleavage method for graphene fabrication has also opened the way for other two dimensional materials to be obtained from their layered parent materials, like BN [10], MoS_2 [11,12], BSCCO [11], $NbSe_2$ [11] and other dichalcogenides. These new materials are sought to be studied on their own or to be exploited in obtaining new materials of entirely different characteristics, when e.g. used in combination with other two-dimensional materials like graphene. The discovery of the existence of two-dimensional materials has thus opened a completely new field in fundamental research, for studying the intrinsic characteristics of artificial crystals composed of individual atomic layers, and applied fields when aiming at harvesting possible novel properties.

The study of the electronic properties of graphene reveal that it has a linear energy dispersion near the charge neutrality point in the electronic band structure and its charge carriers can be described as massless Dirac fermions [13]. Graphene shows an ambipolar field effect and charge carrier concentration can be tuned by varying the gate voltage, approaching up to $10^{13}cm^{-2}$ [1]. The high quality of graphene's crystal lattice results in room temperature ballistic transport over submicron length scales and a high charge carrier mobility that is weakly dependent on temperature [14]. An ultrahigh intrinsic mobility ~ 200,000 $cm^2V^{-1}S^{-1}$ of graphene is reported for suspended graphene devices [15]. All these fascinating properties make graphene an interesting and promising material for future technological applications.

The electronic properties of graphene arising from its unique band structure are different from other conventional two dimensional electronic systems. Efforts to utilize these properties of new material graphene in the world of electronics and device technology have so far been achieved in the form of certain graphene based transistors. High frequency graphene based transistors have been shown to be applicable for applications in imaging, radar, data communication and high frequency spectroscopy [16–19]. However, in the strongest industrial area of digital applications, the use of graphene for device electronics still needs much more advancement since the absence of an intrinsic band gap in graphene's electronic structure composes an as yet not overcome hurdle. Aside from technological applications, many phenomena of quantum physics can be probed and studied in detail in the excellent quality electronic system of graphene. The superior carrier mobility of graphene compared to other semiconductor materials is a quite attractive electronic feature. When using an oxidized silicon wafer as a substrate for graphene , the resulting room temperature charge carrier mobilities reach ~ 5,000-15,000 $cm^2V^{-1}s^{-1}$ [14]. Fabrication of graphene devices on oxidized silicon by employing standard lithography techniques is nowadays common practice. In this thesis, graphene devices employing these techniques were fabricated on oxidized silicon and their transport measurements show similar range of charge carrier mobility as reported.

The values given above are far below than predicted [20–22] and experimentally reported (for suspended graphene) [15] ultrahigh intrinsic mobility of graphene of ~200,000 $cm^2V^{-1}s^{-1}$. Studies on the factors limiting the intrinsic charge carrier mobility of graphene suggest that substrate effects taken as extrinsic limiting factors play a vital role in this

regard and minimizing these substrate induced factors can result in achieving required ultrahigh mobilities [20,23]. To tackle this problem, a clean, smoother and inert substrate for graphene is required. Some initial results related to the improvement in graphene electronic mobility by using hexagonal boron nitride (hBN) as a substrate for graphene [24] devices ignited research into studying graphene on this new substrate. Hexagonal boron nitride is a layered crystal, with each layer having boron and nitrogen atoms arranged in a honeycomb lattice arrangement in the same way as in graphite with carbon atoms. As the fabrication method of micromechanical cleavage has been successfully used to isolate layered materials other than graphite, including hBN [10,11] from bulk layered crystals, the use of hBN could possibly not only be limited to its use as an ultraflat bulk substrate for graphene, but also to use isolated monoatomic boron nitride sheets for applications like thin dielectric to gate graphene or as thin spacer in graphene-boron nitride heterostrutures to study various phenomena of physics like tunnelling or coulomb drag [25,26].

Here, studies were made to prepare and accurately identify BN layers of various thicknesses. Optical microscopy and Raman spectroscopy have proven to be very reliable and useful techniques to analyse single and few layer graphene [9,27]. We employed both tools to characterise the BN single- and multilayers fabricated on oxidized silicon. These BN layers were then used in combination with graphene to produce novel artificial heterostrutures with new and different (or 'yet unexplored') properties.

Graphene is frequently prepared on oxidized silicon substrate for various studies. But the application of graphene in a variety of fields including bendable and flexible electronics, for optical studies and TEM analysis however demands its fabrication on other substrates. This goal can be achieved by transfer of graphene from oxidized silicon to the required target or substrate. The fabrication of heterostrutures involving graphene and other layered materials like BN, MOS_2, BSCCO, WS_2 etc also requires the stacking of the constituting layers belonging to different materials by a controlled and a precise method.

Existing procedures for transferring graphene to various substrates do not need the required positioning accuracy and moreover, since they relay the use of solvents and chemicals [28,29]. They inevitably introduce contaminations to the resulting device. Also the samples for optical studies and for TEM analysis need the clean or even solvent free graphene transfer to minimize the effect of external impurities in graphene samples. The

same applies for the fabrication of heterostrutures like graphene boron nitride (GBN), where one requires the exact and clean transfer of alternating layers of these materials by repeated transfer. For a required geometry and size of a device, a transfer procedure with few micron accuracy is of crucial importance. A procedure meeting these needs, with still being user friendly and allowing for routine usage with high success rate has to be designed in this regard.

The design of a highly reliable transfer technique is the objective of the next part of the work presented here. The transfer of graphene and other layered materials is successfully performed using both dry and wet transfer procedures. The preparation of samples on a TEM grid as substrate for different materials including graphene, BN and MoS_2 is made possible by using this transfer procedure. The described procedure is very helpful in fabricating high-quality (exceptional electronic quality, low contamination) devices with various geometries, in particular heterostructure devices.

As a first example of using hBN as a substrate for graphene electronics, high mobilities of ~100,000 $cm^2V^{-1}S^{-1}$ at a charge carrier density ~ 10^{11} cm^{-2} have been reported [24,30]. The mean free path for these mobilities reaches up to 1μm. Going one step further and building a sandwich of alternating layers, the interaction between graphene and boron nitride layers in heterostructure devices can lead to interesting phenomena including ballistic transport [30]. For a better understanding of the electron transport characteristics in such devices and exploring their use in potential applications, the study of ballistic transport for these high mobility samples is very important and fascinating. Application wise, ballistic electron devices are popular in device industry, because of their high speed potential and enhanced functionality [31].

In this thesis, four terminal devices made from graphene sandwiched between two hBN crystals is used to study the ballistic effects. The transfer technique described in this work has been used to make graphene devices encapsulated by BN which greatly helps to increase the electronic quality of device by isolating it from external environment. Bend resistance measurements were employed to observe the ballistic effects. The negative bend resistance measured in our GBN devices proves that we indeed observe room temperature ballistic transport.

The breakdown of thesis is as follows. Chapter 2 provides an overview of graphene along with a description of its properties, particularly its electronic properties and the applications of graphene in science and technology. The routinely used fabrication and identification of graphene is also described. In Chapter 3, the experimental techniques used for graphene device fabrication are discussed. The electrical characterization of graphene devices and the results of these transport measurement are given.

Chapter 4 of this thesis is related to the insulator hexagonal boron nitride. Use of mechanical cleavage for preparation of large boron nitride flakes is described and the results of optical and Raman spectroscopy analysis are presented. The applications of boron nitride in graphene based electronics are also briefly discussed.

A highly reliable technique for accurate transfer of graphene and other layered materials is presented in chapter 5. Two different transfer methods such as wet and dry are given in detail along with examples of the transferred structures. A comparison of both methods and the corresponding applications of the transfer techniques are discussed in this chapter.

The study of ballistic transport in graphene boron nitride heterostrutures is presented in chapter 6 of the thesis. After a general overview of quantum conductance and ballistic transport, the bend resistance measurements for a given GBN heterostructure device is described and analysed. The fabrication of graphene boron nitride heterostructures using multiple steps of transfer and annealing are also given.

The work presented in the thesis is summarized in chapter 7. This chapter deals with the conclusions of the thesis and an outlook of the future work based on our study.

The work presented in Chapter 4 and chapter 6 has been published and in order for better presentation of the results the original papers are attached in each of these chapters.

Chapter 2

Fundamentals of Graphene

Graphene is the first two dimensional crystal discovered in 2004 at the University of Manchester [1]. Since its discovery it has not only shown extraordinary properties and exceptional quantum phenomena in solid materials but also established its importance and applications in the future technology. This chapter of the thesis will focus on the basics about graphene, including its structure, properties, preparation method, identification and applications. Figure 2.1 shows a 3D image of graphene sheet with hexagonally arranged carbon atoms.

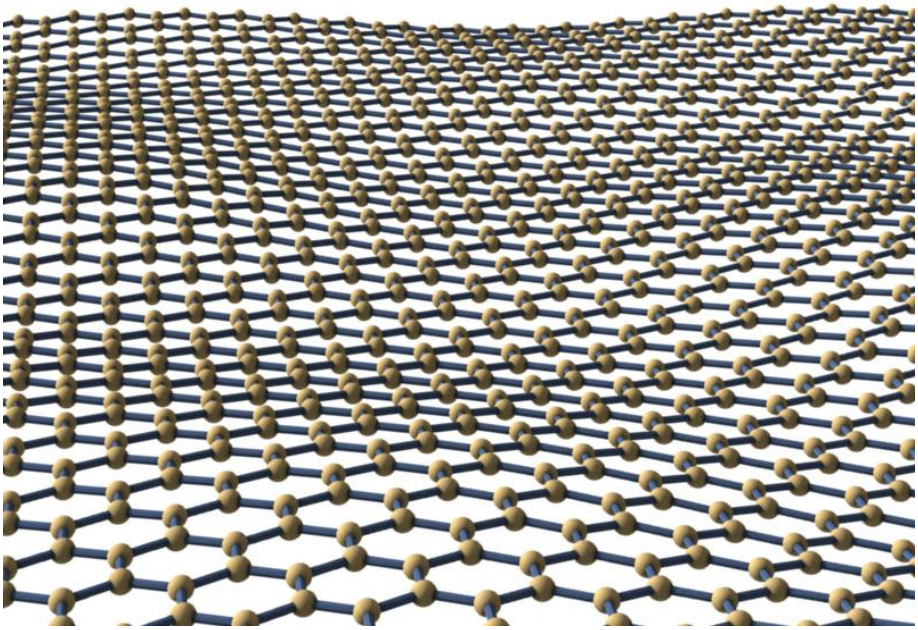

Figure 2.1: A 3D illustration of the graphene sheet.

Image of figure 2.1 is taken from:
http://www.jameshedberg.com/scienceGraphics.php?sort=graphene&id=graphene-3D-wavey

2.1 Introduction

The novel materials for the world of science and technology are always in high demand. The discovery of graphene has opened a new area of research and future applications. In this recently emerging field of graphene research many studies are aimed to find the solutions of scientific and technological limitations in the nano-world. The initial results obtained in this regard shows that graphene has a great potential to be a material for next generation.

The interest in graphene is due to many reasons including that it is a first true two dimensional material, can be used to explore many new phenomena that have never been studied before and can be exploited in a number of advance future applications. Graphene is still continue to surprise the scientists and researchers with its exceptional properties. The Nobel prize in 2010 was awarded to Prof. Andre Geim and Prof. Konstantin Novoselov "for groundbreaking experiments regarding the two-dimensional material graphene" [32].

Carbon belongs to fourth group of the periodic table and is one the most common or abundant element on the earth. It has a variety of crystalline forms that can be characterized on the basis of their symmetry and dimension. Some of the crystalline forms of carbon have been recently discovered including buckyballs, carbon nanotubes and graphene. Graphene is a planar allotrope of carbon with all carbon atoms forming covalent bonds in a single plane. The carbon atoms are hexagonally arranged forming a honeycomb lattice structure in graphene [13]. Graphene is the building block of all other graphitic materials [14]. The wrapped, rolled and sheet forms of the graphene are shown in Fig. 2.2.

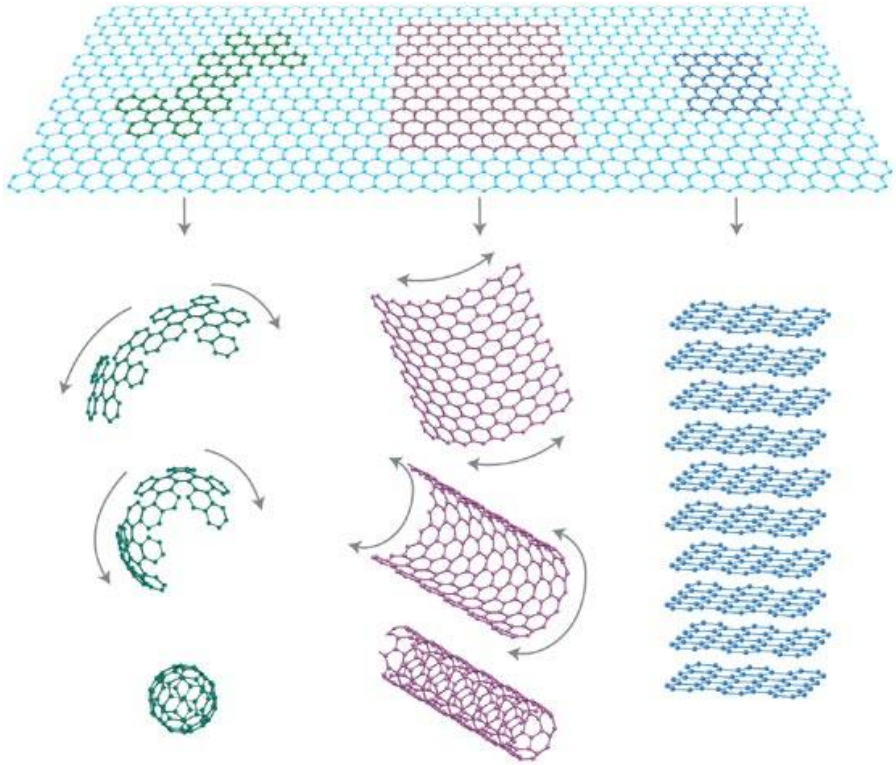

Figure 2.2: Graphene is a 2D building material for carbon materials of all other dimensionalities. It can be wrapped up into 0D buckyballs, rolled into 1D nanotubes or stacked into 3D graphite [14].

The sheets of graphene are stacked together to form bulk graphite which is abundantly found in nature and frequently used in many applications also two dimensional form of graphite (graphene) has been studied theoretically for many years as a model to understand other carbon materials [33,34]. But its existence has always been questioned in past. According to the theory, perfect two-dimensional crystals are thermodynamically unstable and should not exist in free space [35] .

Moreover, earlier attempts [36] to isolate single atomic layer of graphite was unsuccessful and could not fulfil the required goals.

In 2004,the scientists at the University of Manchester found a simple technique named micromechanical cleavage [1] for the isolation of graphene. In this method, graphite is continuously peeled by using an adhesive tape and then the tape is pressed onto an oxidised silicon wafer and subsequently removed to leave occasional graphene flake on the substrate.

With this discovery, gold rush of graphene research began to find the properties and different phenomena related to the new material graphene. The results of the initial studies showed that, graphene is a high quality crystalline material and the charge carriers could travel several thousand interatomic distances ~ 300 nm before scattering [1,13,14]. The excellent crystal quality of graphene result in high mobility of charge carriers ranging ~ 20,000 - 200,000 $cm^2V^{-1}S^{-1}$ [14,15,37] This charge carrier mobility of graphene is one order of magnitude higher than the silicon and other semiconductor materials [38].

2.2 Structure and fundamentals of Graphene

The remarkable properties of graphene, particularly electronic properties are the result of its unique electronic band structure. The study of the electronic band structure of graphene requires the understanding of its crystal lattice structure. Graphene has a honeycomb lattice structure formed by carbon atoms arranged hexagonally in two dimensional plane. Each carbon atom with its one *s* and two in-plane *p* orbitals forms strong SP^2 covalent bond with their three neighbouring carbon atoms providing strength to the graphene honeycomb structure. The electron in the z-direction of the p-orbital remains unpaired and is responsible for the high charge carrier conduction of graphene. The three in-plane σ orbitals and one out of plane (perpendicular to graphene sheet) π orbital formed by P_z electrons of carbon atoms are shown in Fig. 2.3.

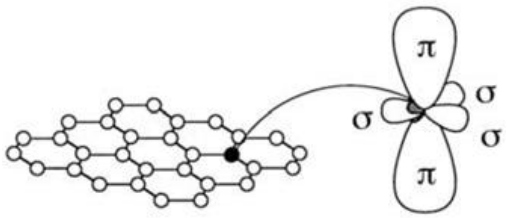

Figure 2.3: Graphene sheet of hexagonally arranged carbon atoms. Each carbon atom in graphene sheet forms three in-plane σ orbitals and one π orbital perpendicular to the graphene sheet [39] .

The crystal structure of graphene is highly symmetric with two equivalent sublattices formed by carbon atoms A and B (basis) attached to the hexagonal lattice in the Fig. 2.4(a). The basis vectors denoted by $\overrightarrow{a_1}$ and $\overrightarrow{a_2}$ in Fig. 2.4(a) can be used to represent any lattice point of the sublattice. The unit cell of the honeycomb lattice formed by these basis

vectors $\overrightarrow{a_1}$ and $\overrightarrow{a_2}$ consists of two carbon atoms. The basis vectors $\overrightarrow{a_1}$ and $\overrightarrow{a_2}$ in real space can be written as:

$$\overrightarrow{a_1} = \sqrt{3}a_{cc}\left(\frac{\sqrt{3}}{2}, \frac{1}{2}\right) \tag{2.1}$$

and

$$\overrightarrow{a_2} = \sqrt{3}a_{cc}\left(\frac{\sqrt{3}}{2}, -\frac{1}{2}\right) \tag{2.2}$$

Where a_{cc} = 1.42 Å is the carbon-carbon distance in graphene honeycomb lattice and $a = |\overrightarrow{a_1}| = |\overrightarrow{a_2}| = \sqrt{3}a_{cc} = \sqrt{3} \times 1.42 = 2.46$ Å is the lattice constant of graphene.

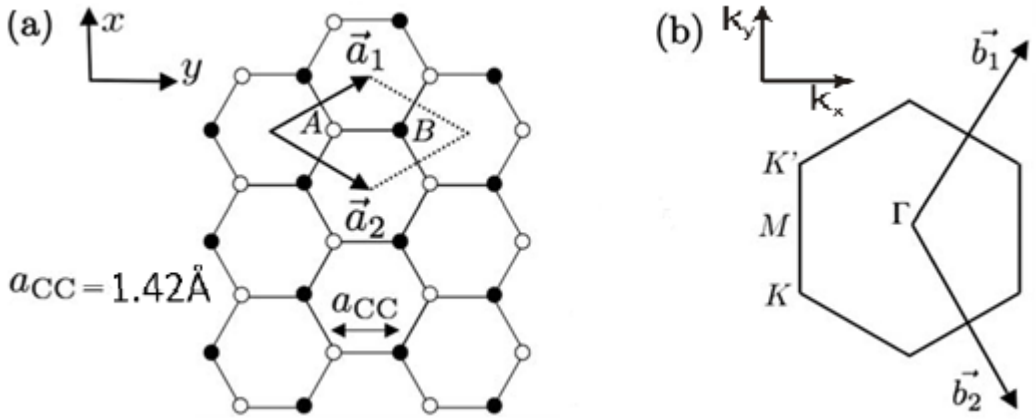

Figure 2.4: Honeycomb Lattice structure and hexagonal Brillouin zone of graphene. (a) Graphene's lattice structure having two carbon atoms A and B in unit cell formed by the lattice vectors $\overrightarrow{a_1}$and $\overrightarrow{a_2}$ where a_{cc} represents the nearest neighbouring distance. (b) Hexagonal Brillouin zone of graphene with Γ as centre and K,K′ as corners of the Brillouin zone. $\overrightarrow{b_1}$ and $\overrightarrow{b_2}$ are the reciprocal lattice vectors [40].

In Fig. 2.4(b) the basis vectors of reciprocal space $\overrightarrow{b_1}$ and $\overrightarrow{b_2}$ are shown and can be represented as:

$$\overrightarrow{b_1} = b\left(\frac{1}{2}, \frac{\sqrt{3}}{2}\right) \tag{2.3}$$

and

$$\overrightarrow{b_2} = b\left(\frac{1}{2}, -\frac{\sqrt{3}}{2}\right) \tag{2.4}$$

defining $b = \frac{4\pi}{\sqrt{3}a}$; where $a = \sqrt{3}a_{cc}$ and a_{cc} =1.42Å.

The hexagon in Fig. 2.4(b) is the brillouin zone of the honeycomb lattice of graphene. The center of the brillouin zone is represented by Γ whereas K and K´ are the two non-equivalent points at the corner of the brillouin zone of graphene The K and K´ points in the reciprocal space are given as:

$$\mathrm{K} = \mathrm{b}\left(\frac{1}{2}, \frac{1}{2\sqrt{3}}\right) \tag{2.5}$$

and

$$\mathrm{K'} = \mathrm{b}\left(\frac{1}{2}, -\frac{1}{2\sqrt{3}}\right) \tag{2.6}$$

The electronic band structure of graphene can be derived and explained well by applying tight binding model to the π orbital formed by P_z electrons of two carbon atoms in the unit cell of graphene. In 1947 P.R Wallace presented first tight binding description of graphene [33]. Solving the eigenvalue problem for Hamiltonian associated with these carbon atoms, the energy dispersion relation for the graphene can be derived. The energy dispersion relation obtained for the graphene is:

$$E^{\pm}(\vec{k}) = \pm\gamma_{\circ}\sqrt{1 + 4\cos\frac{\sqrt{3}k_x a}{2}\cos\frac{k_y a}{2} + 4\cos^2\frac{k_y a}{2}} \tag{2.7}$$

In the above expression of energy dispersion $\gamma_{\circ}$ is the transfer or hopping energy between nearest neighbour and commonly used value for $\gamma_{\circ}$ is 2.9 eV. The positive and negative energy branches in the expression indicate the valence (π) and conduction π* bands respectively and are shown in Fig. 2.5. The negative energy branch is fully occupied whereas the positive energy branch is empty. The Fermi energy separates occupied and empty states. In graphene this is the energy where valence and conduction band touch each other and is often referred to as the charge neutrality point or Dirac point

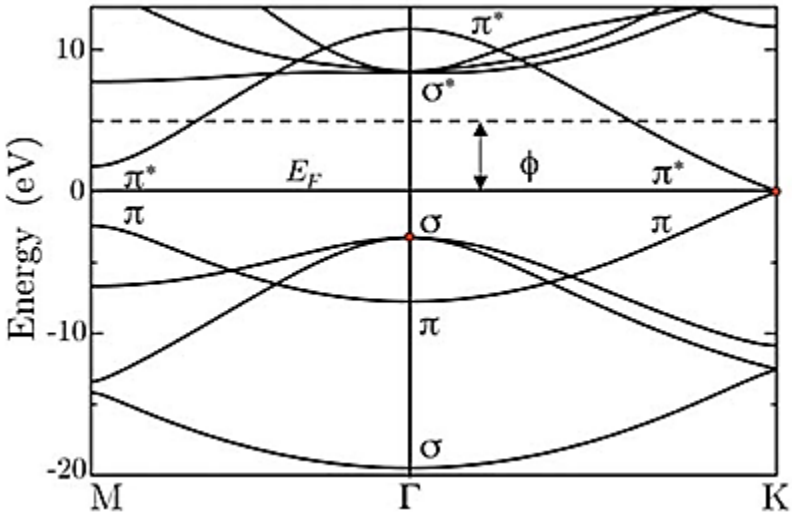

Figure 2.5: Electronic band structure of graphene at high symmetry points M, Γ, K of the hexagonal Brillouin zone. The valence (π) and conduction (π) bands touch each other at points K(Ḱ) of the brillouin zone [39].*

These points where energy bands π and π* touch each other are represented by K and K' in the Brillouin zone of graphene. The excitations near the K/K' points play the major role in graphene's properties. By expanding above equation near K/K' points, the energy dispersion is obtained as

$$E^{\pm}(\vec{k}) = \pm\hbar v_F|\vec{k}| \qquad (2.8)$$

Where $\vec{k}$ is the momentum taken at the point K/ K', $\hbar = \frac{h}{2\pi}$ and v_F is the Fermi velocity and is ~ 10^6 m/s for charge carriers in graphene.

The low energy electronic band structure of graphene forming cones near K/ K' points is presented in Fig. 2.5. The linear energy dispersion of graphene is extremely important and a number of graphene unique properties and many new phenomena are due to its linear band structure. The above energy dispersion relation of graphene charge carriers is related to the relativistic particle behaviour obeying Dirac relation.

2.3 Graphene Fabrication and Identification

Up till now several methods have been reported to produce graphene for research and application purposes. First ever used technique for graphene isolation was micromechanical cleavage [1]. This method can be used to obtain high quality graphene on substrate [11,13] or in free standing form i.e. graphene membranes [15,37,41]. In this method a thick graphite crystal is continuously peeled by using an adhesive tape and then the tape is pressed on to an oxidised silicon wafer to transfer occasional graphene flakes on to the substrate. Finally the tape is removed by using acetone. It is a highly reproducible method for high quality graphene preparation and can be used to prepare graphene on various substrates including oxidised silicon wafer, quartz, glass, plastic and mica. The size of the graphene flakes produced by this method ranges from few microns to millimetre depending on the size of the initial graphite used for cleavage and the cleaning process involved during fabrication process.

Another way of obtaining graphene layers includes the epitaxial growth either by thermal decomposition of silicon carbide (SiC) [42,43] or chemical vapour decomposition of hydrocarbons on metal substrate [44–46]. These methods were also introduced to meet the large area fabrication and to get maximum benefits of the remarkable properties of graphene. More recently growth of graphene on metallic substrates is getting more attention [46–49]. It is known for many years that graphene few layers or monolayers can be prepared on metallic substrates (Ni, Ru, Pt, Rh, Co, Ir, Cu, Pd) usually through the thermal decomposition of hydrocarbon at elevated temperature or surface segregation of C atom from bulk metal (by annealing carbon containing material) [50,51]. Ni and Cu have received more attention as a graphene substrate material [47,52,53] due to cost, excessive use and demand by semiconductor industry. Graphene on metal surfaces needs to be transferred to the other insulating substrates for its characterisation and transport measurements (e.g., an oxide layer) either by mechanical transfer or through solution processing [48,54–56] .

In order to produce large scale graphene for industrial applications, chemical route are available. In this method, graphite is chemically converted to graphite oxide [57]. Dispersion and exfoliation of graphite oxide in liquid phase produces sheets of graphene oxide (GO) whose reduction by thermal annealing or chemical reducing agents produces graphene [58,59]. The reduction of GO is an efficient and cost effective method for bulk scale graphene production. The reduction of oxide leave structural defects [60,61] and

efforts [62] are still in progress to have a liquid phase process with no such chemical reaction or high temperature treatment and also provides high yield of graphene.

2.3.1 Fabrication of Graphene by Micromechanical Cleavage

The graphene is usually produced on oxidized silicon wafers with 100/285/300/315nm oxide coatings on top. The reason for using oxidized silicon wafer as a substrate for graphene is the ease in identification of graphene flakes using optical microscope [9]. Current fabrication process of graphene using micromechanical cleavage involves different steps and are explained below

Pre-cleaning of substrate

High quality graphene can be obtained on the clean and smooth surface. In order to make the substrate more suitable for adhesion of graphene flakes and to minimize the surface contamination, the substrates need to be pre-cleaned before mechanical cleavage and deposition of graphite. The pre-cleaning consists of two procedures, regular solvent cleaning and oxygen plasma cleaning.

Micromechanical Cleavage of graphite

In mechanical cleavage, a piece of natural graphite is pressed onto adhesive tape and is repeatedly peeled. Due to layered structure of graphite, peeling process would separate the graphite layers and produce its thinner layers on tape. This thin graphite on the adhesive tape is transferred to the substrate by sticking this tape onto the substrate. The tape is then removed from the substrate either mechanically (using tweezers) or by solvents treatment. After the tape removal, the sample (substrate +graphite) is cleaned with solvents (Acetone, Isopropanol) to eliminate any contamination from the adhesive tape. The sample is then baked at high temperature ~$120C^0$ to remove the moisture content from it. There are still thick graphite flakes transferred on the substrate. Finally, in a piece of fresh adhesive tape is placed on to the sample and peeled to get rid of the thick graphite layers and to obtain graphene. The process can be described as the scheme below in Fig. 2.6.

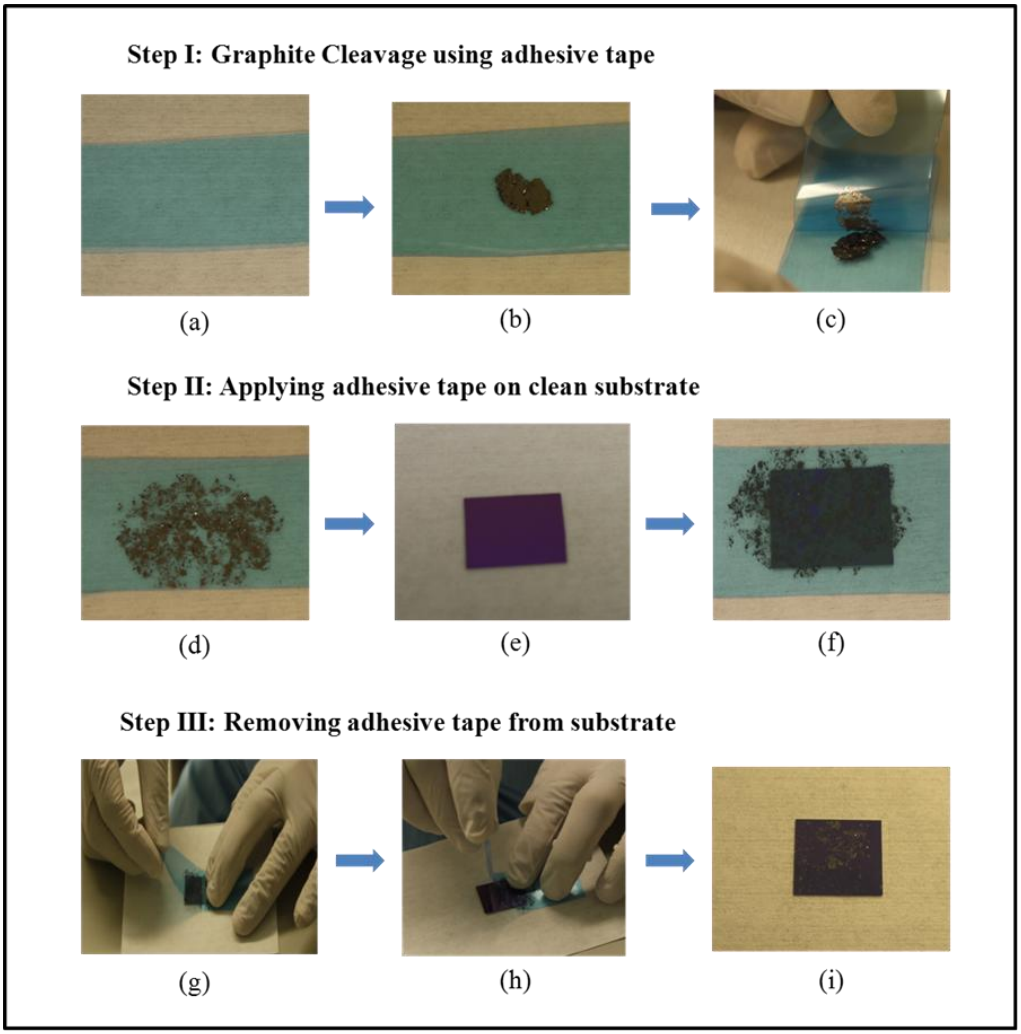

Figure 2.6: Step by step fabrication process of graphene by micromechanical cleavage.

2.3.2 Identification of Graphene

The clear identification of the graphene layers from thick graphite is very important in experimental research and technical applications. The graphene flakes prepared by above mentioned procedure of micromechanical cleavage can be identified by optical microscopy [9], Raman spectroscopy [27] and atomic force microscopy [1,14]. For frequent and quick analysis of graphene flakes, usually optical microscopy is used as an identification tool. It can be successfully used to locate and identify the graphene layers on a large area sample. As this identification method is intensive to measure the thickness of graphene layers and other related topographical details so atomic force microscopy can be useful in this regard. But due to variation in thickness (0.4 nm to 1 nm) of monolayer

graphene measured on oxidized silicon [63] and its low throughput in terms of time it cannot be used as an accurate and frequent identification tool. But Raman spectroscopy is found to be a powerful technique for unambiguous identification of the graphene layers.

Graphene gives good optical contrast on oxidized silicon wafer with particular oxide thickness even though it is one atom thick layer. The optical contrast of the graphene is due to interference effect and it increases with the number of layers [9]. The optimum optical contrast of graphene flakes can be obtained on top of silicon with 100 nm and 300 nm oxide coatings as shown in Fig. 2.7.

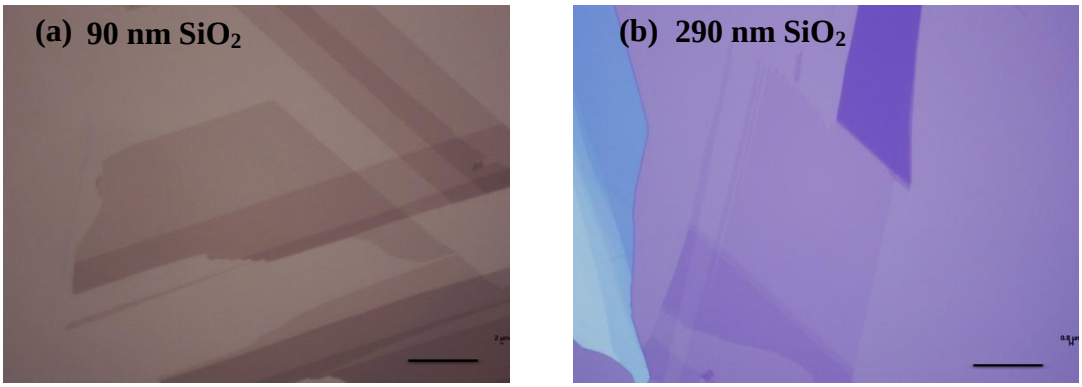

Figure 2.7: Optical images of the mechanically cleaved graphene on 90 nm (a) and 290 nm (b) oxidized silicon wafers. Images are taken in white light at 50x. with scale bar of 10µm.

Graphene obtained on substrates other than SiO_2 can also be examined under the optical microscope if visibility condition of interference is satisfied. Although optical microscopy can be successfully used to locate and identify the graphene flakes on number of different substrates but for the conclusive evidence, other experimental techniques need to be applied. Atomic force microscopy (AFM) is one of them and is quiet helpful in determining the thickness, roughness and frictional studies of the graphene layers. It works on the basis of the tip (mounted on the cantilever) interaction with sample as it scanned across the surface of the sample to be analyzed.

In order to distinguish between the mono, bi, tri and few layers of the graphene by atomic force microscopy, the step height of these layers from the substrate is taken. For a monolayer graphene step-height from the substrate is usually higher than the expected value of 0.334nm. Therefore it is counter checked by step-height between a monolayer and bilayer on the substrate. In Fig. 2.8 AFM image of graphene layers on 290 nm SiO_2 prepared by micromechanical cleavage is shown. Single, bi and trilayer regions are represented by 1L,2L and 3L.

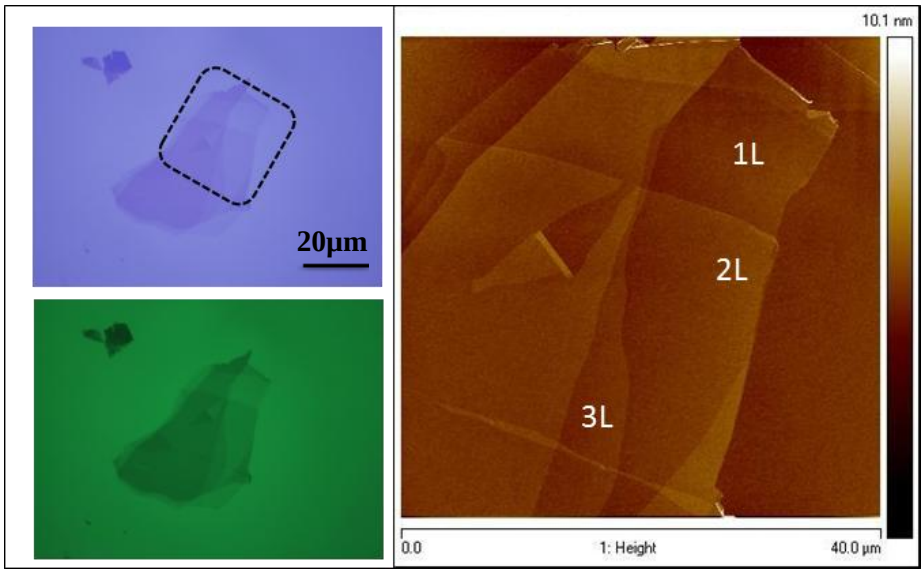

Figure 2.8: Optical image of graphene flake prepared by mechanical cleavage on 290 nm SiO_2 (left), Atomic Force Microscopy image of the same flake (right).

Due to ambiguity in measured thickness of graphene by AFM, its low throughput and tip - sample interaction that can destroy graphene samples, Raman spectroscopy is widely used technique for graphene identification.

The Raman spectrum of graphene monolayer show distinct features that can be used to differentiate monolayer from few layer graphene. Therefore Raman spectroscopy can be used for precise counting the number of graphene layers. The Raman spectra of graphene and graphite taken from ref. [27] is shown in Fig. 2.9

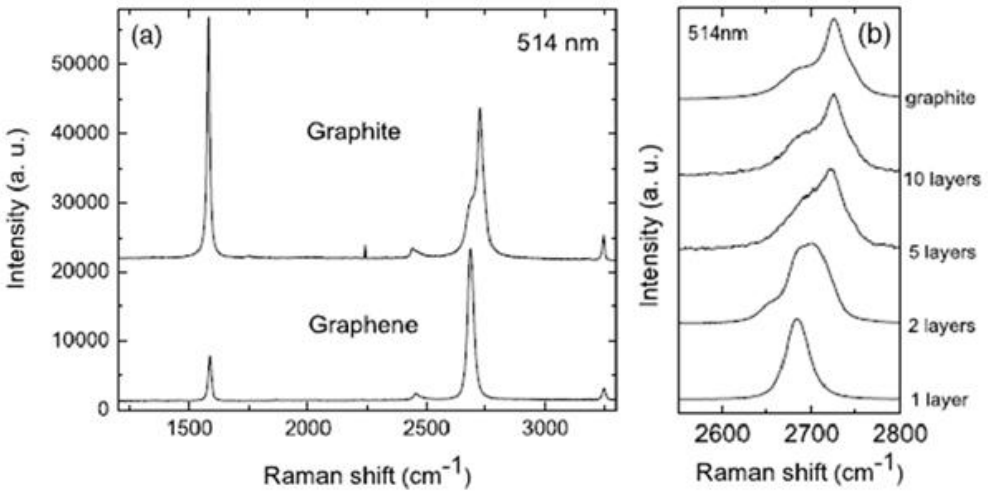

Figure 2.9: Raman spectrum of graphene monolayer and graphite using 514 nm excitation source. (a) Raman peaks are at 1580 cm $^{-1}$ (G-peak) and 2700 cm^{-1} (2D peak). (b) The evolution of 2D peak (used for layer counting) with the graphene layers.

The main peaks in the graphene and graphite Raman spectra are at 1580 cm^{-1} and 2700 cm^{-1} called as G peak and 2D peak respectively. The comparison of Raman spectra of graphene and graphite in Fig. 2.9 (a) shows that Raman G peak intensity of graphene and graphite are comparable (above plot is rescaled to have similar height of 2D peak) . The other prominent feature of graphene Raman spectra is 2D peak which can be used to count the number of graphene layers as line shape of the 2D peak changes with the number of graphene layers. The evolution of the Raman 2D peak with the number of graphene layers is presented in Fig. 2.9 (b). The 2D peak of graphene is a single sharp peak with intensity much higher than the G-peak. When compared to graphite, its 2D peak splits in two components and has intensity less than the G- peak intensity. The line shape of bilayer graphene is also different from single layer graphene and bulk graphite. In Fig. 2.9 the 2D peak of bilayer graphene is an upshifted peak which is splitted into four sub components and is broader than the single layer 2D peak. Therefore Raman spectrum of graphene layers can be successfully used to differentiate graphene single layer from bilayer and few-layer graphene.

2.4 Extraordinary Properties of Graphene

In the new class of two dimensional materials, graphene is the first material which has been isolated and studied experimentally. Graphene shows unique electronic, optical, mechanical, thermal and many other properties that can be well utilized in advanced future applications. Because of all these properties graphene has become the center of attraction in various research fields in the last decade. Even now all graphene properties has not been utilized in expected practical application because of certain limitations (e.g absence of bandgap for digital electronic applications and mass production of defect free graphene for various commercial applications) but still research is in progress to overcome these constraints. Also many new phenomena observed in graphene provide an opportunity to researchers to study exciting physics.

Graphene is a novel material with exceptional good electronic properties. It has an incredible strength of being a suitable material for modern electronics. First ever study of transport properties of 2D exfoliated graphene were reported in 2004 by K.S Novoselov [1]. Graphene exhibits an ambipolar electric field effect such that the gate voltage V_g tune the Fermi energy E_F and ultimately change carriers between holes and electrons as shown in Fig. 2.10 (a) with the concentration as high as about ~10^{13} cm^{-2}. By applying the gate voltage to the graphene, the conductivity σ is found to be linear with the gate voltage V_g both for holes and electrons as presented in Fig. 2.10 (b). The mobilities of the charge carriers are usually found to be varying between 5,000- 15,000 cm^2/Vs on Si/SiO_2 at room temperature [14]. The charge carrier concentration and the mobility dependence on the grate voltage can be seen in the Fig. 2.11.

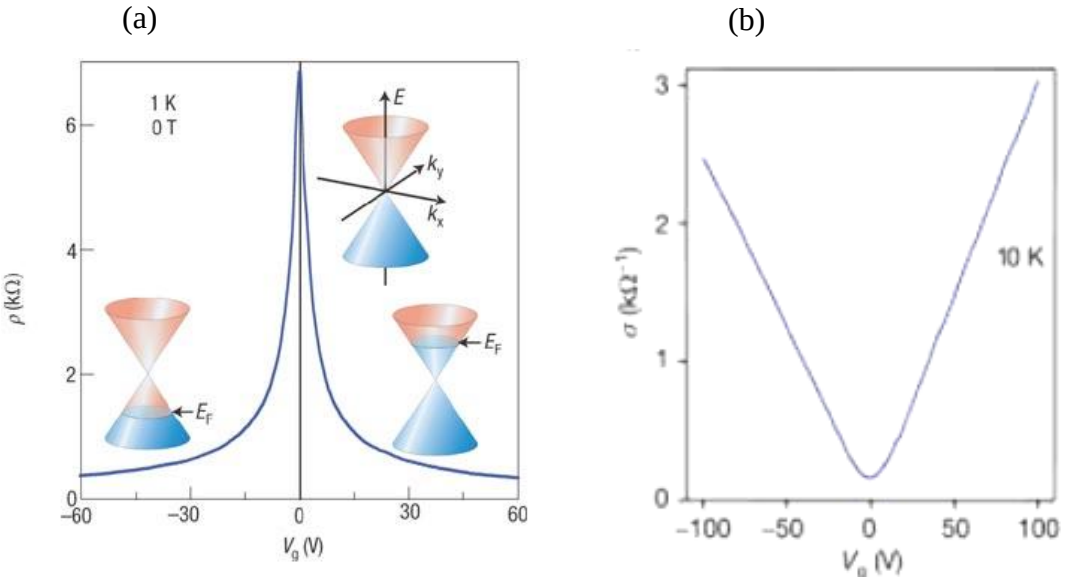

Figure 2.10: (a) Ambipolar electric field effect in Single layer graphene. Inset of the figure show the conical energy spectrum of graphene indicating the position of the Fermi energy E_F changing with the gate voltage V_g [14]. (b) Graphene conductivity as a function of gate voltage V_g at 10K [13].

The mobility μ is found to be weakly dependent on temperature showing that the scattering due to surface charge impurity, phonons or surface roughness is the main limiting source of the mobility and can be improved to higher values . By reducing the mobility limiting factors mainly originating from the substrate surface, the charge carriers mobility for suspended graphene exceeds up to 200,000 cm^2/Vs [15] at low temperature. Recently using boron nitride as an inert substrate for graphene, the mobility of graphene has increased 10 times at room temperature and reaches to 275,000 cm^2/Vs at low temperature [64]. Also ballistic transport on the submicron level (0.3 μm at 300K) is reported in both electrically and chemically doped graphene devices [65].

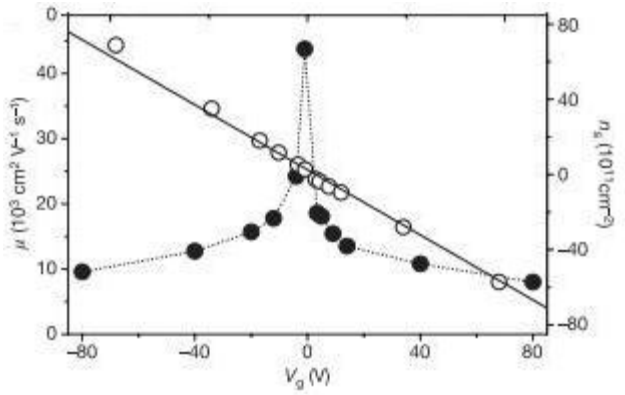

Figure 2.11: Charge carrier density (open circles) and the mobility (filled circles) of the graphene as a function of the gate voltage. The solid line is for the estimated charge induced by the gate voltage V_g [66].

The study of the electronic properties of the graphene also reveals some other interesting phenomena in this two dimensional material including minimum charge carrier conductivity $б_{min}$ [14] and Quantum Hall Effect at room temperature [66,67] due to linear dispersion and electron hole symmetry of graphene near the charge neutrality point.

Conductivity of graphene does not vanishes at the neutrality point (as electrons and holes vanishes when the Fermi energy goes to zero) shown in Fig. 2.10 (b) rather exhibits a minimum conductivity value close to quantum conductivity $б_{min} = e^2/h$ for its carriers [14]. Many theories predicts this type of $б_{min}$ for Dirac fermions, whereas such a low conductivity leads to the metal insulator transition at low T which is not observed in generic graphene but recently this phenomena is observed in double layer graphene heterostrutures device [26].

The $б_{min}$ at the neutrality point is due to the reason that in graphene near the neutrality point, electrons and the holes puddles (with zero average density) are produced as result of charge inhomogeneity (chemical or substrate induced) and are taking part in the conductivity [14]. Macroscopic (larger than carrier mean free path) and microscopic (few nanometres) inhomogeneity both contributes towards the minimal conductivity of graphene at the Dirac point. The effective scattering strength can also be substantial because of weak screening effect due to small DOS and small K.E of electrons near the charge neutrality point.

In addition to electronic properties other physical properties were also studied revealing the versatile nature of graphene and its importance in various fields. The higher thermal conductivity of graphene at room temperature ranging $2x10^3$-$5x10^3$ W/mK [68,69] is another property that is beneficial for all graphene expected application in the field of electronics and photonics [70].

Elastically graphene is robust as it can be stretched up to 20% of its actual size without breaking, showing its remarkable mechanical strength. The elastic properties of graphene were reported by Lee et al [71] in 2009 demonstrating that graphene has tensile strength and fracture strength of 1 TPa and 130 Gpa respectively which are higher than other known strong materials. These exceptional mechanical characteristics of graphene can be utilized to enhance the mechanical strength, thermal and electrical properties of composites [58,72] that are widely used in different applications. Nanoelectromechanical systems (NEMS) is another area of research where high charge carrier mobility, thermal conductivity and mechanical strength of graphene make it as an ideal material to be used [73].

Graphene also exhibits remarkable optical properties. Even though it is one atom thick, it absorbs considerable amount of visible light. The optical transmittance of free standing graphene is found to be 97.7% and is independent of frequency [74]. Optical absorption of graphene is also found to be increase linearly with numbers of layers. Each graphene layer absorbs only 2.3% of the visible light. Therefore being highly transparent and conductive it can be used as transparent conductive electrodes [5,55,56,75]. The phenomena of photoluminescence over a broad spectrum range has also been reported in chemically modified graphene (bandgap induced) i.e graphene oxide [76,77]. All these optical qualities are quiet useful in optoelectronic devices such as light emitting diodes, displays, touch screens, ultrafast laser etc [70].

2.5 Graphene Applications

Graphene has surprised the world not only with this fact that it is only one atom thick material but with its unusual properties of charge carrier conductivity [1,13,15], mechanical strength [71] and optical transparency [74]. All these qualities provide graphene a bright chance to become a future material for variety of applications. A lot of efforts are dedicated to find technological applications of graphene in many diverse fields [6,16,58,70,78,79]. It is believed that in coming years graphene based products will be commercially available [80]. Figure 2.12 shows a predicted global market for graphene based products during 2009-2020.

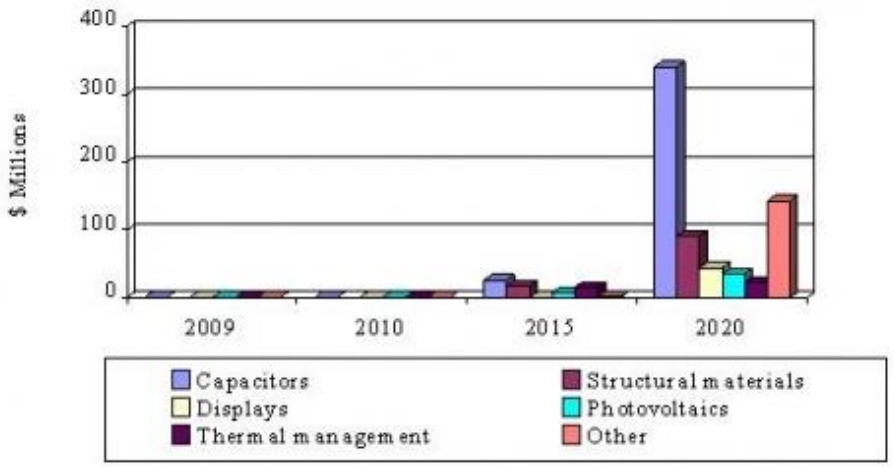

Figure 2.12: A research report on global market for graphene based products during 2009-2020.

In the field of electronics and information technology, silicon and other semiconducting materials has served the world for many years and has revolutionized the microelectronic industry by miniaturizing and enhancing the capability of electronic devices. But now these materials are approaching their ultimate limit of improving the performance and capacity, graphene appears to be a substitute to fulfil the ever rising needs of the nanoelectronics.

Charge carriers concentration in graphene can be tuned by applying electric field [1]and show ballistic transport properties at room temperature due to its high crystal quality and linear electronic band structure [14]. One of the advantages of graphene over other semiconductor materials is charge carrier mobility of graphene at room temperature which is order of magnitude higher than these materials [38,81]. These properties make it suitable for future high performance devices. Graphene based transistors is an important

research area and many graphene based field-effect transistors (GFETs) has been reported with primary focus on analogue and RF applications [16,18,82]. The high cut-off frequency and low noise of these devices makes them suitable for RF applications [83]. In very short time the RF performance of GFET has increased from 15 GHz to 300 GHz [16,18,78,84]. Wafer scale high frequency GFET has been reported using epitaxial graphene [19] and also a wafer scale graphene circuit [6] has been fabricated using all graphene based components integrated on SiC. Much higher expectations from graphene in this respect are restricted by the mobility of graphene that is destroyed by defects and impurities [20,21]. These impurities results in scattering at the graphene dielectric interface and deteriorate the performance of these devices [85]. A lot of effort has been put on the graphene dielectric interface and tried to improve the top gate quality [86,87]. Recently boron nitride has been used as a gate dielectric in graphene based devices improving their overall performance. These high frequency transistors find their applications in imaging, data communication and radar.

Absence of bandgap in graphene restricts its applications in digital electronics. Although graphene's high mobility is ideal for fast switching required in digital applications but the minimum conductivity of graphene at neutrality point due to zero bandgap produces off-current values which in turn provide low current on-off ratio. Graphene cannot be directly used for digital electronic applications due to zero bandgap. Bandgap opening in graphene can resolve this issue and can enable graphene to be used in digital electronics. Several efforts have been made to induce an effective bandgap in graphene and fabricate a graphene transistor with high on/off current ratios using graphene nanoribbons [88] and bilayer graphene [89]. Still there is long way to go before graphene can be utilized in digital electronics and provide expected applications in this field.

The scope of excellent electronic and optical properties of graphene is very high in the field of photonics and optoelectronics. Graphene's high mobility and optical transparency can be utilized in large range of applications e.g transparent conductors, photodetectors, photovoltaic devices, light emitting devices, touch panels, ultrafast lasers and terahertz devices [70]. A lot of studies has been dedicated to the use of graphene as a transparent conductive films [5,55,58,75] for various applications.

Graphene is the strongest and stiffest known material with young's modulus of 1.0 TPa and fracture strength of 130 GPa [71]. These outstanding mechanical properties along with the high aspect ratio and low density of graphene can be employed in polymer nanocomposites where graphene can be used as an ideal nanofiller for polymer matrix

[72]. Graphene based polymer nanocomposites provides better mechanical, thermal and electrical properties [58] and can be useful in composite industry. Recent progress in mass-production of graphene using solution phase method has boosted the research of these graphene polymer nanocomposites for different applications in fields like aerospace, construction and textile.

Graphene seems to have a promising future in the field of electronics due to its high charge carrier mobility, thermal conductivity and mechanical strength. Beside all these properties graphene also has power storage capability that can be used to produce capacitors and batteries with better performance and smaller size. Supercapacitors or ultracapacitors using graphene sheets can be charged and discharged in seconds [90,91] and can be utilized in electric and hybrid vehicles, regenerative brake, power regulation, memory back-up systems and portable electronic devices where fast charging is required. Charge storing capacity of these graphene based supercapacitors ranges from 75 F/g to 200 F/g using graphene based materials derived from graphite oxide (GO) [92]. To improve the overall performance of rechargeable batteries and fulfil the high energy storage and longer lifetime cycles demands, graphene surface has also been used instead of graphite as an anode in Li-ion rechargeable batteries. Recently a hybrid new design of Li-ion batteries using graphene and silicon has been reported which can increase the charge storing capacity and charging time by ten times [93,94].

Chapter 3

Graphene Device Fabrication and Measurement on Oxidised Silicon

For the purpose of graphene fundamental and applied research, device fabrication is an important step. This chapter is related to graphene device fabrication and measurements of these devices. The basic device making techniques and processes involved are discussed here along with the measurement procedures. Limitations of mobility in graphene devices on usual Si/SiO_2 substrate are also discussed.

3.1 Introduction

The rapid growth and exponential miniaturization as represented by Moore's law in the electronics industry approaching micro and then nano-scaled devices has revolutionized the technological world. Not only has the overall size of the devices reduced but also their efficiency has been raised dramatically. Various semiconductor materials are used in the electronic industry each having its own special feature (e.g high mobility, high frequency, and high thermal stability) and applications [95]. The addition of a new material, graphene with exceptional electronic properties [96], has speed up the research activities to exploit these properties of a two dimensional system in various applications. The most important electronic property of graphene is usually considered to be its room temperature mobility that is higher than other semiconductor materials used. Still however, its expected high mobility is not achieved for routine samples.

The routinely used method for graphene device fabrication, its transport measurements and limitations to achieve higher mobilities all are briefly discussed here along with results of graphene devices measured during this study.

3.2 Device Fabrication

The main device fabrication technique used for graphene devices presented in this work was optical lithography and was performed by using:

i) Kurl Suss MJB-3 mask aligner

ii) Laser Writer

Both of these procedures require extremely clean and accurate operating conditions. The step by step processes involved in each of the above mentioned techniques are outlined below.

3.2.1 Optical Lithography

Optical lithography also called Photolithography or UV lithography is a process whereby a geometric pattern is transferred from a photo-mask to a light sensitive chemical (photo resist or resist) coated on the substrate. Usually ultraviolet (UV) light is used as an exposure source in this technique. The main advantage of optical lithography is that this procedure has an exact control on shape and size of the patterns it creates, and also it can create patterns over an entire surface simultaneously. A schematic diagram and photograph of the mask aligner used is shown in Fig. 3.1. The resolution of pattern produced by the Kurl Suss MJB3 mask aligner shown here is about 0.5µm.

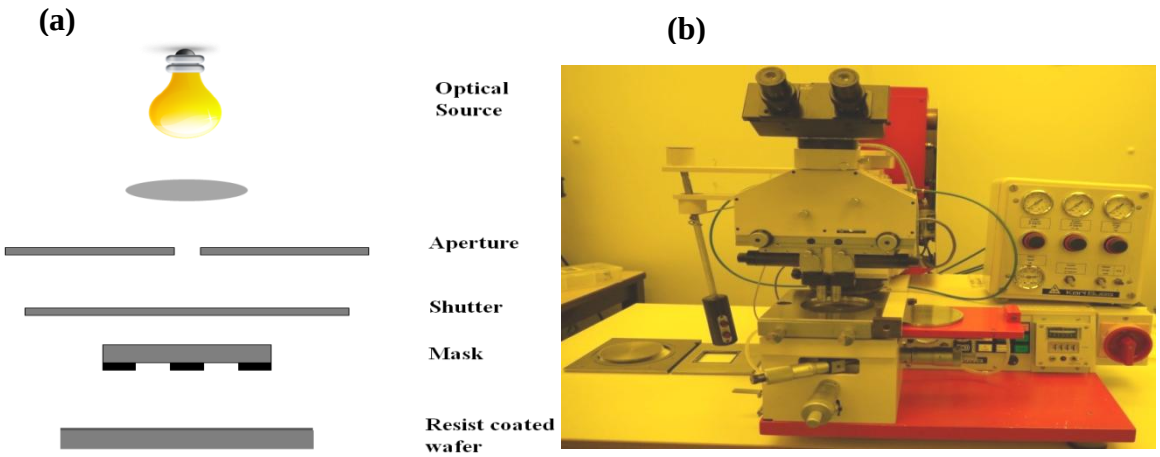

Figure 3.1:(a) Schematic diagram representing the working of a mask aligner (b) Photograph of Karl suss MJB3 UV 354 mask aligner with mercury arc lamp.

A single process of optical lithography for device making combines several sub-steps in sequence as explained below.

I. Substrate Preparation

Surface preparation is an important step prior to the application of photoresist as it improves the adhesion of photoresist and provides a contaminant free resist film in order to get maximum process control and reliability. Sample preparation includes substrate (Si/SiO_2) cleaning to remove contamination and dehydration bake to get rid of water content on the substrate surface. Substrate contamination can occur in the form of the particles on the surface that result in defects in resist pattern, or an organic or inorganic film that decreases the resist adhesion to the substrate. A standard solvent cleaning procedure is used in order to remove the contaminants from the surface of Si/SiO_2 substrate and water is removed by baking at high temperature. During the standard solvent cleaning the substrate is cleaned in acetone and then rinsed in isopropanol (IPA). The substrate is dried in high pressure flow of nitrogen. For the purpose of dehydration bake, the substrate is baked at 100-200°C to drive off the water content from the substrate and allowed to cool and immediately coated with photoresist to avoid re-absorption.

II. Spin-coating Photoresist

Spin coating is the standard method for uniform photoresist application. Spinning is a simple process in which substrate is placed on spinners having speeds of up to 10000rpm with a drop of resist on top. A film of few millimetres resist is achieved on the substrate whose thickness (t) depends on the resist viscosity (η) and spin speed (ω) according to

$$t \propto \sqrt{\frac{\eta}{\omega}}$$

The film thickness ranges from 0.1-1μm and is about 0.4μm for standard photoresists. Spin speed plays an important role in obtaining a uniform film thickness onto the substrate. The process of spin coating is explained schematically in Fig. 3.2. After spinning, the substrate is baked on a hotplate or in an oven to remove any solvent residue from resist before the exposure and is called as pre-exposure bake or soft bake.

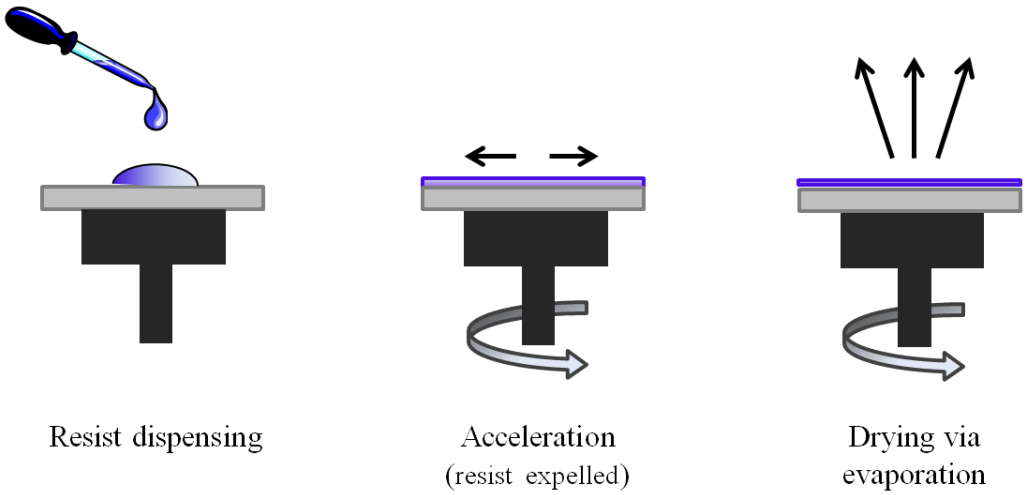

Figure 3.2: Various steps involved in photoresist spin coating during optical lithography.

There are a number of ways to perform photolithography. The method used was the bi-layer resist process. The substrate was covered with two layers of photoresist, PMGI and Shipley S-1805, by spin coating. PMGI resist is based on polydimethylglutarimide, which exhibits excellent adhesion to most semiconductors [97]. PMGI performs exceptionally well when used as an undercut layer in bi-layer resist processing.

The photograph of the spinner used for this purpose is shown in Fig. 3.3. The PMGI is spun onto the substrate at 4000 rpm for 60 seconds to produce a uniform thick layer (~200nm). The substrate is then soft-baked at 150°C for 5 minutes on a hot plate to drive off excess solvent. After the substrate cooled down, the layer of PMGI is flood exposed using a deep ultraviolet source for 18-20s. The second layer, Shipley S1805, is then spun onto the substrate at 4500 rpm for 45 seconds. The complete process of spin coating used is described in table 3.1. And finally the substrate is soft-baked again at 110°C for 60s on a hot plate.

Figure 3.3: Photograph of a spinner used in clean room.

Table 3.1: *Procedures of photoresist application by spin-coating.*

Layer	Frequency	Time
PMGI	4000 rounds per minute	60 seconds
	Soft-bake the substrate at 150℃ for 5 minutes and exposure under UV for 18-20 sec	
S1805	4500 rounds per minute	45 seconds
	Soft-bake the substrate at 110℃ for 1 minute	

III. Alignment, Exposure and Development

A photomask is aligned on the substrate using a MJB3 Mask Aligner to make sure the pattern is correctly positioned on the required region of the substrate. Afterwards, the photomask and the substrate with resist on top are brought into close contact. The area of substrate not covered by the mask is then exposed to the UV lamp for 1s. After exposure, the substrate is immediately developed in the MF-319 developer for 45-50 seconds, which removes the exposed photoresist from the substrate. The process is performed in a yellow room due to the sensitivity of the photo resists below 450nm.

IV. Metal Evaporation and Deposition

Thermal or electron beam evaporation techniques can be used for making metal contacts attached to graphene and to do electronic measurements. Thermal evaporation involves the evaporation of the source material (usually a metal) by heating it to sufficiently high temperature where it then deposits onto the substrate by condensation. Evaporation takes place in a high vacuum. Inside the evaporation chamber, vapours and particles other than the source metal are almost entirely removed before the process. The metal is heated by current through the filament which is in the form of a crucible or boat. A schematic diagram of a thermal evaporation unit is shown in Fig. 3.4(a). High vacuum conditions are required so that the evaporated particles from the source material can travel directly to the deposition target without colliding with the background gas and a contamination free deposition can therefore be obtained.

In order to evaporate Chromium and Gold, a Moorfield MiniLab system was used. The typical pressures used during evaporation were around 10^{-7} mbar. Gold cannot be directly evaporated on the typically used Si/SiO_2 substrate surface due to its poor adhesion to the SiO_2, therefore another layer of 5nm chromium, which provides good adhesion to both SiO_2 and gold surface, was evaporated prior to the evaporation of gold. Gold evaporated for alignment markers is usually 50-70nm. Figure 3.4(b) shows a photograph of a Moorfield thermal evaporator for metal deposition.

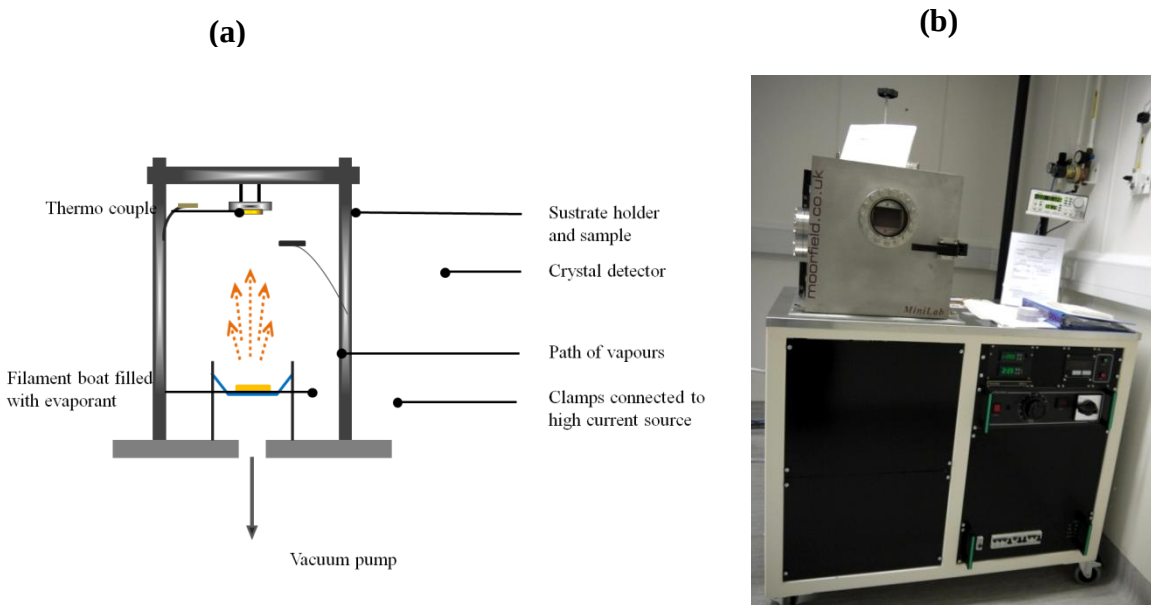

Figure 3.4: (a) Schematic view of the system used for the thermal evaporation. (b) Photograph of the Moorfield MiniLab system used for the thermal evaporation.

The other technique for the metal deposition that was frequently used for the work presented in this thesis was electron beam evaporation. As the name of this process indicates, it uses an electron beam to evaporate the source material. High deposition rates can be achieved as a result of the large amount of heat accumulated on small region of the target/source by the electron beam. This process takes place under high vacuum conditions. The e-gun filament is located outside the evaporation area to avoid the contaminants during evaporation. The heated filament, via an applied voltage, emits the electrons that are accelerated and deflected by magnets towards the target surface. The target vaporizes as a result of the energy delivered by the electron beam. A schematic of the working of an electron beam evaporator is shown in Fig. 3.5(a).

In order to evaporate Chromium and Gold by electron beam evaporation, a Moorfield E-gun evaporation system was used and a photograph of the system is shown in Fig. 3.5(b). The typical pressure used inside the evaporation chamber was around 10^{-8} mbar and a high DC voltage of 9 KV was given to the filament.

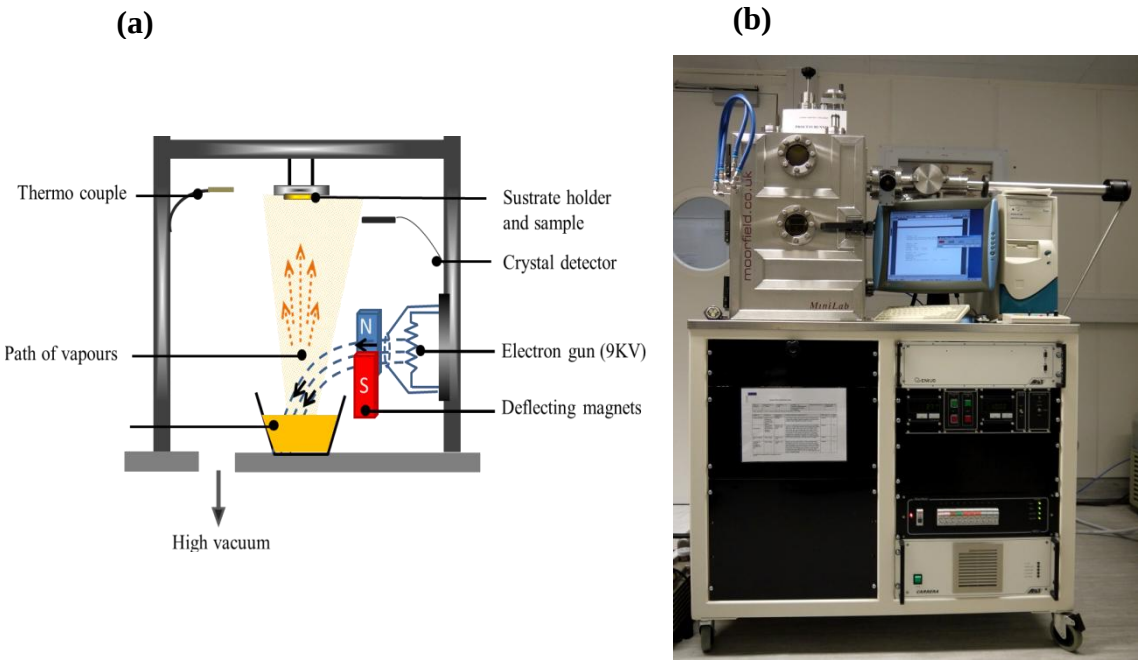

Figure 3.5: (a) Schematic view of the system used for the thermal evaporation. (b) Photograph of the Moorfield Egon system used for the electron beam evaporation.

V. Metal Lift-off

The process of lift off is the last step in the optical lithography and is required to have metal on exposed area of the substrate. After metal deposition by either of the above mentioned techniques, Cr/Au is deposited over the entire substrate, including the area masked by photoresist and areas in which the photoresist had been cleared during development process. The process of development and metal evaporation of lithography pattern for a graphene device is presented in Fig. 3.6.

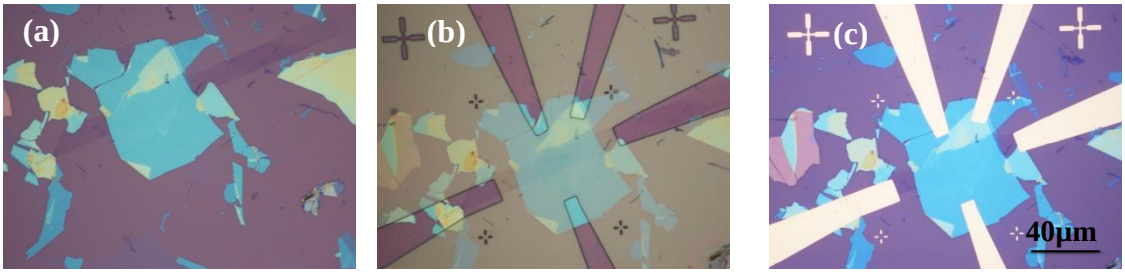

Figure 3.6: optical lithography performed on a flake (a) a selected flake before lithography (b) Post exposure resist development with MF-319 developer.(c) Au/Cr metal evaporation on in the developed area.

In order to get the metal only in the developed area of the substrate that contains the required patterns, the remaining deposited metal on photoresist has to be removed by stripping away the underlying photoresist. During the lifting-off process, the photoresist under the deposited metallic layer is removed with solvents leaving the metal only in the desired area of the substrate.

The process of lift-off used here during lithography involves the immersion of the substrate in a solvent prepared by mixing acetone and developer, MF-319. The substrate was left for several minutes until most Cr/Au on the substrate was removed. The immersed substrate was heated at 60 °C on hot plate or placed in the ultrasonic bath for a few seconds to help lift-off more stubborn areas. As a final solvent treatment step for removing the residue left on substrate, the substrate was cleaned in acetone, DI water and IPA respectively and was blow dried with nitrogen.

As an example Fig. 3.7 shows an optical image of the alignment crosses pattered on the Si/SiO_2 substrate by optical lithography with graphene on top prepared by micromechanical cleavage.

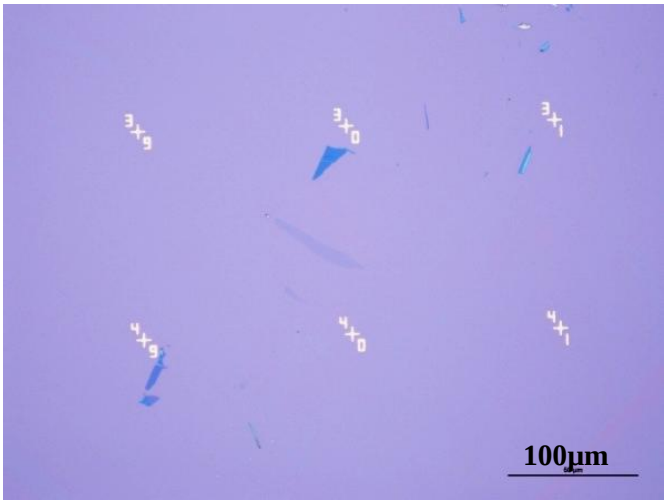

Figure 3.7: White light optical image of the micromechanically cleaved graphene on Si/SiO_2 substrate with alignment crosses patterned by mask aligner Karl Suss MJB3.

Step by step schematic diagram of the optical lithography process is shown in Fig. 3.8.

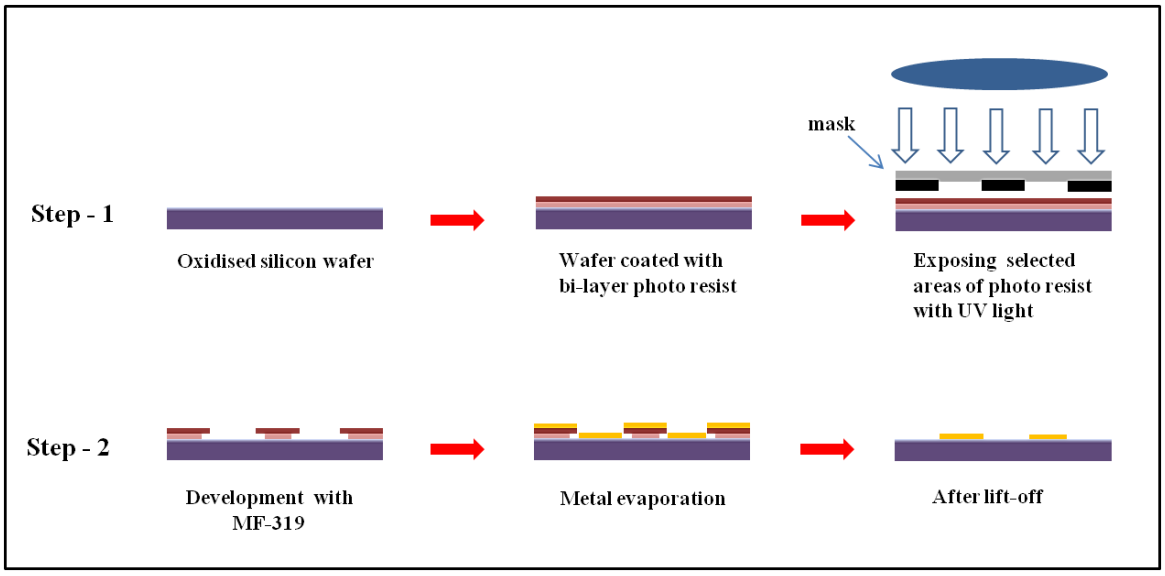

Figure 3.8: Step-by-step procedure of the optical lithography using photoresists and mask aligner.

3.2.2 Lithography Using Laser Writer

Initially, optical lithography had always been dependent on the use of photomasks in order to transfer patterns/structures to the substrates however, the art of patterning using optical lithography without the use of a photomask was started in 1987 by the introduction of first laser direct write system [98]. This direct writing laser lithography system provides fast patterning of submicron structures using standard photoresists. It uses a focused laser beam to directly expose the photoresist without a photomask and is based on the scanning technique of "writing pixel after pixel". Figure 3.9(a) represents a simple schematic diagram of the laser writer scanning and Fig. 3.9(b) shows the photograph of a Microtech Laserwriter LW405 system used for lithography during graphene device preparation presented in this thesis.

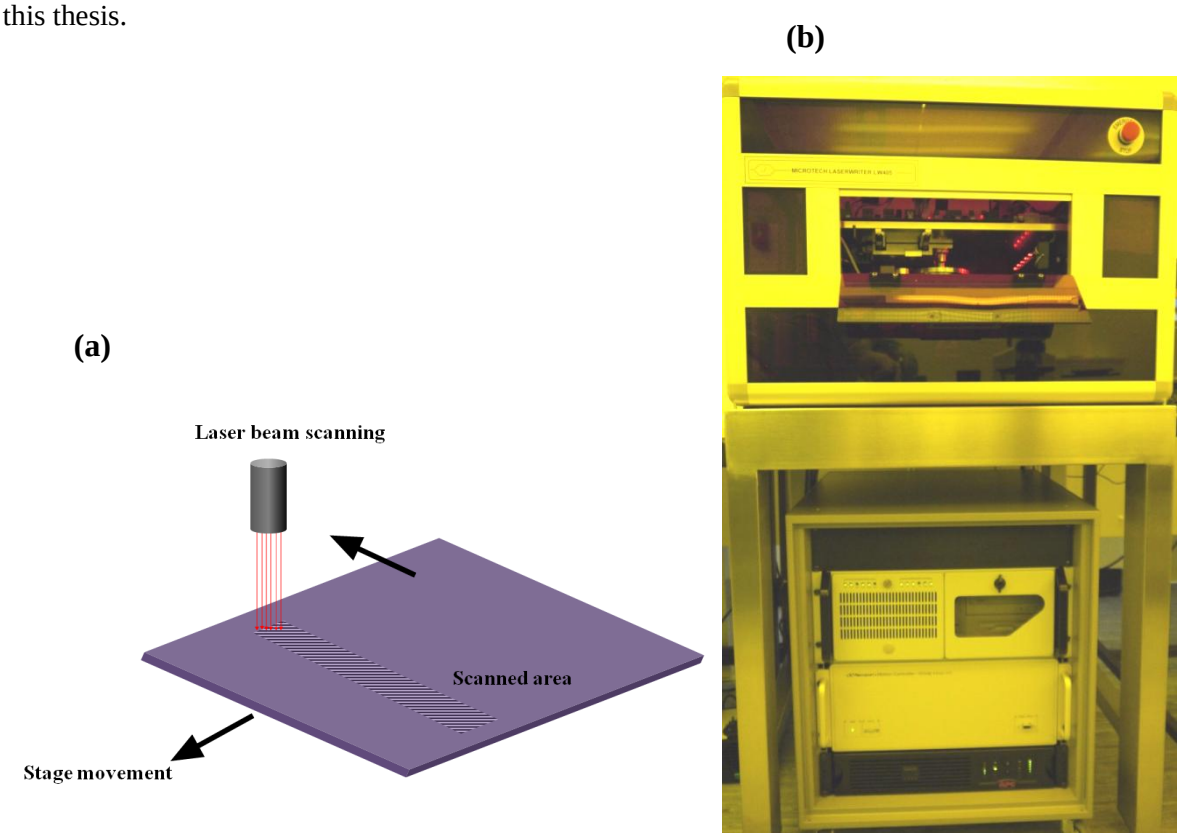

Figure 3.9: (a) Schematic drawing of the Laser writer scanning on the substrate. (b) Photograph of Microtech Laserwriter LW405 system used for lithography.

A 405nm GaN solid state laser is used for scanning exposures and produces microstructures with resolution of 0.5micron. Figure 3.10 shows the photograph of the stage used for holding the substrate and laser interferometer for positioning.

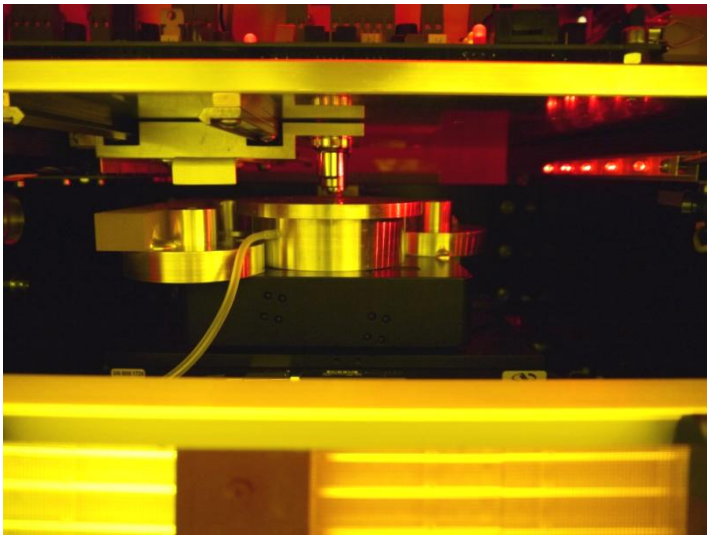

Figure 3.10: Photograph of the stage for holding the substrate to be scanned by LW405 system using 405 nm GaN solid state laser.

Lithography using laser writer involves the same step by step procedure as used for optical lithography explained above except for the fact that Laser writing directly exposes the photoresists instead of a photomask.

The procedure adopted for laser writer lithography is again bi-layer resist process. The photoresists used are the same as used for standard photomask optical lithography i.e PMGI and S1805. The specifications and procedure used for spin coating both photoresists are described in table 3.2.

Table 3.2: *Procedures of photoresist application by spin-coating.*

Layer	Frequency	Time
PMGI	4000 rounds per minute	60 seconds
	Soft-bake the substrate at 170℃ for 5 minutes and exposure under UV for 18-20 sec	
S1805	4000 rounds per minute	60 seconds
	Soft-bake the substrate at 110℃ for 1 minute	

An optical image of a graphene devices fabricated by using laser writer is shown in Fig. 3.11. Device patterning using laser writer has an advantage over conventional photo-lithography using mask aligner because it permits us to design according to arbitrary shape of flakes where as we can only expose fixed patterns in photo masks.

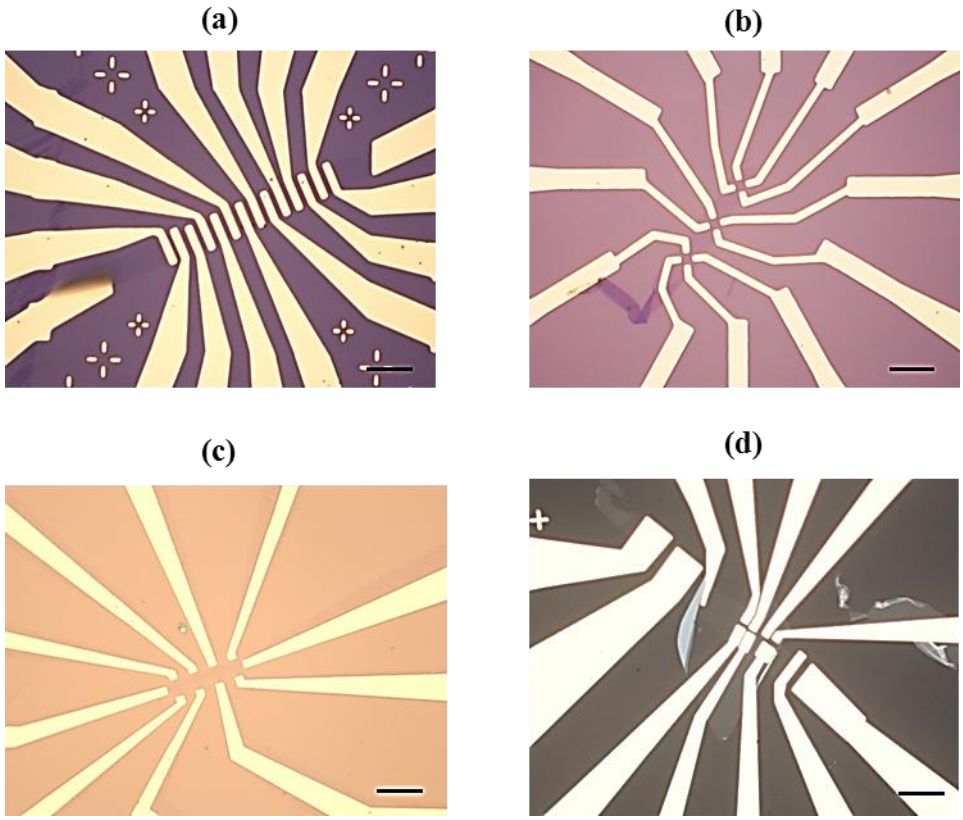

Figure 3.11: Optical images of graphene device fabricated by laser writer on Si/SiO_2 and quartz. Scale bar representing length 10µm.

3.3 Measurement of Graphene Devices

For fundamental studies of the material and its applications in electronics, it is very important to measure the response of a fabricated device to an applied voltage. One of the most widely used approaches is to make use of the electric field effect to build a transistor called as field effect transistor (FET). The applied electric field can alter the charge carrier concentration and resistance in the material thereby controlling/tuning the electronic properties of the material. Conventionally in semiconductor electronics, a metal-oxide-semiconductor (MOS) structure named as MOSFET is used to control/tune the charge carriers of the semiconductor through an electric field produced as a result of an applied voltage to the metallic gate [99,100]. A typical graphene device as presented schematically in Fig. 3.12 also produces the same effect. The structure has a graphene layer on an oxidized silicon (SiO_2) surface with metal contacts on top. The electric field effect can be observed in this graphene structure by applying gate voltage V_g to the silicon that serves as a backgate.

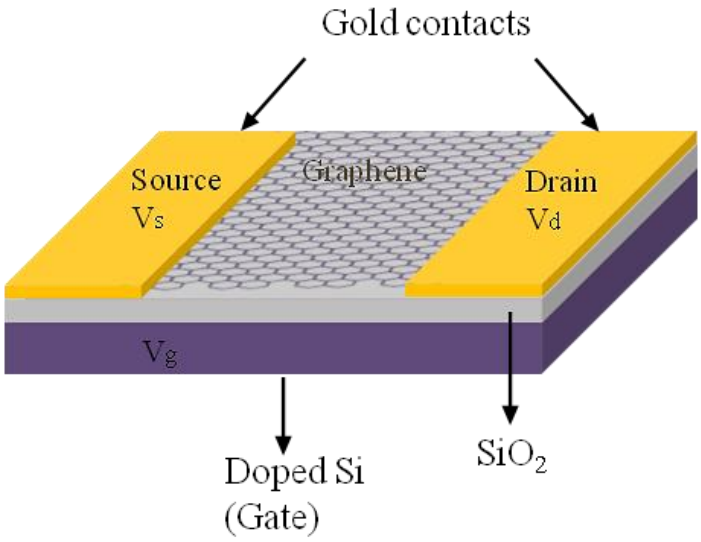

Figure 3.12: Schematic picture of the a typical graphene device on Si/SiO_2.The doped Si used as a semiconducting backgate to tune the graphene charge carriers by applied voltage V_g.

The graphene device structure shown schematically in Fig. 3.12 serve as a capacitor with one plate of doped Si (gate) separated by an oxide layer SiO_2 of few hundreds of nanometers from graphene layer acting as the second plate of capacitor.

The voltage V_g applied across the silicon backgate accumulates the charge carriers (electrons or holes) between Si and SiO_2 junction which in turn induces the charge carriers (holes or electrons) in the graphene sheet. The capacitance C of such a capacitor can be taken as:

$$C = \frac{Q}{V_g} \tag{3.1}$$

where the charge induced Q is the capacitor charge for the area A of the junction and given by:

$$Q = enA \tag{3.2}$$

The resultant electric field effect induced charge carrier density n,

$$n = \frac{\varepsilon_r \varepsilon_0}{ed} V_g \tag{3.3}$$

$$n = \alpha V_g \text{ with } \alpha = \frac{\varepsilon_r \varepsilon_0}{ed} \tag{3.4}$$

Where ε_o is the dielectric constant of free space, $\varepsilon = \varepsilon_r \varepsilon_0$ is dielectric constant of SiO_2, *e* is the electron charge and *d* is the thickness of SiO_2 layer, For d= 300 nm and ε=3.7, the value of $\alpha \approx 7.2\times10^{10}$ cm^{-2}/V. Equation (3.4) shows that the charge carrier density *n* induced in graphene by the electric field varies linearly with the gate voltage V_g.

The capacitance C in eq. (3.1) then becomes

$$C = \frac{\varepsilon \varepsilon_0 A}{d} \tag{3.5}$$

In a graphene device, the change in carrier density with the applied voltage can also be used to tune the Fermi level [14]. For undoped graphene, in the absence of the applied voltage V_g, the Fermi level E_F lies exactly at the point where the conduction and the valence bands join each other (it is the single point in the band structure of graphene called as Dirac point). The applied voltage V_g changes the position of the Fermi level E_F as shown in Fig. 3.13. The positive (negative) voltage induces electrons (holes) for field effect graphene device and shifts the Fermi level to the conduction (valence) band. The charge carriers (electrons and holes) induced by the applied voltage decreases the resistance and contribute to the transport of the graphene device. Therefore the applied voltage controls the charge induced on a graphene device by changing the charge carrier type and concentration below or above the Fermi level.

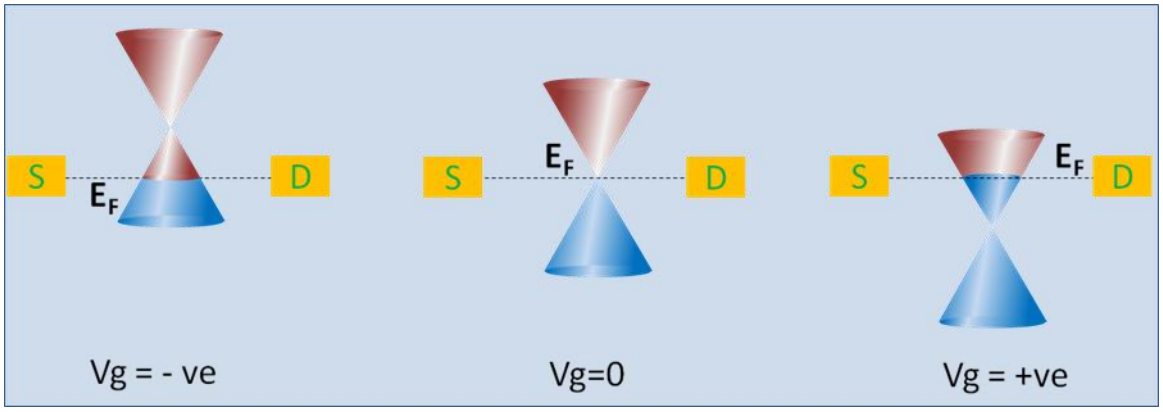

Figure 3.13: Change in position of Fermi level E_F with gate voltage V_g. Undoped graphene have E_F at the points where conduction and valence band meet each other. The positive V_g shifts the E_F to the conduction band by inducing electrons and negative V_g changes the E_F to the valence band by inducing holes as charge carrier density $n=\alpha V_g$,for graphene devices on 300 nm SiO_2 layer $\alpha=7.2\times10^{10}$ cm^{-2}/V

3.4 Transport in Graphene

The electronic devices work on the basis of the transport of the charge carriers in the material. Charge carriers in materials are transported by appropriate forces like electric or magnetic fields. In graphene, charge carriers travel several hundreds of nanometers before scattering due to its high crystal quality (less defects and impurities) [14]. Therefore the charge carrier mobility which is determined by the carrier drift velocity in the presence of the applied electric field is expected to be much higher for graphene than other semiconductors. Mobility of charge carriers is an important electronic property of a material and a crucial parameter for many technological applications. For a graphene device exhibiting an ambipolar field effect, the first transport measurements demonstrated the charge carrier concentrations up to $10^{13}cm^{-2}$ and room temperature mobilities of 10,000 cm^2/Vs [1]. Since then a lot of efforts has been made to enhance the carrier concentration and mobility of graphene in order to explore fully this new material [20,101,102] .

For a graphene field effect device, the mobility μ of charge carriers can be determined by the Drude model in which charge particles are treated classically:

$$\mu = \frac{\sigma}{ne} \tag{3.6}$$

where σ is the charge carrier conductivity, n and e are the charge carrier density and charge of the electron respectively. Using the relation (3.6), the mobility of the both electrons and holes can be determined. The electric field effect in graphene results in the resistivity ρ and conductivity (σ=1/ρ) curves shown in Fig. 3.13. The resistance of graphene changes with the gate voltage and is maximum at the Dirac point whereas the conductivity is minimum at this point. The conductivity changes linearly with the gate voltage as shown in Fig. 3.14.

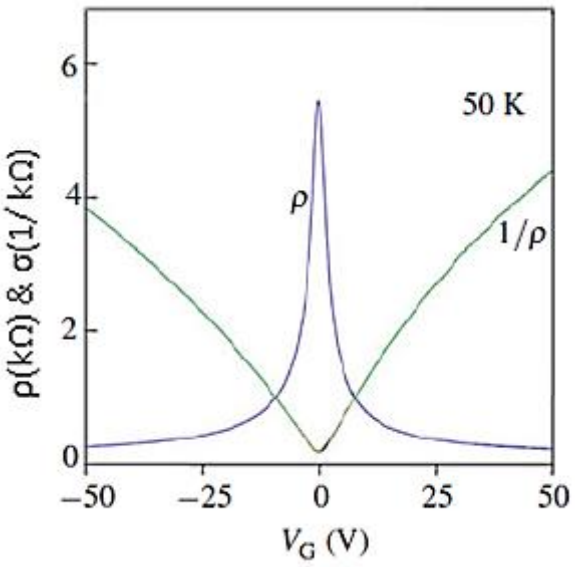

Figure 3.14: Resistivity ρ and conductivity σ as a function of gate voltage V_g. The conductivity σ changes linearly for both positive and negative V_g [21].

When the magnetic field is applied to the graphene device, the Hall coefficient $R_H = \frac{1}{ne}$ shows a linear dependence on the gate voltage $R_H \propto \frac{1}{V_g}$. Thus the ratio of the charge carrier density, n and the gate voltage V_g yields 7.3×10^{10} cm^{-2}/V for graphene device on 300nm which is in agreement with the above theoretical calculated value of α. In terms of Hall coefficient, the mobility of a graphene can be determined by:

$$\mu = R_H\sigma = \frac{R_H}{\rho} \tag{3.7}$$

Where σ and ρ are the charge carrier conductivity and resistivity.

The mobility of graphene on Si/SiO_2 substrate at room temperature ranges from 5,000-15,000 cm^2/Vs [14] and reaches up to 200,000 cm^2/Vs for suspended graphene [15].

The transport measurement of a graphene device on Si/SiO_2 is shown in Fig. 3.15. The resistivity ρ (kΩ) and conductivity σ (mS) varies with the carrier density n (cm^{-12}) as presented in the measurements below.

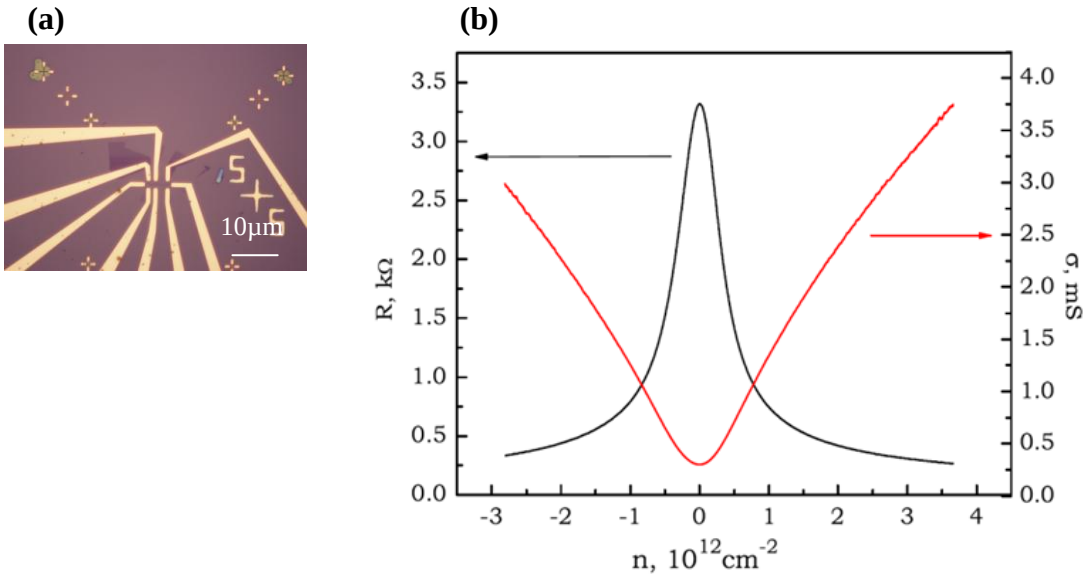

Figure 3.15: (a) A hall- bar graphene device on 300 nm Si/SiO_2 (b) Resistivity and conductivity as a function of the carrier density for a graphene device on Si/SiO_2.

The mobility of graphene on Si/SiO_2 derived from the above measurements gives:

$$\mu = 5{,}000\ cm^2V^{-1}S^{-1}$$

.

Experimental data of graphene mobility taken from other three devices fabricated on Si/SiO_2 substrates with standard four probe geometry is presented in Fig. 3.16. Despite of using different substrate cleaning procedures, the measured values of graphene mobility still ranges ~ 5000-15000 $cm^2V^{-1}S^{-1}$.

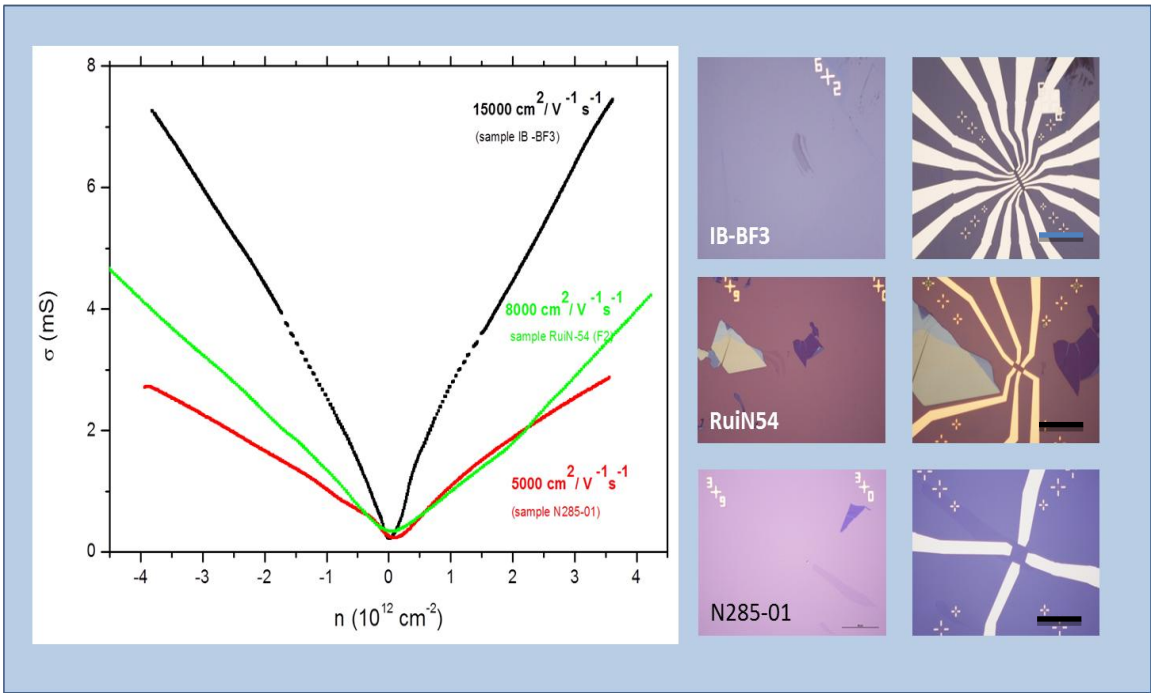

Figure 3.16: Experimental data of graphene mobility measured on oxidised silicon surface(left) and the optical images of the devices used for these measurements(right). Scale bars are same and represent 15µm.

The value of mobilities for other semiconductors is also given in table 3.3.

Table 3.3: Mobilities of electrons μ_e and holes μ_h at the room temperature for various semiconductors [95].

Material	$-\mu_n$(cm²/Vs)	μ_p(cm²/Vs)
Si	1300	500
Ge	4500	3500
GaAs	8800	400
GaN	300	180
InSb	77,000	750
InAs	33,000	460
InP	4600	150
ZnO	230	8

As seen above, the room temperature mobility of graphene is higher than other semiconductors. However, the mobility of graphene on a Si/SiO_2 substrate is lower than that of suspended graphene.

3.5 Factors limiting graphene mobility

The decrease in graphene's mobility on the substrate is related to the scattering of charge carriers that limits the intrinsic high mobility of graphene [21,103,104]. It is very important to investigate the factors limiting graphene's mobility as high mobility graphene devices (less impurities and defects) are required in graphene based electronics and are also important to investigate the physics of graphene charge carriers.

The charge carriers in electronic structures experience scattering during their motion under the influence of driving force. The scattering rate (average time between scattering events) can be taken in terms of the relaxation time τ of the charge carrier. The mobility of charge carriers is related to the relaxation time by the expression:

$$\mu = \frac{e\tau}{m^*} \tag{3.8}$$

Where m^* is the effective mass of the charge carrier.

The conductivity and mobility of charge carriers are linearly linked therefore:

$$\sigma = \mu ne = \frac{ne^2\tau}{m^*} \tag{3.9}$$

The corresponding resistivity can be written as:

$$\rho = \frac{m^*}{ne^2\tau} \tag{3.10}$$

Generally the charge carriers in an electronic structure undergo different kinds of scattering processes and the relaxation time of charge carrier sums up all the scattering processes [95]. If the relaxation times, τ_i, of various scattering processes are independent then the total relaxation time τ can be taken as:

$$\frac{1}{\tau} = \sum_i \frac{1}{\tau_i} \tag{3.11}$$

Therefore the total scattering probability is taken as the sum of all possible scattering probabilities occurring in the electronic structure.

The charge carriers scattering in graphene is mainly contributed by the charged impurities [103,104], neutral impurities (as a result of defects or dislocation in the crystal structure) [103], intrinsic phonons [105], ripples (strain) [106], resonant scatterers [102], surface phonons [20] and surface roughness [107].

The scattering of charge carriers by charged impurities is taken as a long range scattering mechanism as a result of the long range coulomb potential produced by these charge impurities. The origin of these charge impurities is the undesired trapped charges on the graphene substrate (usually SiO_2) or on the interface between graphene and the substrate. The concentration of charge impurities of a typical graphene sample is estimated ~ 10^{12} cm^2. The experimentally reported linear conductivity of graphene with the charge carrier density is also verified by this source of scattering. It was reported that the scattering rate by long range scatterers (coulomb scatterers) $< \tau_l > \sim n^{1/2}$ [103,104] plays a significant role in limiting the carrier mobility at the lower charge carrier concentration. The decrease in the carrier mobility of graphene as a result of potassium doping was demonstrated [104] and also the ultra high charge carrier mobilities were observed in suspended graphene [15] with less charge carrier scattering.

The neutral impurities arising from the defects and dislocations give rise to the short range potential and are known as short range scatterers. The short range scattering by neutral impurities has a small impact on the graphene's resistivity, and hence on its conductivity and mobility [103,104]. The scattering rate in the case of short range scatterers $< \tau_s > \sim \frac{1}{n^{1/2}}$ shows that these scatterers are not significantly active and contributing at the low charge carrier concentration.

In the presence of both long and short range scattering the total contribution of scattering is given by eq. (3.11) and therefore becomes

$$\frac{1}{\tau} = \frac{1}{\tau_l} + \frac{1}{\tau_s} \tag{3.12}$$

The mobility of graphene at high charge carrier densities is affected by the scattering due to the intrinsic phonons. This intrinsic scattering limits graphene's mobility as the extrinsic scatterers i.e charge impurities can be minimized by using high K dielectrics that can screen the charge impurities. S.V. Morozov et al. [21]demonstrated that this intrinsic phonon scattering is weak in graphene and mobilities ~ 200,000 cm^2/Vs are achievable if the extrinsic limits are controlled.

Ripples, large scale and nano-scale, in graphene layers could also be the factor hindering high graphene mobilities [106]. The ripples in graphene are unavoidable and are part of the two dimensional graphene sheet that help to stabilize the crystal. However observed topography shows that strain as a result of these ripples is not consistent with the strain distribution required to give the conductivity linear dependence on carrier density [107].

Resonant scatterers (RS) are also one of the factors limiting the graphene's charge carrier mobility [102]. These are the atomic scale defects originating from the adsorbates on graphene and result in long range scattering of charge carriers. RS lead to the intervalley scattering observed in the form of Raman D-peak in graphene samples.

Usually oxidized silicon is used as a substrate to deposit graphene and it was reported that the SiO_2 surface phonons play a vital role in the scattering of charge carriers [20]. Also surface roughness plays a significant role in the charge carrier mobility of graphene [107]. The roughness of SiO_2 may give rise to the long range strain that is detrimental for high mobility graphene samples. Ultra high mobilities observed in suspended graphene [15] confirms the role of substrate induced factors in limiting the mobility of graphene. Therefore the intrinsic high mobility of graphene ~200,000 cm^2/Vs can be achieved [21,22] if the extrinsic scattering sources are eliminated by an alternate substrate for graphene or suspending graphene. A smooth and inert substrate with high dielectric strength is always in high demand as an underlying substrate for graphene.

In order to improve the mobility of graphene devices up to reported intrinsic mobility, a number of possible methods have been used such as clean fabrication of graphene devices, annealing and alternate substrates for graphene. The other substrates (amorphous carbon, mica [108] …) used for graphene so far have given rise to the same kinds of problems and

have not been able to routinely increase the obtained 10,000 cm^2/Vs mobility of graphene. Recently hexagonal boron nitride crystals has been used as a substrate for graphene and it has shown to produce high quality graphene devices with mobilities of 140,000 cm^2/Vs near neutrality point at carrier density ~ $10^{11}cm^{-2}$ [24]. Hexagonal boron nitride is a better choice for graphene based electronics due to its flat surface [109], large electrical bandgap [110], dielectric strength and structural similarity with graphite (chemical inert, no dangling bonds).

3.5 Conclusions

In this study, mobility of all measured graphene devices on Si/SiO_2 ranges between 5000-15000 $cm^2V^{-1}s^{-1}$. The average mobility of routinely made graphene devices on oxidized silicon has not been improved to desired extent by clean fabrication and even annealing the devices. Hence to increase the mobility of graphene for the study of new physics in this two dimensional system and many technological applications, a novel substrate for graphene is suggested.

Chapter 4

An Atomically Flat Substrate: Hexagonal Boron Nitride

4.1 Introduction

Graphene, a monolayer of graphite, was first isolated successfully in 2004 [1]. It has opened a new area of research i.e. physics of two dimensional material and has attracted much scientific attention [1]. The existence of this class of material has been considered unachievable due to its thermodynamically unstable behaviour at atomic scale [111,112].

Soon after the discovery of this missing class of materials, thin layers of other 2D layered materials e.g. transition metal dichalcogenides ($NbSe_2$ and, MoS_2), and layered super conductors (BSCCO) were also extracted by micromechanical cleavage on arbitrary substrates [11]. Boron nitride is one of the candidates in this material family considered as sister material of graphene due to its structural similarities. It is also known as white graphite. It has two allotropes hexagonal Boron Nitride (hBN) and cubic boron nitride (cBN) similar to graphite (hexagonal) and diamond (cubic) [113]. Fig. 4.1 is schematic of Hexagonal boron nitride crystal structure.

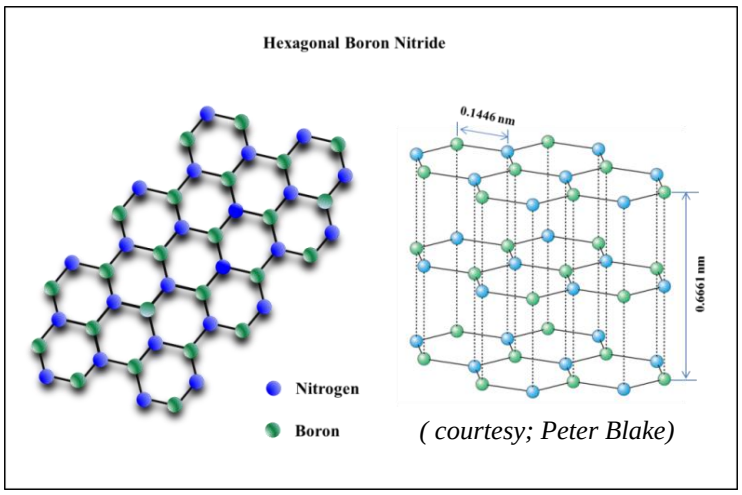

Figure 4.1: Schematic of Hexagonal boron nitride crystal structure. Monolayer of boron nitride with alternating boron (green) and nitrogen (blue) atoms (left). Layered structure of bulk boron nitride (right).

Hexagonal Boron nitride has honey comb lattice structure with alternating boron and nitrogen atoms at lattice sites such that in an atomic plane each boron atom is attached to three nitrogen atoms by means of covalent bonding and vice versa. B and N atoms are stacked so that each B3N3 hexagons is placed above and below N3B3 hexagon .

Fig. 4.2. is a schematic of hBN and Graphite crystal structures. Despite of having similar honey comb lattice, the hBN stacking is AA′, different from graphite's AB Bernal stacking which has the same planar arrangement but offset planes so that only half the carbon Atoms have neighbours directly above and directly below [114].

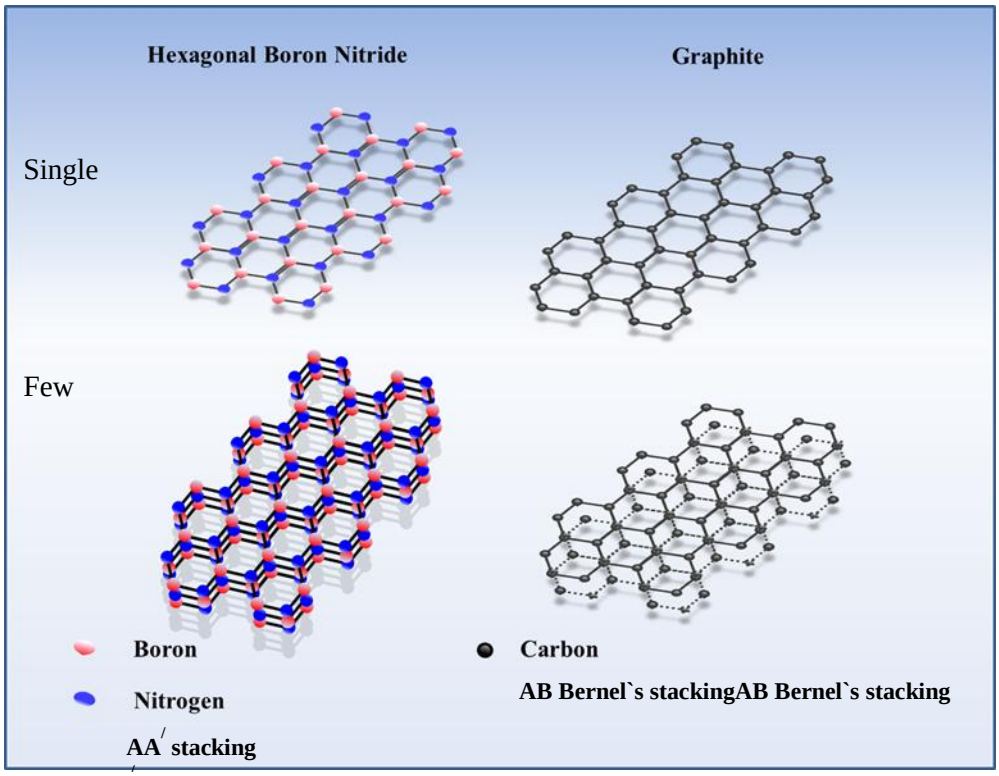

Figure 4.2: Comparison of the crystal structures of boron nitride (left) and graphite (right).

The lattice constants for boron nitride are very close to graphite lattice constants (hBN lattice constant is only 1.7% larger than graphene). Hexagonal planes are weakly bonded by the van der Waals forces same as the graphite planes. The strong in-plane covalent bonding of boron and nitrogen atoms and weak bonding between the planes gives anisotropy in boron nitride. The bond length in hBN is nearly same as that of in graphitic planes with an angle of 120^0 between the atoms.

The electronic properties of hBN are, however, different from graphite. No free electrons are present in the hBN for conduction. P_z orbitals in boron atoms are vacant whereas in nitrogen atoms, they are occupied by the neighbouring electrons. Thus, there are no electrons left to overlap and to form π bonds. Therefore, boron nitride has insulating character [115]. For graphite, the fourth valence electron is paired with an electron of the adjacent plane and form π bonds, responsible for the high conductivity.

Boron nitride is not found in nature and is therefore produced synthetically from boric acid or boron trioxide. The initial product is amorphous BN powder, which is converted to crystalline h-BN by heating in nitrogen flow at temperatures above 1500 [116].

c-BN is made by annealing h-BN powder at higher temperatures, under pressures above 5 GPa. Contrary to diamond, larger c-BN pellets can be produced by fusing (sintering) relatively cheap c-BN powders. As a result, c-BN is widely used in mechanical applications [117].

Lack of interest in single and few layers of boron nitride were due to unavailability of high grade boron nitride. But in recent few years, synthetically produced good quality of hexagonal boron nitride provoke the interest of researchers in this material [116]. It can be cleaved with ease and large size thin flakes (>100um) of this material are now possible. The HRTEM and STEM studies show that there are no pinholes in this material and therefore, making it an ideal material for the use as thin insulator [118].

4.2 Experimental Methodology

The optical image of a bulk hexagonal boron nitride crystal is shown in Fig. 4.3. Bulk BN crystal size varies from 0.5mm 1.5mm both in length and width.

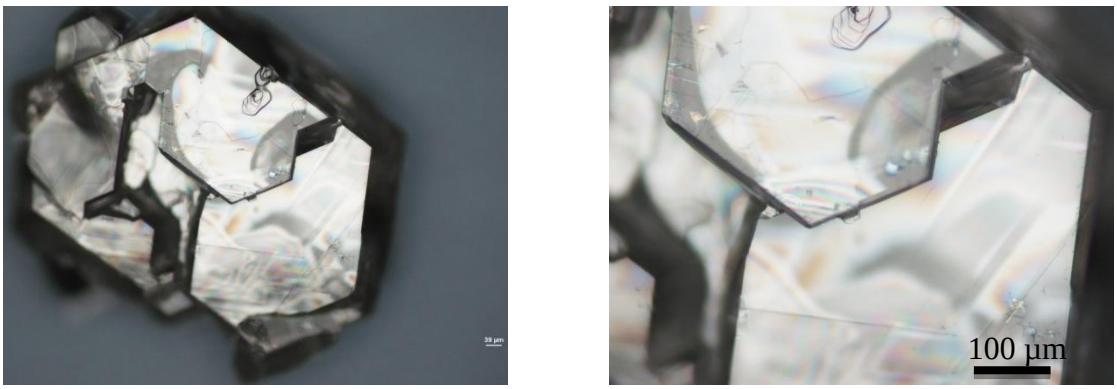

Figure 4.3: Optical image of a bulk hexagonal boron nitride (hBN) crystal

Unlike graphite, the thin crystals of hBN are transparent. Oxidised silicon wafer was used as substrate for making hBN flakes. The flakes were made by standard cleavage method just like graphene preparation explained in section 2.22. Schematic of flake preparation is shown in the Fig. 4.4.

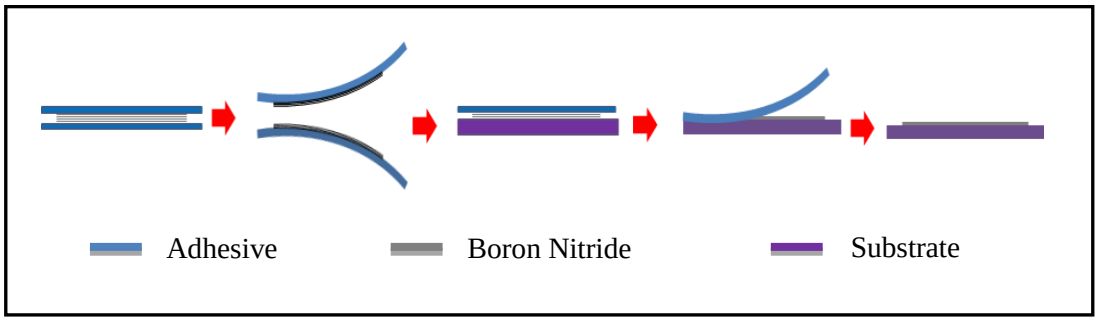

Figure 4.4: Schematic of micromechanical exfoliation of boron nitride crystal.

Monolayer and few layers flakes were initially identified by optical microscopy. The thickness of layers in various flakes was also verified by atomic force microscopy (AFM) and Raman spectroscopy.

Optical microscopy is a well-known technique for flake hunting. In this technique, the numbers of layers in any flake are estimated by observing their optical contrast on the underlying substrate. It provides a quick way for identifying mono and few layer thick flakes [9]. When compared to graphene, monolayer of boron nitride shows low contrast due to zero opacity [9]. This contrast may be improved by using additional optical filters in optical microscope and also by varying the oxide thickness of underlying substrate. The single layer boron nitride flakes on silicon substrate with 300 nm oxide thickness shows <1.5% white light contrast and usually makes it difficult to work with. Optimal contrast may be obtained by using optical filter of wavelength 590nm. When the hBN flakes were prepared on 90nm thick oxidised silicon substrate, maximum contrast was observed with 560nm optical filter. Highest white light contrast was observed for oxide thickness 80±10 nm. It was found that the contrast reaches ~2.5% per layer, similar for graphene on 90 nm SiO2. Fig. 4.5 showing the contrast enhancement of hBN flakes both by changing the oxide thickness and using additional optical filters.

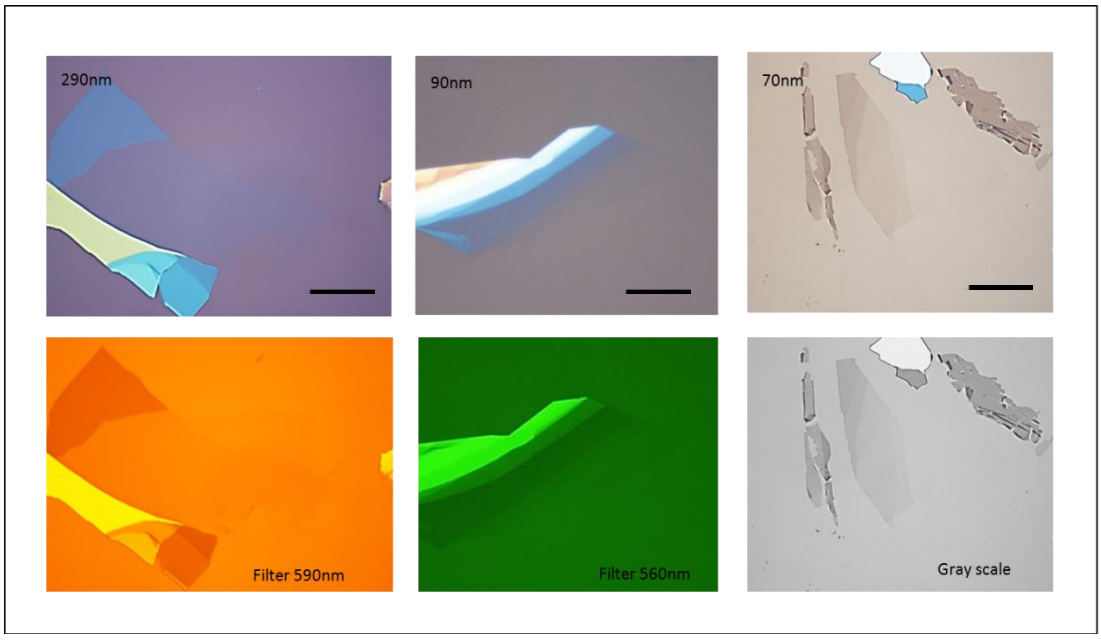

Figure 4.5: Optical image (White light) of hBN flakes silicon substrate with different oxide thicknesses (up). Contrast enhancement of hBN flakes by using optical filters (down). Scale bar is same and represents 20µm.

Numbers of layers in a BN flake can be confirmed by measuring their thickness. Since 0.35 nm is the lattice constant for hBN in C direction therefore, atomic force microscopy (AFM) may be useful for this purpose.

A bilayer flake of boron nittride was prepared on 300nm oxidised silicon sabstrate using michromechanical exfoliation technique. Fig. 4.6(a) is the optical images (white light) and Fig. 4.6(b) is tapping mode AFM micrograph of the same flake and is bilayer flake from scale height.

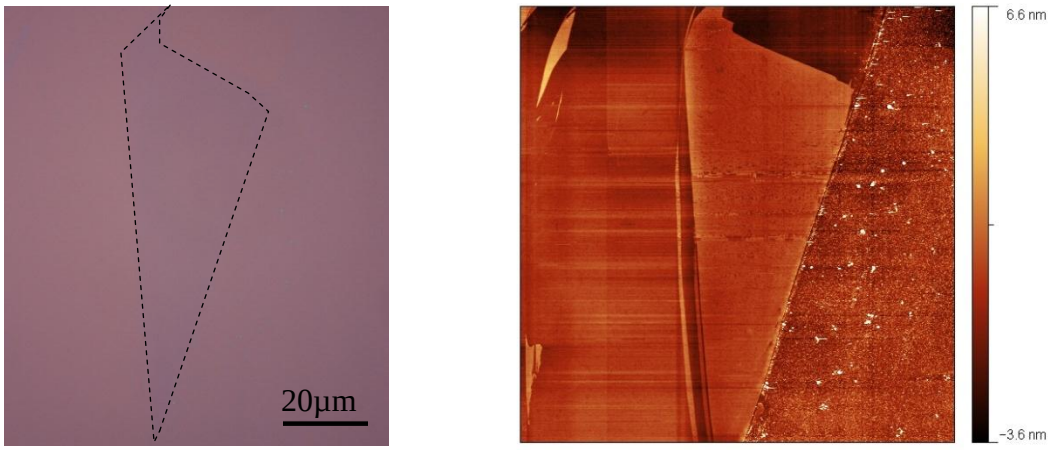

Figure 4.6: optical image of a bilayer hBN flake (left), AFM micrograph of the hBN flake (right).

Scanning electron microscopy (SEM) is another experimental technique for topological studies. Unlike graphite layers, the contrast of thin BN layers observed relatively darker to that of thick layers. Fig. 4.7 is a SEM micrograph of another BN flake. Clearly the contrast of monolayer of BN is higher than thick layers.

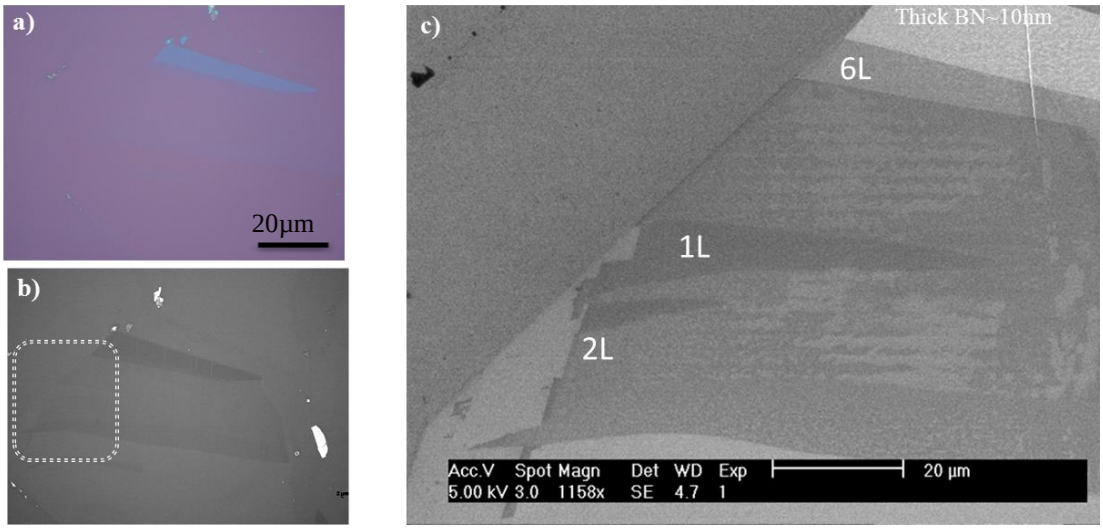

Figure 4.7: (a) white light Optical image of hBN flake (b) optical image with contrast enhanced by a factor of 2 (c) SEM micrograph of selected region of flake. Monolayer contrast is higher than thick layers.

Raman spectroscopy is useful tool often used to identify single and few layer graphene flakes [27]. Similarly it has proved itself an equally good technique for identification of monolayer to few layer thick hBN flakes. Raman peak of thick hBN is centred at 1366 cm^{-1}. The position and intensity of the Raman peak is sensitive to number of layers. Fig. 4.8 is a Raman spectrum of single to few layer thin hBN flake. Clearly the position and intensity varies with number of layers. Peak intensity is found to be proportional to layers thickness.

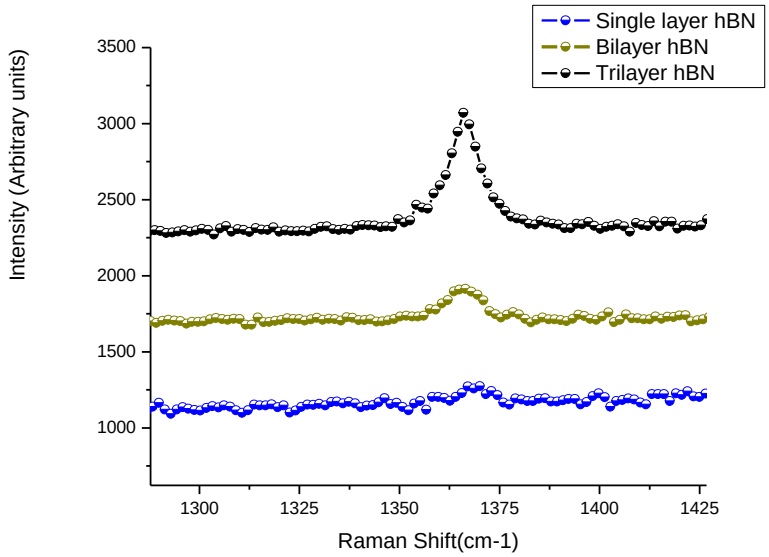

Figure 4.8: Raman spectra of single, bi-layer and tri layer of BN. The intensity of the peak changes with the number of BN layers.

4.3 Results and Discussion

The results of this work have been published in ***Small*** *in* 2011. In order to best present our results, the original paper "Hunting for Monolayer Boron Nitride: Optical and Raman Signatures" (Small, 7(4), 2011, P 465-468) is attached from the next page.

This work presented was carried out in collaboration with several colleagues of the University of Manchester. My contribution to this work includes the preparation of boron nitride flakes on oxidised silicon substrates by mechanical cleavage and verification of monolayer graphene Si/SiO_2 substrate by optical contrast.

Hunting for Monolayer Boron Nitride: Optical and Raman Signatures

Roman V. Gorbachev, Ibtsam Riaz, Rahul R. Nair, **Rashid Jalil**, Liam Britnell, Branson D. Belle, Ernie W. Hill, Kostya S. Novoselov, Kenji Watanabe, Takashi Taniguchi, Andre. K. Geim, and Peter Blake

Small, 7(4), 2011, P 465-468

Properties of few-nanometer-thick BN sheets (often referred to as few-layer BN) have been attracting steady interest over the last several years. [1] Although individual atomic planes of BN were also isolated [2] and investigated by transmission electron microscopy (TEM) [3-5] and atomic force microscopy (AFM) [6], interest in BN monolayers has been rather limited, especially, if compared with the interest generated by its "sister" material, graphene [7]. This can be attributed to 1) the lack of hexagonal boron nitride (hBN) crystals suitable for the mechanical cleavage approach [7] and 2) difficulties in isolating and finding sufficiently large BN monolayers. The situation is now changing rapidly due to the availability of hBN single crystals, which allow the cleavage of relatively large (~ 100 μm) and relatively thin (several nm) BN samples with an atomically flat surface.[6,8,9] Such crystals have been used as a thin top dielectric to gate graphene[9] and as an inert substrate for graphene devices, which allowed a significant improvement of their electronic quality,[8] unlike the earlier attempts with highly-oriented pyrolytic boron nitride (HOPBN).[10] Most recently, it has been demonstrated that BN films with 2 to 5 layer thickness can also be obtained by epitaxial growth on copper and subsequent transfer onto a chosen substrate.[11] Particularly motivating is the emerging possibility to use BN as an ultra-thin insulator separating graphene layers. The layers could then be isolated electrically but would remain coupled electronically via Coulomb interaction, similar to the case of narrow-spaced quantum well heterostructures.[12] Such atomically thin BN-graphene heterostructures may allow a variety of new interaction phenomena including, for example, exciton condensation.[13]

In the case of graphene, its mono-, bi- and few- layers are often identified by their optical contrast[14] and Raman signatures.[15] Little is known about these characteristics for the case of BN and, in the previous AFM and TEM studies,[2,5,6] one had to rely on finding

atomically thin BN regions either randomly or close to edges of thick BN flakes. In this Communication, we report optical and Raman properties of mono- and few-layer BN obtained by micromechanical cleavage of high-quality hBN. Because of its zero opacity (the band gap is larger than 5 eV),[1] atomically-thin BN exhibits little optical contrast, even if the interference enhancement using oxidized Si wafers is employed.[14,16] For the standard oxide thickness of ~ 300 nm SiO_2,[6,7] BN monolayers show white-light contrast of <1.5%, which makes them undetectable by the human eye.[17] Moreover, the contrast changes from positive to negative between red and blue parts of the spectrum, respectively, and goes through zero in green where eye sensitivity is maximum. We show that the use of thinner SiO_2 (≈80±10 nm) offers optimum visualization conditions with contrast of ~ 2.5% per layer, similar to that for graphene on transparent substrates in light transmission mode. Mono- and bi- layers can also be identified by Raman spectroscopy due to shifts in position of the characteristic BN peak that is centered at ≈1366 cm^{-1} in hBN crystals.[1] Monolayers exhibit sample-dependent blue shifts by up to 4 cm^{-1}. This is explained by a hardening of the E_{2g} phonon mode due a slightly shorter B-N bond expected in isolated monolayers,[18] with further red shifts due to random strain induced probably during the cleavage. This strain effect dominates in bilayer, causing red shifts of the Raman peak by typically 1 to 2 cm^{-1}.

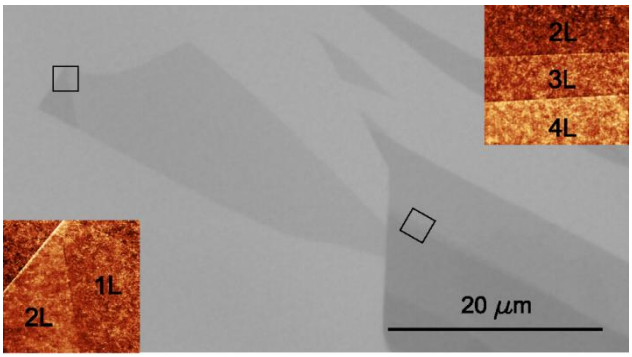

Figure 1. ((Atomically thin BN on top of an oxidized Si wafer (290 nm of SiO_2) as seen in an optical microscope using a yellow filter (λ = 590 nm). The central crystal is a monolayer. For legibility, the contrast is enhanced by a factor of 2. The insets show AFM images of the 3.5x3.5 μm^2 regions indicated by the squares. The step height between the terraces in the images is ~ 4 Å. BN crystals are usually lifted above the wafer by up to extra 10 Å, which can be explained by the presence of a water or contamination layer.[2,6]))

Atomically thin BN crystals were prepared by the standard cleavage procedures[2] and using hBN single crystals grown as described in refs.[19,20] It is important to note that previously we used HOPBN (Momentive Performance Materials) but could only obtain strongly terraced crystallites and no monolayers.[10] BN monolayers mentioned in ref. [2]

were extracted from a powder (*Sigma-Aldrich*) and did not exceed a couple of microns in size because of the small size of initial flakes. Using hBN, we can now prepare few-layer samples larger than 100 μm, that is, comparable in size to our single crystals. **(Figure 1)** shows examples of single- and few- layer BN on top of an oxidized Si wafer. The AFM images in Fig. 1 are to illustrate our identification of regions with different thickness.

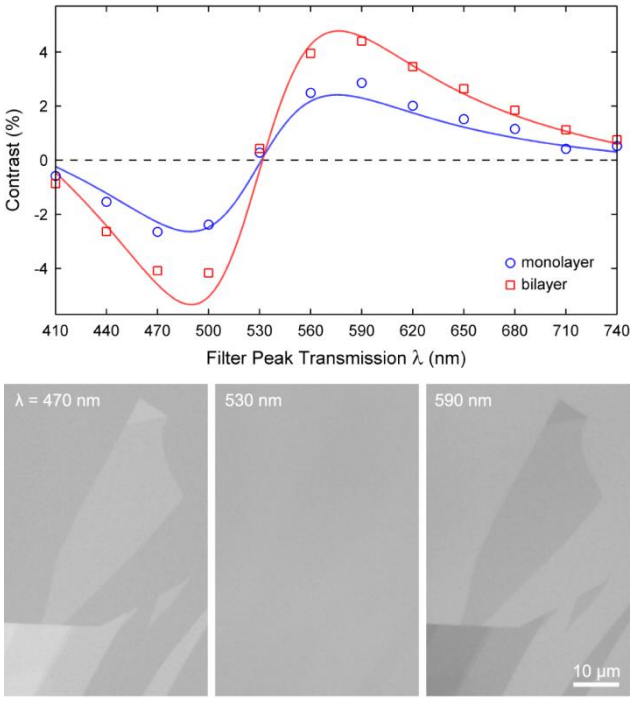

Figure 2. Changes in the optical contrast with wavelength for mono- and bi- layer BN on top of a Si wafer (290 nm SiO_2). We used filters with a 10 nm bandwidth. The solid curves are the dependences expected for mono- and bi- layer BN. In the modeling, we have included the influence of a finite numerical aperture (NA). [21] For the used microscope objective (NA = 0.8), we have integrated over angle assuming a Gaussian weight distribution of width $\theta_{NA}/3$ where θ_{NA} is the maximum acceptance angle of the objective lens.[22] The lower panels show examples of the BN visibility using different filters for the same sample as in Fig. 1. For legibility, the contrast in the images has been enhanced by a factor of 2.

(Figure 2) shows variation of the contrast measured with respect to the bare wafer at different wavelengthsλ. To this end, we have taken optical micrographs using illumination through narrow bandpass filters.[14] Representative images for 3 different λ are also presented in Fig. 2. One can see that the contrast is a nonmonotonic function of λ and changes its sign at ~ 530 nm (BN is darker than the substrate at long wavelengths and brighter at short ones). This is different from graphene, in which case the contrast is either positive or negligible.[14] With increasing the number of BN layers N, the contrast increases proportionally to N. To explain the measured λ dependence, we have used an

analysis similar to that reported for graphene [14] and based on the matrix formalism of interference in thin film multilayers.[16] This requires the knowledge of the real *n* and imaginary *k* parts of the refractive index. We used spectroscopic ellipsometry for our hBN crystals and found k≈0 and n≈2.2 with a slight upshift for λ <500 nm. Assuming that optical properties of monolayers change little with respect to hBN, we obtain the dependences shown in Fig. 2. The theory accurately reproduces the observed contrast, including its reversal at 530 nm and the absolute value that is related to the extra interference path due to the presence of a transparent monolayer on top of SiO_2.

The developed theory allows us to predict at which SiO_2 thickness the optical contrast for BN monolayers would be maximal. **(Fig. 3)** shows that this is expected for a thickness of 80±10 nm. In this case, the contrast remains relatively strong with the same sign over nearly the entire visible range. This prediction has been confirmed experimentally by imaging BN crystals on top of 90 nm SiO_2. We have found that the contrast reaches ~ 2.5% per layer already in white light (~ 3% with a green filter), and this is sufficient to hunt for and directly see BN monolayers in a microscope. Still note that it is much harder to find BN than graphene monolayers that give a contrast of ~ 10%.[14]

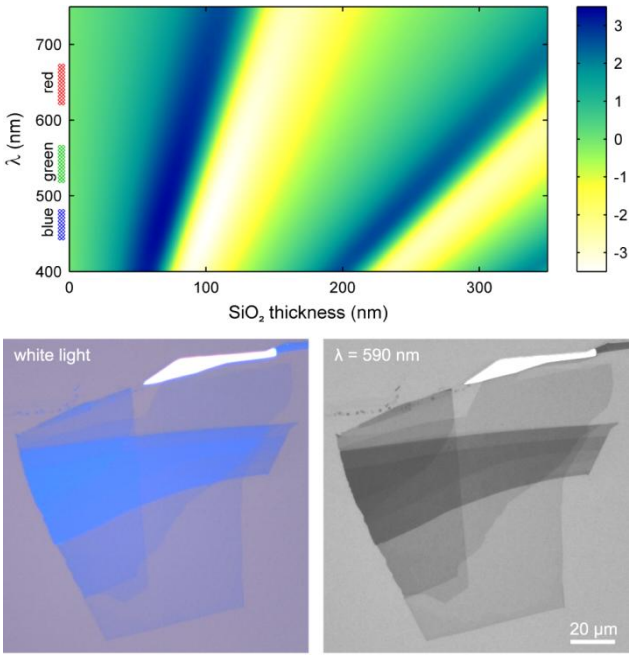

Figure. 3. Optical contrast due to monolayer BN for different λ and SiO_2 thicknesses (top). The plot is for the case of a typical high magnification objective (50X) with NA = 0.8 but changes little for NA = 0.7 or 0.9. The lower images show BN on top of a 90 nm SiO_2/Si wafer (the lower part is a monolayer). Similar to Figures 1 and 2, the contrast is enhanced by a factor of 2.

The optical contrast increases in integer steps (that is, by a factor of N for N-layer BN) and this can be employed for search and identification of mono- and few- layers. However, let us warn that any contamination or a thin layer of water, which is believed to raise atomic crystals above Si wafers, can notably affect the measured contrast. This was previously observed for graphene[22] but the effect becomes much more important for BN because of its weaker contrast. In our experience, it is not unusual for monolayer BN to look like a bilayer. To avoid misidentification and obtain the correct contrast as reported above we annealed our samples at 150 °C in vacuum. For this and other reasons, it is desirable to have another way of confirming BN thickness. Of course, AFM can be used to this end but it is a low throughput technique. For the case of graphene, Raman spectroscopy has proven to be an indispensible tool and, below, we show that it is also useful for identifying monolayer BN.

(Figure 4a) shows Raman spectra of mono-, bi- and tri- layer BN using a green laser with λ = 514.5 nm. BN exhibits a characteristic peak that is due to the E_{2g} phonon mode and analogous to the G peak in graphene.[1,18] In our hBN single crystals, the Raman peak occurs at ≈1366 cm^{-1}. One can see in Fig. 4a that the peak becomes progressively weaker as N decreases and, for monolayer BN, its intensity is ~ 50 times smaller than for graphene's G peak under the same measurement conditions. We have found that the integrated intensity I_T for the BN peak is proportional to N with high accuracy for first several layers (inset in Fig. 4a). Accordingly, once a Raman spectrometer is calibrated for a given substrate, this can be exploited to distinguish between one, two and more BN layers.

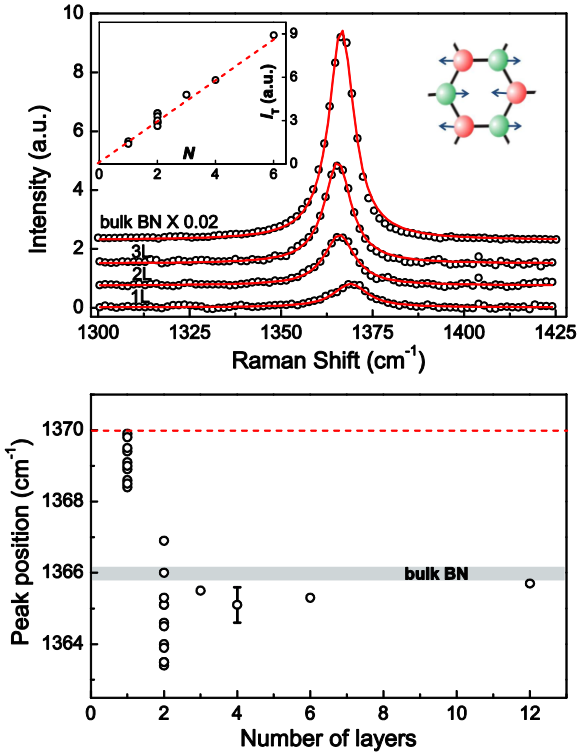

Figure 4. (a) Raman spectra of atomically thin BN. The left inset show changes in integrated intensity I_T with the number of layers N. The right picture illustrates the phonon mode responsible for the Raman peak. (b) Position of the Raman peak for different N. In mono- and bi-layer BN, the peak position is sample dependent and varies by as much as ±2 cm^{-1}. The dashed line is the Raman shift predicted for monolayer BN.[18] The error bar indicates a typical accuracy of determining the peak position using our spectrometer.

In addition to its intensity proportional to N, we have found that the Raman peak is usually shifted upwards in monolayers and downwards in bilayers with respect to its position in bulk hBN (see Fig. 4b). Monolayers show relatively large shifts (typically, between 2 to 4 cm^{-1}), which vary from sample to sample. The maximum observed blue shift is in agreement with the theory expecting its value to be ≈4 cm^{-1} for monolayers.[18] However, Fig. 4 also shows that mono- and bi- layers exhibit unexpectedly strong variations in the peak position whereas these are essentially absent for crystals thicker than 5 layers (not all data for thicker crystals are shown in Fig. 4). To find the origin of these changes, we used different laser powers and ruled out heating effects. We also measured the width of the Raman peaks. The HWHM varied between 10 and 12 cm^{-1} for monolayers and was only marginally larger than the width in hBN (≈9 cm^{-1}). No apparent correlation between the width and peak position was found.

To explain the observed variations, we invoke strain that causes additional sample-dependent red shifts in the case of stretching. This is supported by the theoretical and experimental observation of strain induced shift of the Raman peak for the similar material graphene, where the analogous G peak is red-shifted by as much as ~ 20 cm^{-1} per 1% of strain.[23] Strain-induced shifts in pristine graphene deposited on a substrate are completely masked by doping effects[24] which often move the G peak by ~ 10 cm^{-1}. In the absence of such doping effects for insulating BN, strain is expected to become an important factor in determining the Raman peak position. The observed downshifts with respect to the intrinsic blue shift would then imply the stretching of BN monolayers by only a fraction of a percent, which is highly feasible. It seems pertinent to attribute the peak broadening to the same effect. Indeed, strain can also vary within the micron-sized laser spot as monolayers try following the substrate roughness.[25] This argument also applies for bilayers and can explain their random shifts and notably smaller broadening (HWHM of ~ 9 to 10 cm^{-1}). The maximum observed peak position for bilayers in Fig. 4b implies a small intrinsic blue shift of ~ 1 cm^{-1}. We are not aware of any theory for the intrinsic shift in BN bilayers.

In conclusion, BN mono- and bi-layers can be prepared and identified on top of an oxidized Si wafer using the same mechanical exfoliation technique as widely employed for the case of graphene. BN monolayers obtained from hBN crystals can be as big as samples of cleaved graphene and, therefore, should allow a variety of new experiments and proof-of-concept devices, beyond the previous studies by AFM and TEM. The search for atomically thin BN is more difficult than for graphene as the former does not absorb visible light and, therefore, gives rise only to the contrast due to changes in the optical path. Nevertheless, the use of thinner SiO_2 and/or narrow optical filters makes it possible to see even BN monolayers. To verify the number of layers, one can employ Raman spectroscopy. It allows the identification of monolayers by an upward shift in the Raman peak position. The shift depends on local strain and, therefore, is not as unambiguous as the Raman signatures for mono- and bi- layer graphene. The step-like increase in the Raman intensity can be used for further confirmation and for counting the number of layers. We believe that the provided analysis and the strategy for hunting for mono- and few-layer BN should facilitate further work on this interesting two-dimensional insulator.))

Experimental Section

Experimental optical contrast and images:

Optical images were taken with a Nikon DS-2MBW monochrome camera in the 12-bit raw mode using narrow band filters (10 nm bandwidth). For each filter, 100 frames were averaged to produce the final image. Exposure times varied in the range 10-300 ms depending on filter. The white light images were taken with a Nikon DS-2MV color camera (100 frames averaged).

Calculations of the optical contrast:

The reflectance of the incident light was calculated (taking into account interference and multiple reflections) for each angular step ranging from normal incidence to the maximum acceptance angle of the objective lens (determined by its 0.8 NA). The difference in reflectance was calculated for the cases of (a) bare substrate and (b) substrate with additional BN layer. The total contrast is the difference in reflectance normalized to substrate value integrated over the angle with a weight distribution determined by the experimental conditions (a Gaussian distribution with a width $\theta_{NA}/3$). The refractive index of BN was taken from our own ellipsometry measurements and those for Si, SiO_2 taken from ref. [26].

The Raman studies were carried with a Renishaw micro-Raman spectrometer at 514 nm excitation wavelength. AFM topography images in Fig. 1 were measured in the intermittent contact mode using a Veeco Dimension V scanning probe microscope.

Acknowledgements

The work was supported by EPRSC (UK). We thank Andrea Ferrari for many helpful comments.

[1] ((D. Golberg; Y. Bando, Y. Huang, T. Terao; M. Mitome; C. Tang, C. Zhi, *ACS Nano* **2010**, *4*, 2979.))

[2] ((K. S. Novoselov, D. Jiang, F. Schedin; T. J. Booth, V. V. Khotkevich, S. V. Morozov; A. K. Geim, *Proc. Natl. Acad. Sci. U.S.A.* **2005**, *102*, 10451.))

[3] ((J. C. Meyer, A. Chuvilin, G. Algara-Siller, J. Biskupek, U. Kaiser, *Nano Lett.* **2009**, *9*, 2683.))

[4] ((J. H. Warner, M. H. Rümmeli, A. Bachmatiuk, B. Büchner, *ACS Nano* **2010**, *4*, 1299.))

[5] ((W. Q. Han, L. Wu, Y. Zhu, K. Watanabe, T. Taniguchi, *Appl. Phys. Lett.* **2008**, *93*, 223103.))

[6] ((C. Lee, Q. Li, W. Kalb, X. Z. Liu, H. Berger, R. W. Carpick, J. Hone, *Science* **2010**, *328*, 76.))

[7] ((K. S. Novoselov, A. K. Geim, S. V. Morozov, D. Jiang, Y. Zhang, S. V. Dubonos, I. V. Grigorieva, A. A. Firsov, *Science* **2004**, *306*, 666.))

[8] ((C. R. Dean, A. F. Young, I. Meric, C. Lee, L. Wang, S. Sorgenfrei, K. Watanabe, T. Taniguchi, P. Kim, K. L. Shepard, J. Hone, arXiv:1005.4917, **2010**.))

[9] ((A. F. Young, C. R. Dean, I. Meric, S. Sorgenfrei, H. Ren, K. Watanabe, T. Taniguchi, J. Hone, K. L. Shepard, P. Kim, arXiv:1004.5556, **2010**.))

[10] ((L. A. Ponomarenko, R. Yang, T. M. Mohiuddin, M. I. Katsnelson, K. S. Novoselov, S.V. Morozov, A. A. Zhukov, F. Schedin, E. W. Hill, A. K. Geim, *Phys. Rev. Lett.* **2009**, *102*, 206603.))

[11] ((L. Song, L. Ci, H. Lu, P. B. Sorokin, C. Jin, J. Ni, A. G. Kvashnin, D. G. Kvashnin, J. Lou, B. I. Yakobson, P. M. Ajayan, *Nano Lett.* **2010**, *10*, 3209.))

[12] ((J. P. Eisenstein, A. H. MacDonald, *Nature* **2004**, *432*, 691.))

[13] ((H. Min, R. Bistritzer, J. J. Su, A. H. MacDonald, *Phys. Rev. B* **2008**, *78*, 121401.))

[14] ((P. Blake, E. W. Hill, A. H. Castro Neto, K. S. Novoselov, D. Jiang, R. Yang, T. J. Booth, A. K. Geim, *Appl. Phys. Lett.* **2007**, *91*, 063124.))

[15] ((A. C. Ferrari, J. C. Meyer, V. Scardaci, C. Casiraghi, M. Lazzeri, F. Mauri, S. Piscanec, D. Jiang, K. S. Novoselov, S. Roth, A. K. Geim, *Phys. Rev. Lett.* **2006**, *97*, 187401.)

[16] ((W. S. Bacsa, J. S. Lannin, *Appl. Phys. Lett.* **1992**, *61*, 19.))

[17] ((G. Westheimer, *J. Opt. Soc. Am.* **1972**, *62*, 1502.))

[18] ((R. Arenal, A. C. Ferrari, S. Reich, L. Wirtz, J. V. Mevellec, S. Lefrant, A. Rubio, A. Loiseau, *Nano Lett.* **2006**, *6*, 1812.))

[19] ((K. Watanabe, T. Taniguchi, H. Kanda, *Nat. Mater.* **2004**, *3*, 404.))

[20] ((T. Taniguchi, K. Watanabe, *Journal of Crystal Growth* **2007**, *303*, 525.))

[21] ((C.Casiraghi, A. Hartschuh, E. Lidorikis, H. Qian, H. Harutyunyan, T. Gokus, K. S. Novoselov, A. C. Ferrari, *Nano Lett.* **2007**, *7*, 2711.))

[22] ((M. Bruna, S. Borini, *J. Phys. D* **2009**, *42*, 175307.))

[23] ((T. M. G. Mohiuddin, A. Lombardo, R. R. Nair, A. Bonetti, G. Savini, R. Jalil, N. Bonini, D. M. Basko, C. Galiotis, N. Marzari, K. S. Novoselov, A. K. Geim, A. C. Ferrari, *Phys. Rev. B* **2009**, *79*, 205433.))

[24] ((C. Casiraghi, S. Pisana, K. S. Novoselov, A. K. Geim, A. C. Ferrari, *Appl. Phys. Lett.* **2007**, *91*, 233108.))

[25] ((W. G. Cullen, M. Yamamoto, K. M. Burson, J. H. Chen, C. Jang, L. Li, M. S. Fuhrer, E. D. Williams, arXiv:1007.4802, **2010**.))

[26] ((*Handbook of optical constants of solids* (ed. E. D. Palik), Academic Press,

4.4 Conclusions

Large BN layers can be prepared by the mechanical exfoliation technique as widely used for graphene preparation. Thin layers of BN on oxidized silicon wafer can be identified by optical contrast and Raman spectroscopy. Hunting for atomically thin BN layers is more difficult than for the graphene due to zero opacity of BN. Thin SiO_2 enables to give better contrast for thin BN layers. Raman spectroscopy can be used for counting the number of BN layers on the basis of the BN characteristic peak intensity analysis and monolayer BN can be distinguished by an upward shift in peak position whereas the shifts are dependent on the local strain. Therefore two dimensional insulator BN layers for different experiments and applications can now be prepared and identified successfully.

Chapter 5

Mechanical Transfer of Nano-structures

5.1 Introduction

Graphene is a single atomic layer of carbon atoms arranged in a form of honey comb lattice. The possibility of depositing and observing this material on Silicon substrates with a specific oxide thickness made it possible to investigate the 2D graphitic system [1,14]. It also lead to the exploration of its remarkable mechanical [71], electronic [96] and optical [74] properties giving rise to an array of applications including thin film transistors, electrodes and transparent and conductive composites [16,54,75,119]. In the case where Silicon is used as a substrate, the true potential of graphene electronics cannot be explored and as such, it is necessary to study graphene on other substrates.

There has been no significant improvement in the carrier mobility of graphene and it is still around ~10^4 $cm^2V^{-1}s^{-1}$on oxidised silicon surface [14]. There are various arguments for this low mobility on Si/SiO_2 substrate like the presence of trap charges [120], surface roughness [107] and surface phonons [20]. It is believed that the above mentioned factors are playing vital role in limiting the mobility. Perturbation to graphene can be minimised by removing the substrate and as such, mobility of graphene suspended devices has been reported to be ~ 200 000 $cm^2V^{-1}s^{-1}$at room temperature [15].

A recent breakthrough in supported graphene mobility was due to hexagonal boron nitride (hBN) crystal being used as substrate for graphene. Mobilities of graphene devices on hBN substrates are reported ~120 000-140 000 $cm^2V^{-1}s^{-1}$at room temperature [24,30,64] and ~275 000 $cm^2V^{-1}s^{-1}$ at T = 4.2K [64]. In order to make these types of devices, precise graphene transfer is needed.

In this chapter, the transfer of graphene flakes on other crystals like hexagonal boron nitride (hBN) and mica is described briefly. The presence of graphene on these crystals is investigated by optical contrast, Raman spectroscopy and atomic force microscopy (AFM).

5.2 Review of Graphene Transfer Techniques

In 2004, Graphene was successfully prepared on silicon substrate with a selected oxide layer thickness [1]. Up until now, Si/SiO_2 substrates were used extensively in order to gain a deep understanding of the properties of this two dimensional material. To investigate the substrate's influence on graphene's electronic properties, graphene was initially transferred from one substrate to another substrate at any arbitrary location [28]. Graphene exhibits remarkable improvement in its electronic properties when studied on other flat crystals like hBN, mica ect. The most crucial step in producing these types of devices is the transfer of graphene from one substrate to a precise location, i.e. another crystal flake.
In this section, a graphene transfer technique which gives a few micron accuracy with high output yield is discussed. There are two main transfer techniques routinely used for precise transfer

- Wet transfer Technique
- Dry Transfer technique

5.3. Wet Transfer Technique

The electronic quality of graphene devices strongly depends upon its interaction with the substrate [107]. Surface roughness can limit the graphene charge carrier mobility. Substrate free graphene (suspended) on the other hand shows very large mobility of charge carriers [15]. In this section, transfer of a particular graphene flake to a precise location is explained.

5.3.1 Graphene flakes preparation and lift-off

Graphene flakes were first prepared on oxidised silicon substrate with oxide thickness of 300nm by micromechanical cleavage, explained in chapter 2, section 2.4.1. Single layer, *bilayer* and few layer regions were identified and mapped using optical contrast microscopy. Later, these same graphene flakes were transferred precisely on to other substrates.

This transfer technique can be explained in to two parts

i) Lifting of graphene flake from a substrate using tape window.

ii) Precise transfer on to another substrate.

In the first part of the transfer process, a selected graphene flake was lifted from Si/SiO_2 substrate by wet etching of underlying silicon oxide.

For this, a thin layer (~300nm) of PMMA resist 950-A3 was spin coated on the surface of the sample. Then sample was then heated at $120C^0$ for 10 minutes in order to remove any solvent from the resist. Fig 5.1 show the optical contrast of a selected graphene flake after spin coating the PMMA resist layer. The blue dots seen on the flake were due to air bubbles underneath large graphene flake. These bubbles usually appear under large graphene flakes sometime after their preparation.

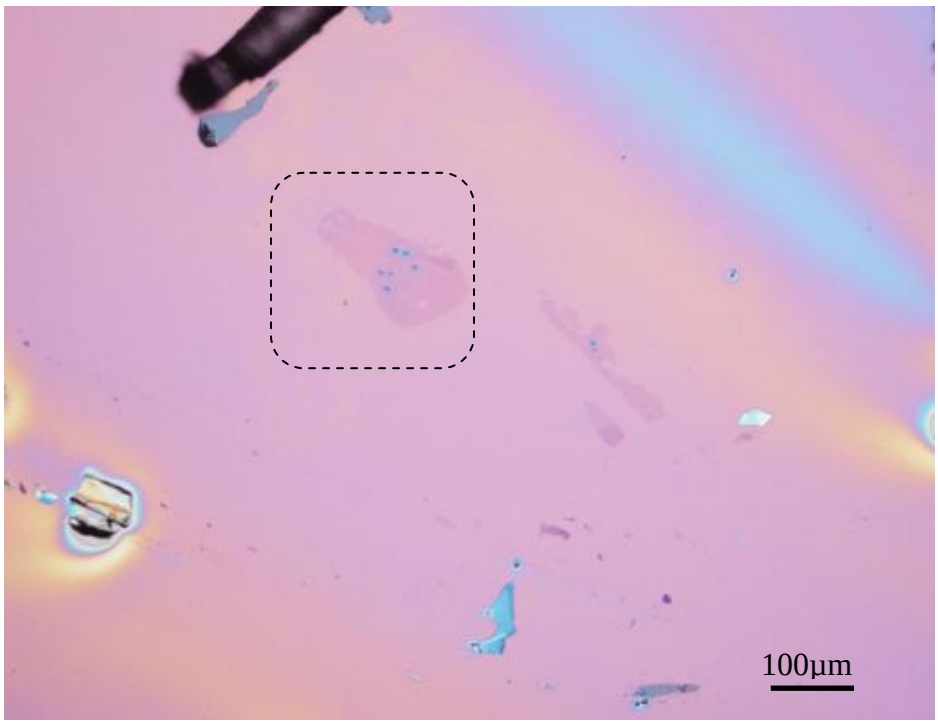

Figure 5.1: Graphene on Si/SiO_2 substrate coated with PMMA resist layer.

After coating the PMMA resist, a tape window was place around the flake as shown in fig. 5.2(c) with the adhesive side of the tape attached to PMMA resist. The window size, usually used during transfer is (1mm x 1mm). To isolate the tape window from rest of PMMA layer on substrate, the outer boundary of the tape window was scratched. Etching of silicon oxide was carried out using 3% (w/w) of potassium hydroxide (KOH) solution.

The sample was then transferred into a beaker containing the above mixture as shown in the Fig. 5.2 (e) and then heated at $40C^0$. After some time, the KOH etched away few nanometres of the silicon oxide layer and detached the tape window from the substrate as shown in Fig. 5.2(f). Finally, the tape window which was carrying the graphene-PMMA membrane was transferred into DI water Fig. 5.2(g). It was rinsed several times in DI water in an attempt to remove any traces of KOH.

Steps involved in lifting a graphene flake from a substrate are schematically shown in Fig. 5.2.

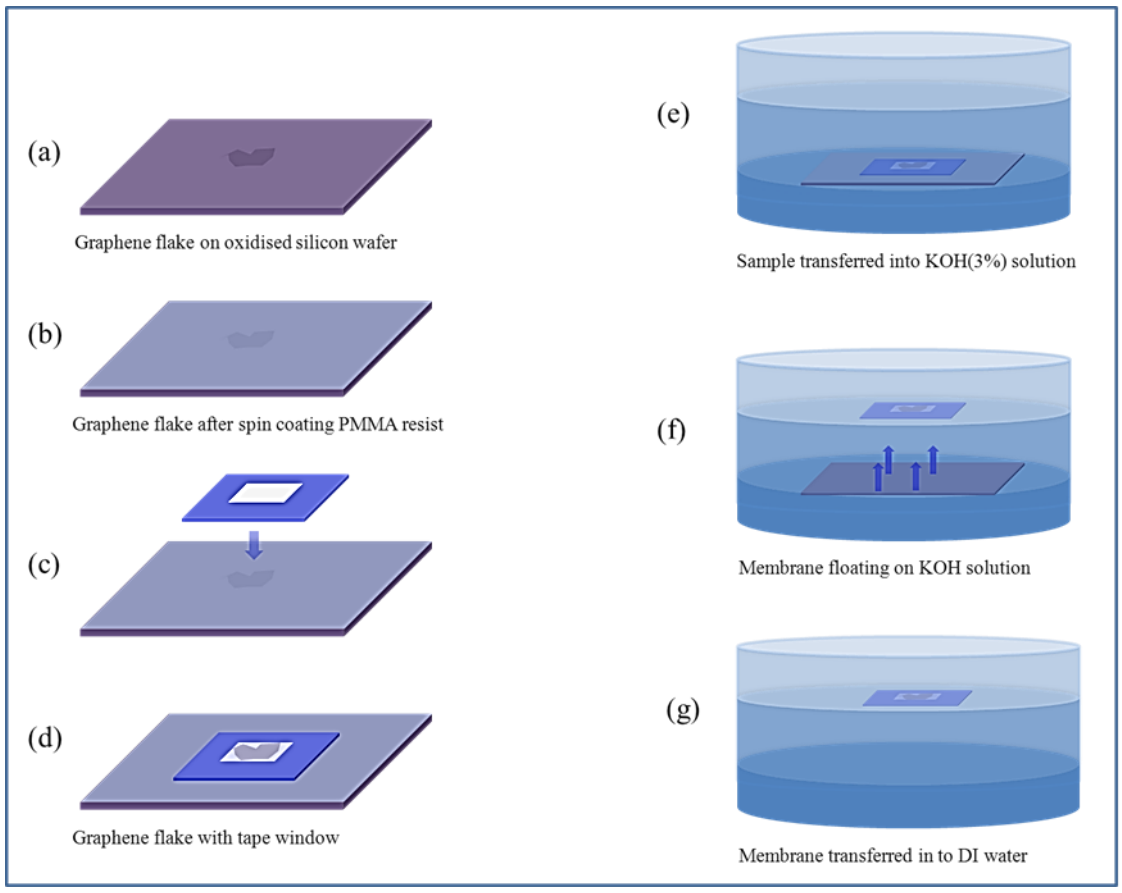

Figure 5.2: schematic of graphene transfer by wet- etching using KOH solution.

5.3.2 Alignment Procedure

The precise flake alignment was achieved by using an MJB-3 mask aligner. It is a delicate instrument which is commonly used for optical lithography. It has a moveable stage with x,y,z directional controls. A little modification was required to use it for the flake transfer process. Instead of using a conventional mask holder, a transparent sheet (of what material) with a hole at its centre was used as a holder for the tape window. The tape window carrying graphene-PMMA membrane was carefully attached to the mask using a double sided tape, as shown in Fig. 5.3 (a).

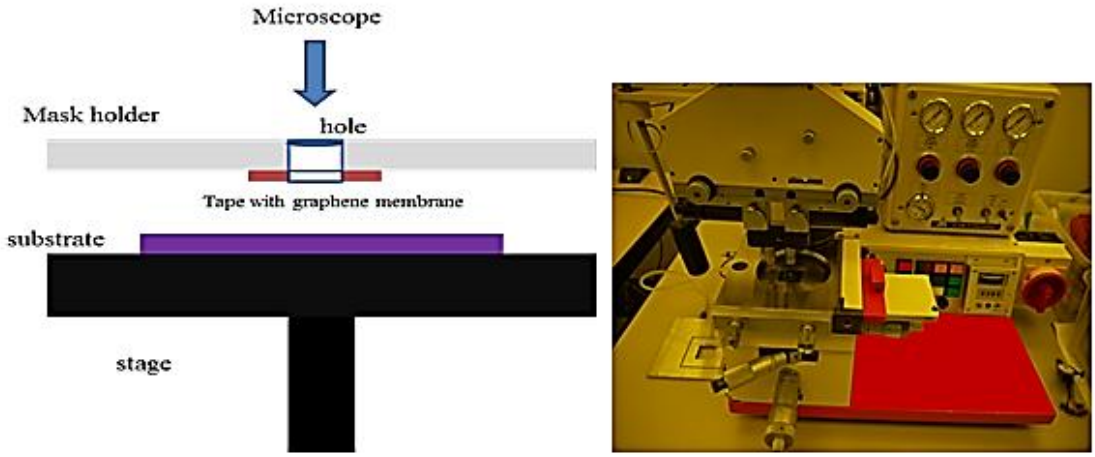

(a) (b)

Figure 5.3: (a) Schematic of alignment setup (b) MBJ3 mask aligner

The target sample, on which graphene transfer was required, was placed on the stage of the mask aligner. Any specific location on the sample may be brought in focus using microscope controls. After that the substrate was move closed to the membrane by moving mask aligner stage upwards using the Z-control of stage. For accurate alignment, the position of graphene flake against its transfer location on substrate was observed several times by viewing through the microscope.

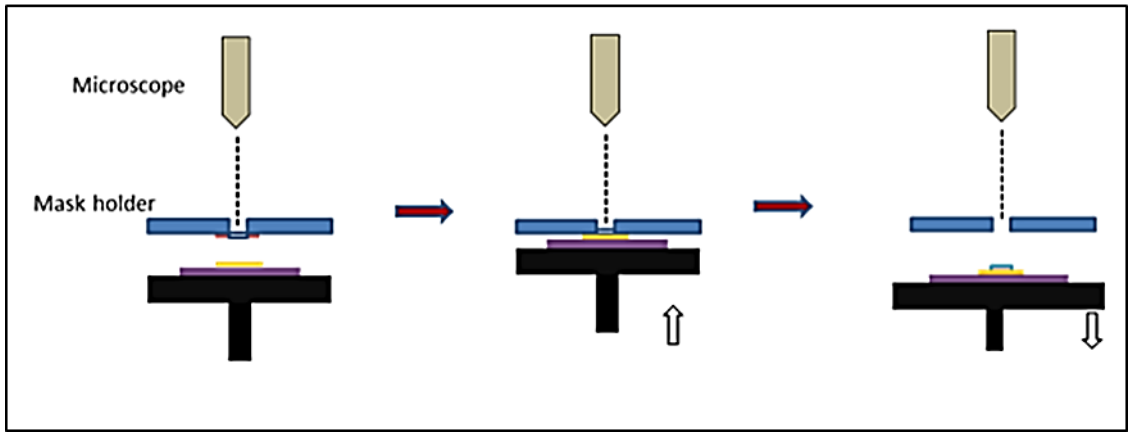

Figure 5.4: schematic of accurate transfer of flakes.

Finally, the stage was moved up further using Z-control of mask aligner stage so that membrane attached to the substrate as shown in Fig. 5.4. The inner boundary of the tape window was scratched then in order to detach the membrane from tape, the stage moved down.

Graphene has now been transferred on the substrate/sample with thin PMMA resist layer covering it. The sample was heated at $120C^0$ for 5 minutes to dry the membrane. It was then washed in acetone for 10 min to dissolve the PMMA resist layer and then transferred to isopropanol (IPA) for 5 minutes. Finally, the sample dried with nitrogen. Some examples of the flake transfer by this technique on different substrates are shown in Fig. 5.5.

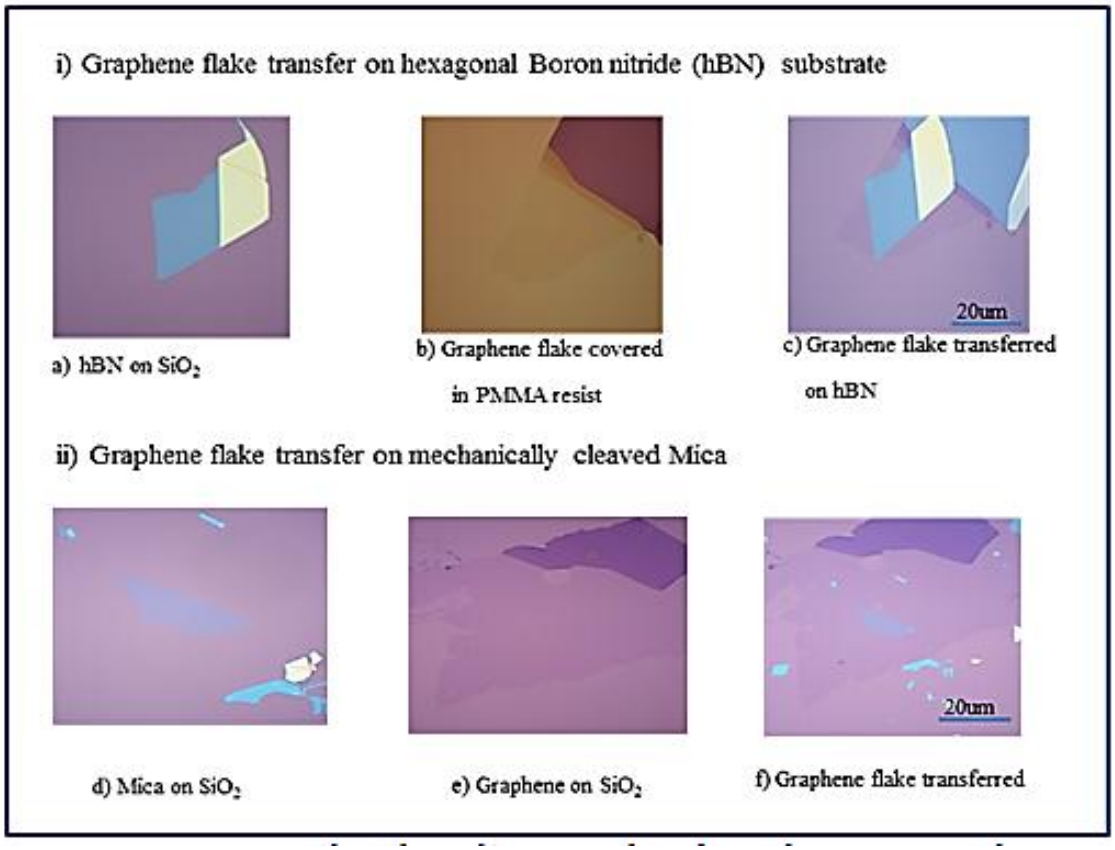

Figure 5.5: Examples of graphene transferred on other 2D materials

5.3.3 Raman analysis of transferred Graphene

The presence of the graphene on substrates can be identified using Raman spectroscopy [27]. It is a reliable technique widely used for graphene signature. The Raman spectra of transferred graphene are taken on two different substrates i.e., on hexagonal Boron nitride and other mechanically cleaved mica on oxidised silicon.

The Raman peak of Boron nitride is centred at 1366.5 cm^{-1} [10] where as two prominent peaks of un-doped graphene is the G-peak centred at 1580cm^{-1} and the 2d peak at 2680 cm^{-1}. The presence of the graphene on top of hBN substrate is represented in orange spectrum Fig. 5.6 (left). In case of mica, no prominent peak is observed in the given frequency range and graphene transfer on mica is shown in red spectrum Fig. 5.6 (right).

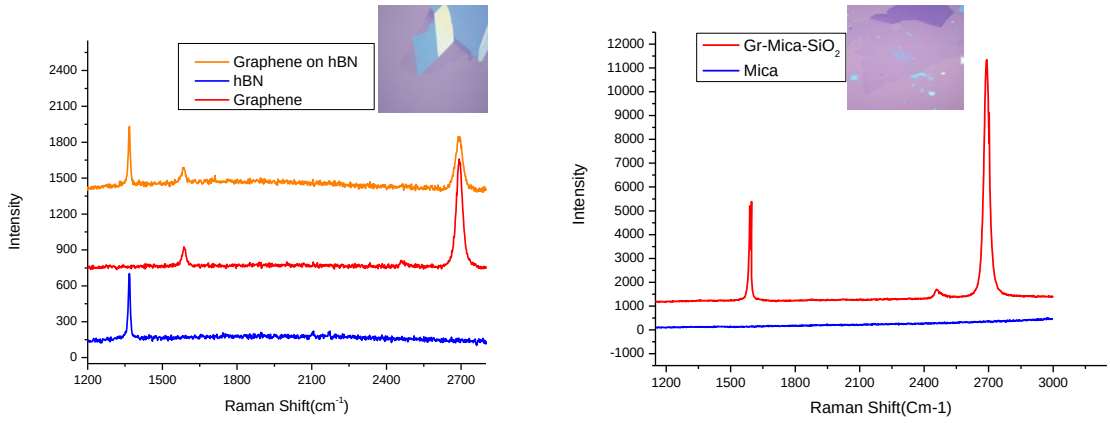

Figure 5.6: Raman spectra of graphene flake transferred on hBN (left) and mice substrate(right)

5.3.4 AFM analysis of transferred Graphene

Graphene can also be identified by measuring step height of a particular flake with the aid of an atomic force microscope (AFM). We can also observe the contamination produced as result of a transfer. Fig. 5.7(b) shows an AFM image of a graphene flake which was transferred on mica by wet transfer technique. The white spots on the AFM image were due of PMMA resist. One can minimise the contamination by additional solvent cleaning (Acetone & Shiply 1165) and annealing the sample at elevated temperature in Ar-H_2 atmosphere.

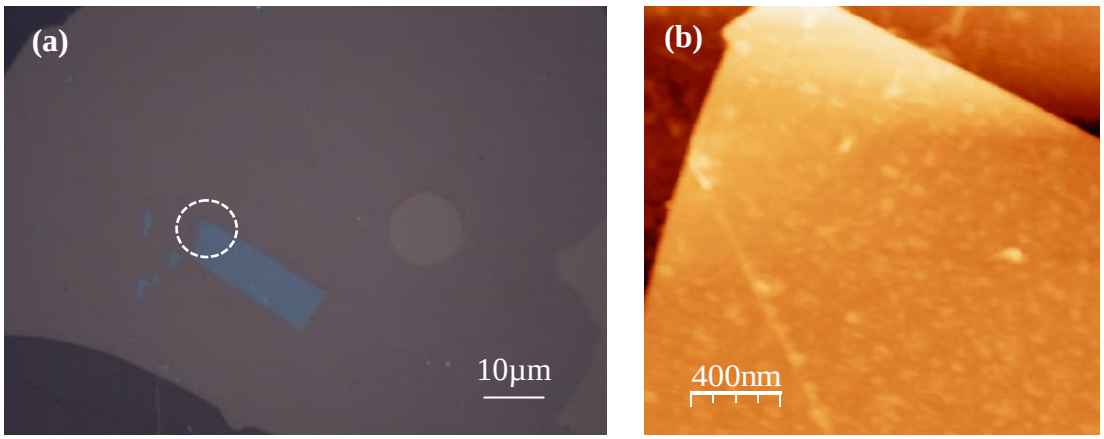

Figure 5.7: (a) optical image of graphene transferred on mica. (b) AFM micrograph of graphene on mica (right).

5.4 Flake transfer recipe for TEM Grid

The above described wet transfer technique is also useful for making TEM samples. It is often observed that flakes are not transferred to desired location on TEM grids. The reason for this is that during the making of samples for TEM, the floating membrane of graphene encapsulated in PMMA in DI water, is taken out with TEM grid. Therefore, the flake can stick at any place on the grid. If flake is transferred on the frame of the grid then it is impossible to investigate it and the sample is therefore useless.

In this section a new technique for making TEM samples is described which allows us to transfer graphene to any particular location on the TEM grid (Quantifoil). Sample making for TEM consists of two parts:

During first part, graphene flake or any other desired material flake (MoS_2, BSCOO, WS_2, Mica etc.) is lifted up from the substrate by wet etching as explained in section 5.2.1 of this chapter, then tape window carrying Graphene-PMMA membrane is transferred into DI water. A relatively large window size is used in this case; i.e. it should be larger than the grid diameter. The larger window size permits us to cut the inner boundary of the PMMA membrane with ease during flake transfer process. Figure 5.8 represents the schematic of tape window used for TEM grid.

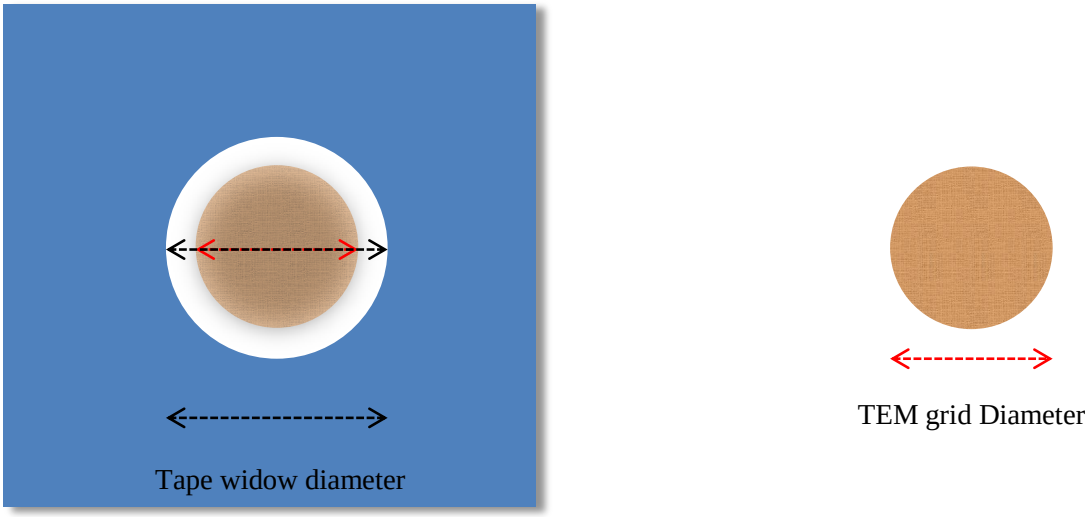

Figure 5.8: schematic of window size to the TEM grid dimensions.

The second part deals with the alignment procedure for graphene transfer on TEM grids. The mask aligner (Karl Suss MJB-3) was modified to use it for this purpose. A glass slide was placed on the mask aligner stage and TEM grid was put on to glass slide. Another glass side was used to mount the tape window carrying the graphene membrane. A schematic of this modified setup is shown in the Fig. 5.9.

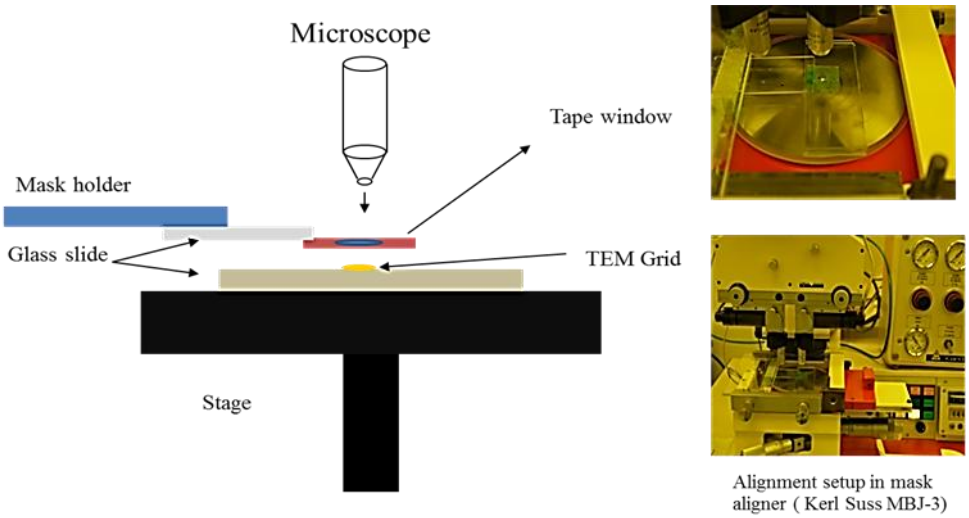

Figure 5.9: Schematic of setup for the precise alignment for TEM samples.

Then mask aligner stage was moved close to the tape window. Alignment of the graphene flake on membrane to the desire location on grid was adjusted several times via the microscope and stage (x, y) controls. Once flake has been aligned correctly, the mask aligner stage was moved further up until grid was in contact with the graphene flake. The inner boundary of the tape window was now scratched with a tweezer to separate grid from rest of membrane. The mask aligner stage was then moved down and Grid was baked at $90C^0$ for 15 minutes. Finally, the PMMA resist layer was removed by solvents and dried using a critical point dryer (CPD). Some examples of TEM samples made by this technique are shown in Fig. 5.10.

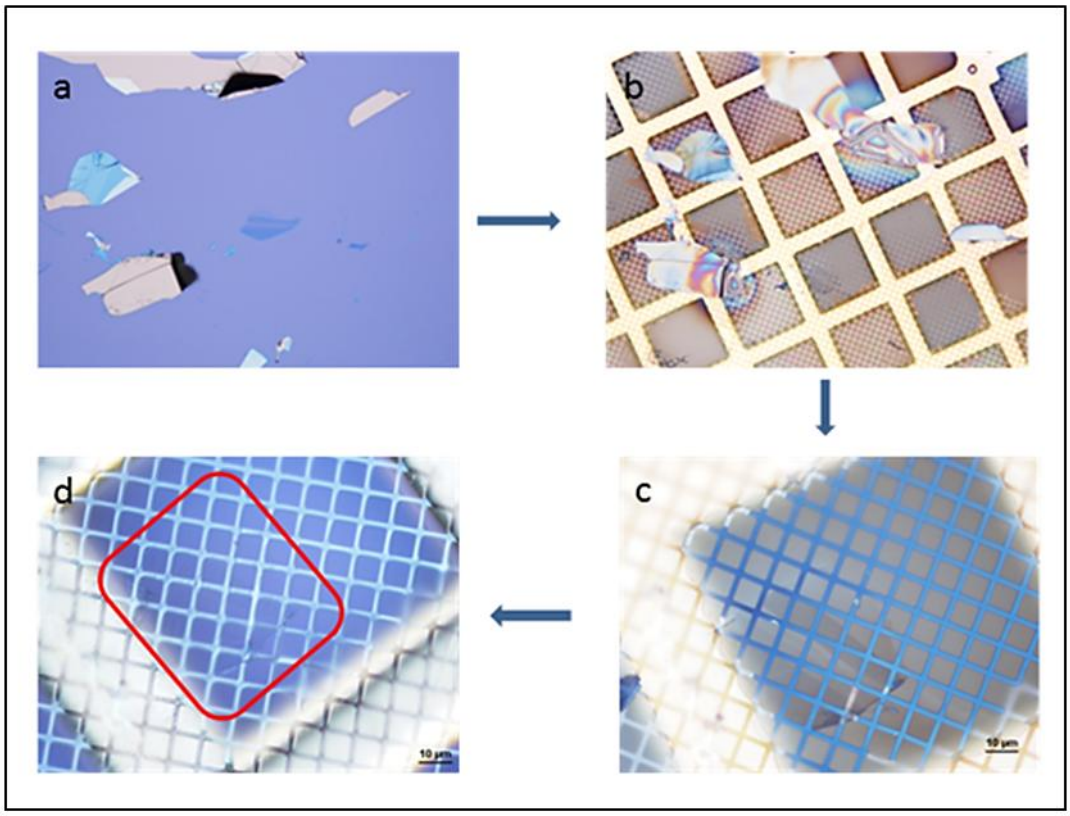

Figure 5.10: (a) Graphene flake made by mechanical cleavage of graphite on oxidised silicon substrate. (b) Flake transferred on TEM grid with PMMA resist. (c) 50x zoomed optical image of graphene flake with resist on top. (d)optical image of graphene flake after removing PMMA resist by critical point dryer(CPD).

5.5 Dry transfer technique

In this section another technique for graphene transfer is explained. It is called Dry transfer technique because the graphene surface is not exposed to solvents or any other liquid throughout the transfer procedure ensuring the interface is extremely clean.

This technique can be explained in three steps

i) Graphene exfoliation

ii) Flake lift off

iii) Alignment procedure using Mask aligner (Kerl Suss) MBJ-4

5.5.1 Graphene making recipe and lift-off

In the first step of the dry transfer technique, graphene flakes were prepared by micromechanical cleavage. In conventional methods of graphene exfoliation, solvents are used at different steps i.e. for tape release etc, whereas in this case no solvents were used during graphene preparation. A special substrate which was a single side polished silicon wafer coated with bi-layer resist was prepared for this purpose.

To prepare the sample, the silicon wafer was firstly dehydrated at 200C for 5min. Then a photo-resist (PMGI) was spun coated at 4000rpm for 1min, with ramp of 4000m/s^2 and baked at 130C^0 for 5minutes. The resist thickness was around 200nm. Next, another resist layer (PMMA 950 with 6% anisole) was then spun at 7500rpm for 1min. The sample was again baked at 130C^0 for 5min. The combined thickness of resists was ~500nm. The optical contrast of substrate before and after spinning the bilayer resist is shown in Fig. 5.11.

Figure 5.11: (a) single side polished silicon substrate (b) optical contrast of sample with bi-layer resist.

Adhesive tape was used prepare graphite pieces until there was adequate coverage. The tape was then pressed on to the resist covered silicon and even pressure was applied for 30s with the aid of a rubber pad. The tape was then removed from the substrate by simple peeling it back. The procedure is shown in Fig. 5.12.

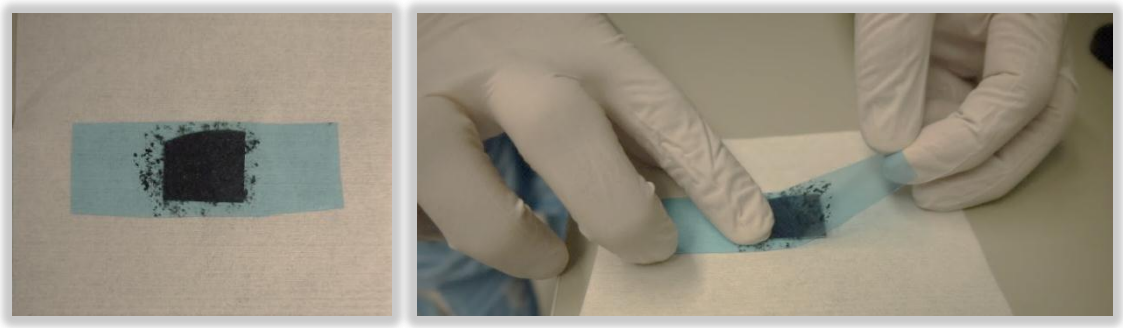

Figure 5.12: (a) adhesive tape with cleaved graphite placed on sample (b) Mechanical peeling of tape.

Different optical filters (410nm-680nm) were then used in the microscope to enhance the visibility of graphene on the substrate [9], As observed in Fig. 5.13, for this particular sample, the red filter (620 nm) gave maximum contrast.

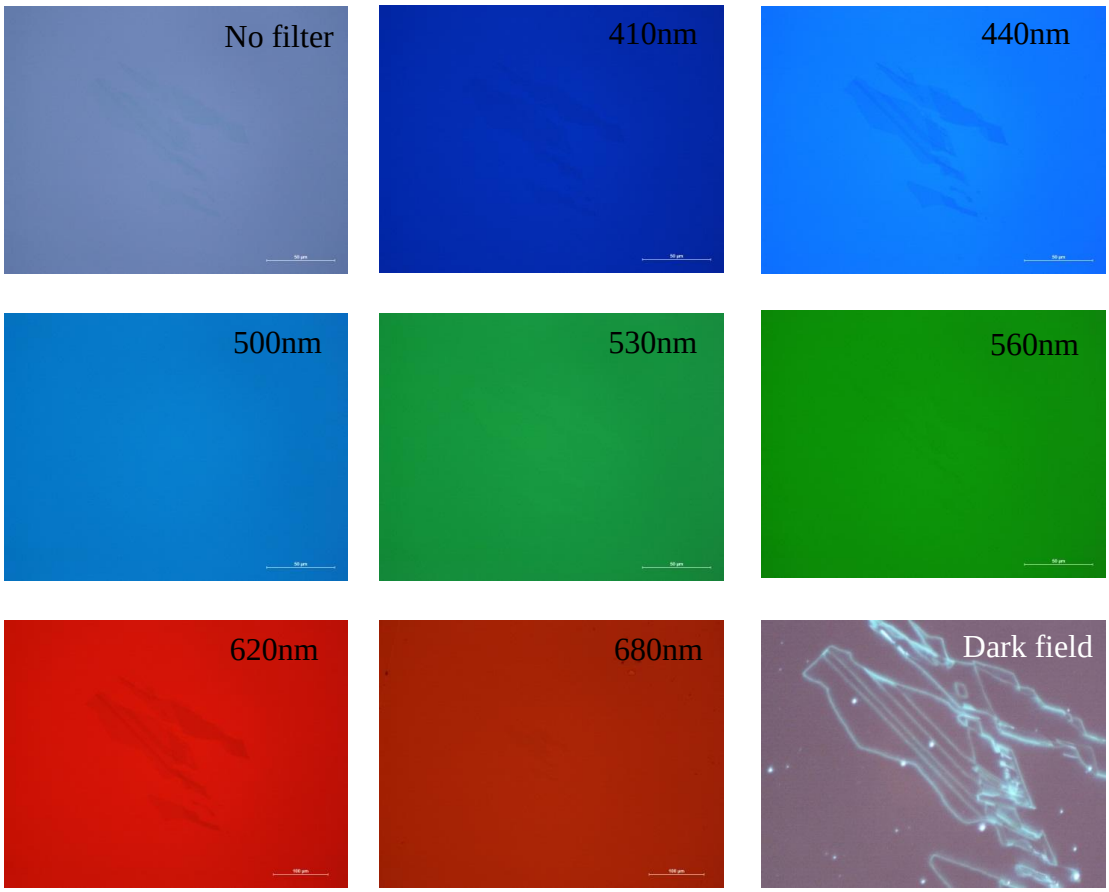

Figure 5.13: optical image of graphene flake using different filter range. Scale length is 50μm.

5.5.2 Flake lift off procedure

In order to lift the graphene flake from the substrate, the resist across the boundary of the flake was scratched in a circular shape. Photo resist developer (MF-319) was carefully applied to the scratched area which caused the bottom layer to be dissolved. The top layer is insoluble in this developer and thereby remained unaffected as shown in Fig. 5.14.

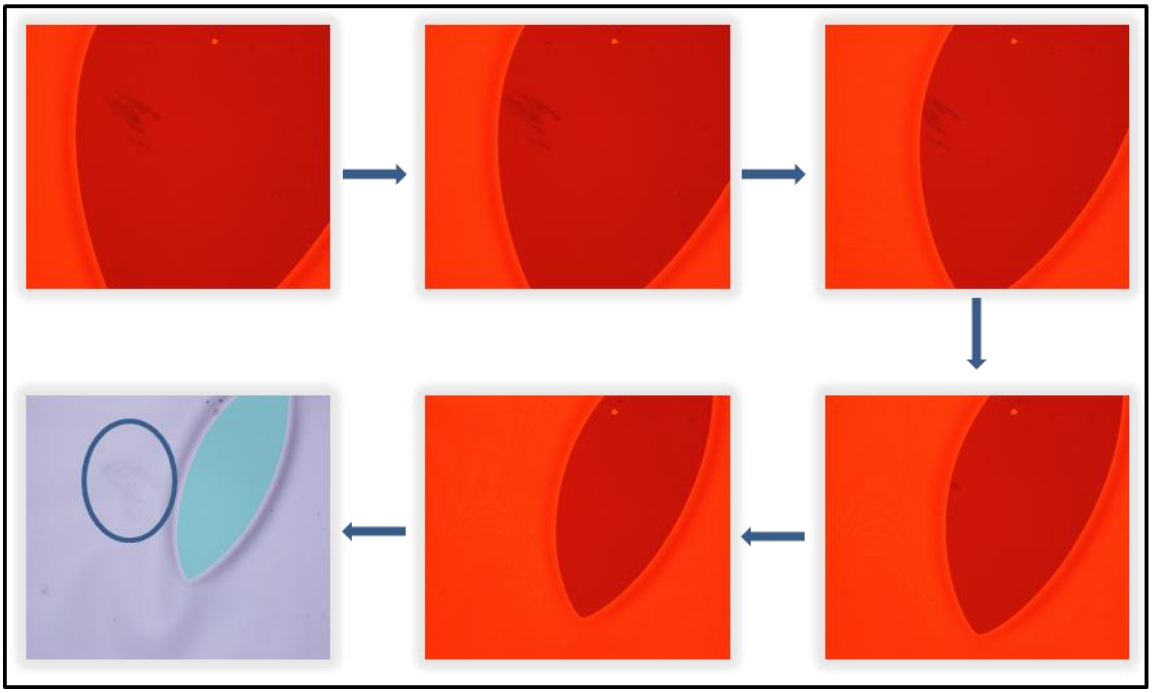

Figure 5.14 optical images of graphene flake lifting at different stages by developer (MF-319).

After the membrane was fully detached and floating, it was carefully transferred to DI-water in another beaker. DI water dissolves the developer (MF-319) making the PMMA membrane cleaner. Up till this stage, the surface of the graphene flake has not been exposed to any solvent. Then membrane was then transferred on to a metal ring. It was achieved by dipping the metal ring into DI-water and carefully lifting it up to suspend the membrane on it.

5.5.3 Alignment procedure

Instead of using MJB-3 mask aligner, in the dry transfer technique an MJB-4 mask aligner was used for Flake alignment. The stage was modified such that sample may be heated during the flake transfer procedure. Unlike a transparent sheet used as mask in wet transfer technique, here a metallic disk with a hole at its centre was used. The metallic ring containing graphene membrane was mounted on disk using double sided adhesive tape. For flake alignment the same procedure was follow as explained in section 5.2.2 of this chapter. The dry transfer of graphene flake on a thick hBN flake using mask aligner (Kerl Suss MBJ-4) is shown in Fig. 5.15

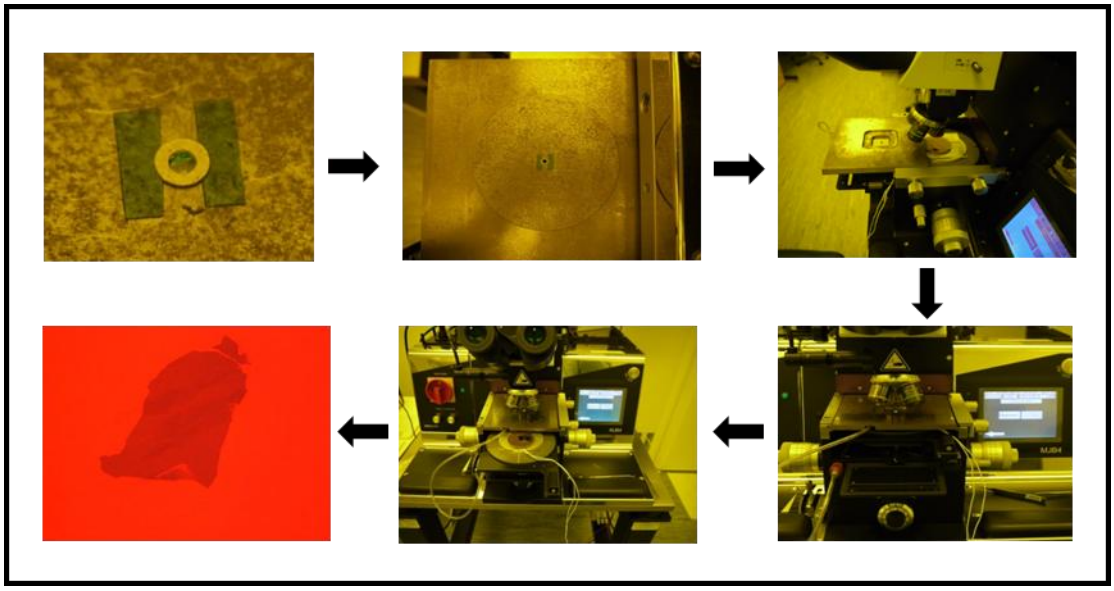

Figure 5.15: Schematic of dry Flake transfer technique using mask aligner (Kerl Suss MJB-4)

5.6 Comparison of Transfer techniques

In this section a comparison between dry and wet transferred techniques is made especially for graphene-hBN hetero-structures. Bubbles appear whenever graphene is transferred on hBN (used as substrate). These bubbles are usually few nanometres high and several hundred nanometres in width. It is believed that there are always some contamination (hydro-carbons) on hBN surface which latterly trapped between graphene and boron nitride interface. Initial investigation about nature of these bubbles revealed that material trapped in these bubbles composed of hydrocarbons with carbon and oxygen its major components. These bubbles are often connected to each other via narrow channels. SEM image of such bubbles for another sample is shown below.

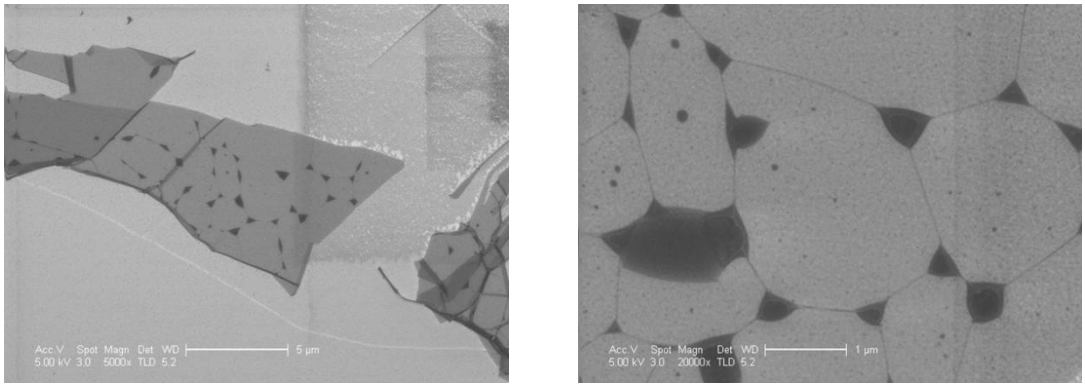

Figure 5.16: SEM image of bubbles produced on graphene flake transferred on top of hBN substrate.

The bubbles are usually triangular in shape as it can be seen on SEM micrograph shown in Fig. 5.16. In some cases of graphene transfer, no bubbles appear as result of the transfer. It does not necessarily mean the absence of bubbles, actually either graphene or hBN (substrate) or even both graphene and hBN are not clean enough and have contaminants presumably hydrocarbons on their surfaces. When such samples are annealed at elevated temperature, bubbles re-appear at the interface. However, large bubble-free regions are seen if a graphene flake is transfer on pre-heated substrate (hBN).

Similarly annealing the samples in Ar-H_2 atmosphere at elevated temperature may result in generating bubble free graphene regions as well. Fig. 5.17 is a comparison of bubbles between graphene and hBN interface before annealing and after annealing in Ar-H_2 atmosphere at $300C^0$ for 3 hours.

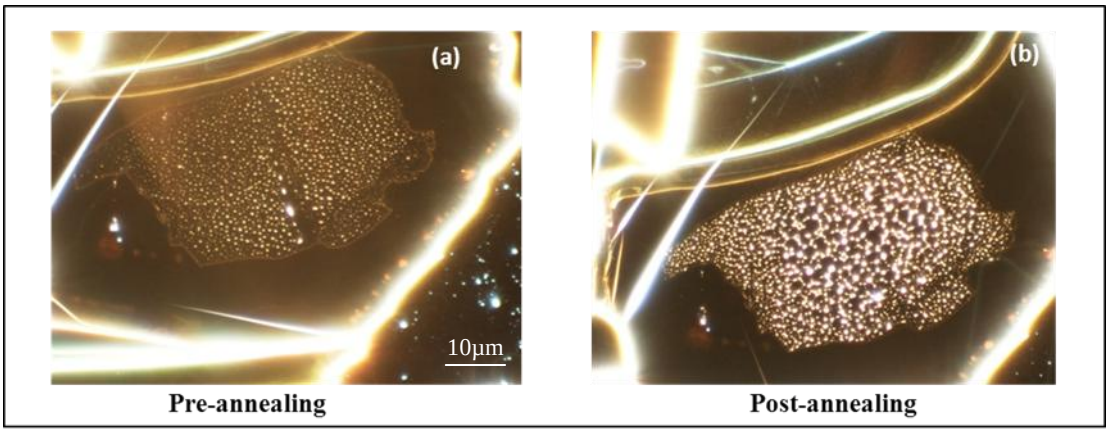

Figure 5.17: Comparison of bubbles on GBN surface (a)Dark field image of GBN structure before annealing. (b) Dark field image of the GBN structure after Ar-H2 annealing.

It is found that in dry transfer technique; bubbles concentration is lesser than the wet transfer process. In optical microscopy these bubbles are hardly seen in white light image. Dark filed mode of the microscope gives better view of these bubbles. Fig.5.18. shows a comparison of bubbles formed as result of dry and wet transfer techniques. Clearly fewer bubbles (~20% less) are observed in case of dry transferring technique.

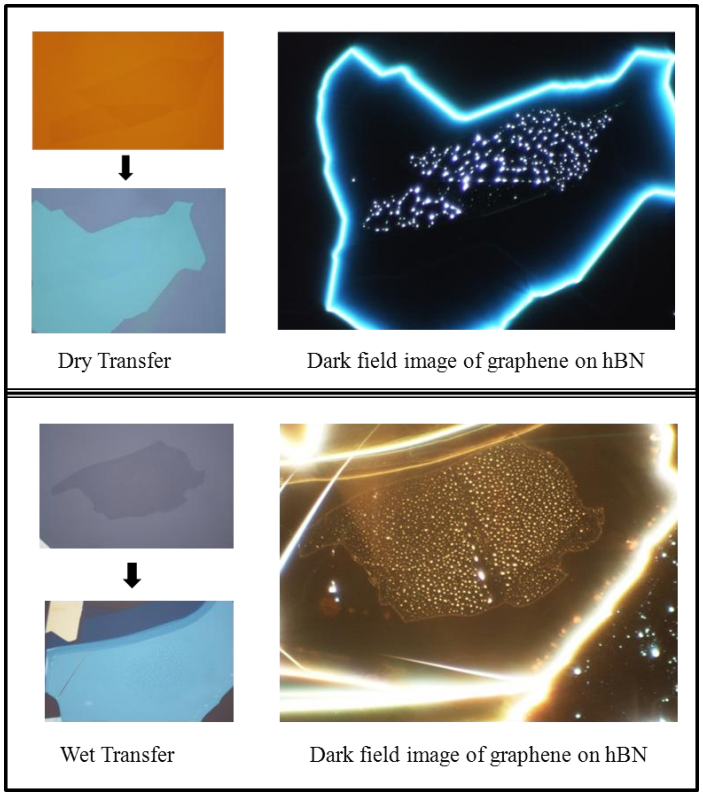

Figure 5.18: White light and Dark field images of two graphene flakes transferred by dry and wet flake transfer techniques

Dry transfer technique permits us to transfer graphene on pre-heated substrate because graphene-PMMA membrane is suspended on metal ring. In case of wet transfer procedure it is not possible due to tape window since it would melt on the substrate at higher temperatures and would contaminate the surface.

On other hand success rate of flake transfer by wet transfer technique is more than in dry transfer. It is due to fact that in wet transfer, graphene-pmma membrane is flatter on tape window than in dry transfer where membrane is supported by metallic ring, thus makes alignment easier during flake transfer.

5.7 Applications

Most recent breakthrough in high mobility graphene devices was achieved by using hexagonal boron nitride as an inert and atomically smooth substrate for graphene [24,30,64]. High mobility samples have allowed us to probe in to different phenomena. With the addition of another hBN layer (transferred) on top of high mobility devices, environmental effect was eliminated on such devices. Ballistic transport ~3µm have been reported in these encapsulated G/BN devices [30]. The schematic of these devices made on hBN substrates are shown in Fig. 5.19.

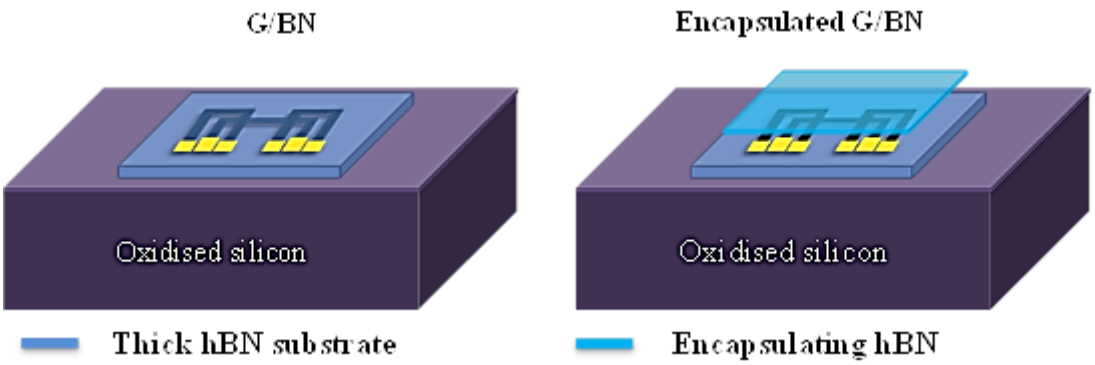

Figure 5.19: schematic of graphene Hall bar device on hBN substrate (left) and encapsulated graphene Hall bar device on BN substrate(right).

The next stage of devices concerned to a system in which two graphene flakes (hall bars) were separated by a thin spacer of boron nitride. The in-plane transport allowed us to study tuneable metal insulator transition in double-layer graphene system [26].

Similarly filed effect tunnelling transistor has also been reported by using a thin barrier of hBN layer [25]. Figure 5.20 is a schematic of double- layer graphene system separated by thin layers of hBN.

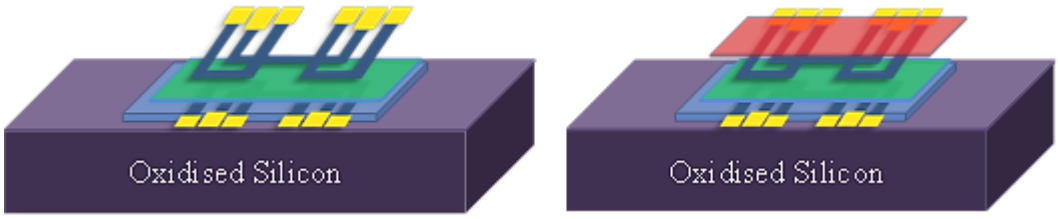

Figure 5.20: schematic of double layer graphene Hall bar device on hBN substrate (left) and encapsulated double-graphene Hall bar device on BN substrate(right).

5.8 Conclusions

The transfer of graphene flakes from one substrate to another substrate at a specific location is explained in this chapter. Both wet and dry transfer techniques are routinely used in device fabrication process. These transfer techniques are not only applicable for graphene flakes but for other 2D materials e.g., Hexagonal boron nitride, BSCOO, Molybdenum disulphide.

These transfer techniques enabled us to study graphene's electronic properties on different substrates like on hBN substrate which until now has shown highest graphene mobility for a supported graphene device. This has allowed us to probe into a verity of new phenomena like Millimetre scale ballistic transport of graphene, coulomb drag etc.

Chapter 6

Ballistic Transport in Graphene-Boron Nitride Heterostrutures

6.1 Introduction

The intrinsic high electronic quality of graphene on standard Si/SiO_2 substrate is not optimum due to the interaction between graphene and SiO_2 surface [107]. The charge carrier mobility of mechanically cleaved graphene on Si/SiO_2 is usually ~10 000 $cm^2V^{-1}s^{-1}$ at charge carrier densities ~$10^{12}cm^{-2}$ [14]. These values turn into the charge carrier mean free path of the order of sub-micron. Suspended graphene devices are a possible solution since we can eliminate the role of underlying substrate limiting the intrinsic electronic characteristics of graphene. The mobility for suspended graphene devices reaches as high as 200 000 $cm^2V^{-1}s^{-1}$ at charge carrier densities ~$10^{11}cm^{-2}$ indicating the high electronic quality of these devices [15]. Suspended graphene devices are fragile and difficult to handle with low yield in addition to the difficulty of fabrication a suspended four probe geometrical device.

Therefore, there still exists a need to improve the electronic quality of the substrate based graphene to search new phenomena by fabricating variety of complex device structures that are much more difficult to make without substrate. A smooth and inert substrate for graphene has been required and hunted for long [108]. In 2010, hexagonal boron nitride (hBN) emerged as the ideal substrate for graphene [24]. The mobility of exfoliated graphene on hBN substrates for charge carrier density $10^{11}cm^{-2}$ reaches $\sim 100\ 000\ cm^2V^{-1}S^{-1}$ [24,64]. These values give the charge carrier mean free path of 1 μm but no evidence of ballistic transport has been demonstrated.

To this end, graphene boron nitride (G-BN) heterostrutures have enabled us to study room temperature ballistic transport [30]. The graphene devices were made on an hBN substrate and were then encapsulated another hBN layer. The measured devices exhibit room temperature mobility $> 100\ 000\ cm^2V^{-1}S^{-1}$ at low charge carrier density $\sim 10^{11} cm^{-2}$.

To study ballistic transport in our G-BN devices the bend resistance measurements were performed. We have observed negative bend resistance on $n > 10^{11} cm^{-2}$ which confirmed ballistic transport over 1 μm at room temperature. The mean free path of charge carriers reaches ~ 3 μm at low temperature with large negative bend resistance value and this value implies very high charge carrier mobility ~ 500 000 $cm^2V^{-1}s^{-1}$.

6.2 Conductance

The operation of semiconductor devices at low temperature by applying electric field strongly depends upon the chemical potential μ, and impurities distribution present in the device [121]. This control over the device functioning becomes more complicated when the device scale becomes smaller. Quantum transport approach is needed to deal with and understand the transport of carriers in such a structure [122,123]. Quantum interference is observed when the inelastic scattering of charge carriers is weak and their phase coherence is maintained which can be seen in structures of small length scales.

In general, charge transport described by the electrical conductance, depends upon certain characteristic length scales in the system (mean free path, phase coherence length, elastic scattering length) and their relation with the size of the system [122]. Different transport regimes can occur depending on these relations. As the characteristic length of the system continue to decrease, the quantum phenomena become important such as universal conductance, fluctuations, weak localisation and ballistic transport (when the charge carriers in the system experience no scattering while travelling through the device) [31]. The electrical quantity such as conductivity σ and conductance G also become quantized. The Landauer Buttiker formula [124,125] relates the conductance of a multi-terminal device to the electron transmission coefficients. The conductance of a two terminal device according to Landauer formula is the product of e^2/h, the number of propagating transverse modes and the transmission coefficient T and given as:

$$G = \frac{2e^2}{h} MT \tag{6.1}$$

T is assumed independent of energy and lies between 0 to 1 and is defined as the transmission probability of the electron to pass from one contact to another.

For calculating the quantum conductance of a device, consider a wire with M number of occupied modes and T as the transmission per mode. Each state occupies $\frac{2\pi}{W}$ volume in k-space (between $-k_F\, to + k_F$) therefore the number of occupied modes is given by:

$$M = \frac{K_F W}{\pi} \tag{6.2}$$

where k_F the maximum wavevector in the degenerate electron gas and w is the width of the wire.

The conductance of a quantum device increases in steps as M increases in steps for such small devices. For transmission probability T≈1, the active region of the device should be short (few microns) so as to have small scattering of carriers.

In our experiment we measured the conductance of the graphene on a boron nitride substrate and compared the measured value with that of the calculated using Landaue Buttiker formula and numerical modelling of the transmission probability through our device. The active region of the GBN device was taken $w\sim$ 1 μm and length of 3 μm for calculation purposes. At high charge density n$>$ 10^{11}, the transmission probability calculated was T ~ 0.4 which represents the quasi ballistic region of carrier transport (regime between diffusive and ballistic system satisfying the condition $W < l_m and\, L > l_m,\ W$ being the width of the system) and situation of this regime of system is presented schematically in Fig. 6.1.

6.3 Ballistic Transport

One important length scale in the system is the mean free path of the carriers. Mean free path is the average distance that an electron travels before it scatters elastically. The mean free path l_m is related to the relaxation time and the average velocity of charge carriers as:

$$l_m = v\tau_m \tag{6.3}$$

Where τ_m is the momentum relaxation time and υ is the velocity of charge carriers.

If the dimension of the system is larger than the mean free path that is $L > l_m$ then the charge carriers in the system undergo both elastic and inelastic scattering. However the inelastic scattering in this regime is considered to be weak. In this device region, the drift-diffusion model is used to describe carrier transport [121,123]. The current density J for charge carriers (electrons and holes) becomes:

$$J_{e,p} = q_{e,p} n_{e,p} \mu_{e,p} E + q_{e,p} D_{e,p} \Delta n_{e,p} \quad (6.4)$$

The subscripts e and p represents the electrons and holes. $q, n\ and\ \Delta n$ are the charge, density and change in density of charge carriers. Whereas μ and D are the mobilities of charge carriers and diffusion coefficients respectively. The average velocity of carriers in this case is given by the drift velocity as a result of the applied electric field $v_d = -\mu E$. Along with the drift motion of carriers, the diffusive transport also contributes, which occurs as a result of the gradient in the carrier density.

When the system size is smaller than the elastic mean free path $L < l_m$, the charge carriers in the system can cross it without any scattering. Therefore in an ideal ballistic transport device, the charge carriers cross the active region without any collisions. In this case, the charge carrier momentum increases as a result of the acceleration by applied electric field. The situation of the diffusive, quasi ballistic and ballistic transport regime is illustrated in Fig. 6.1.

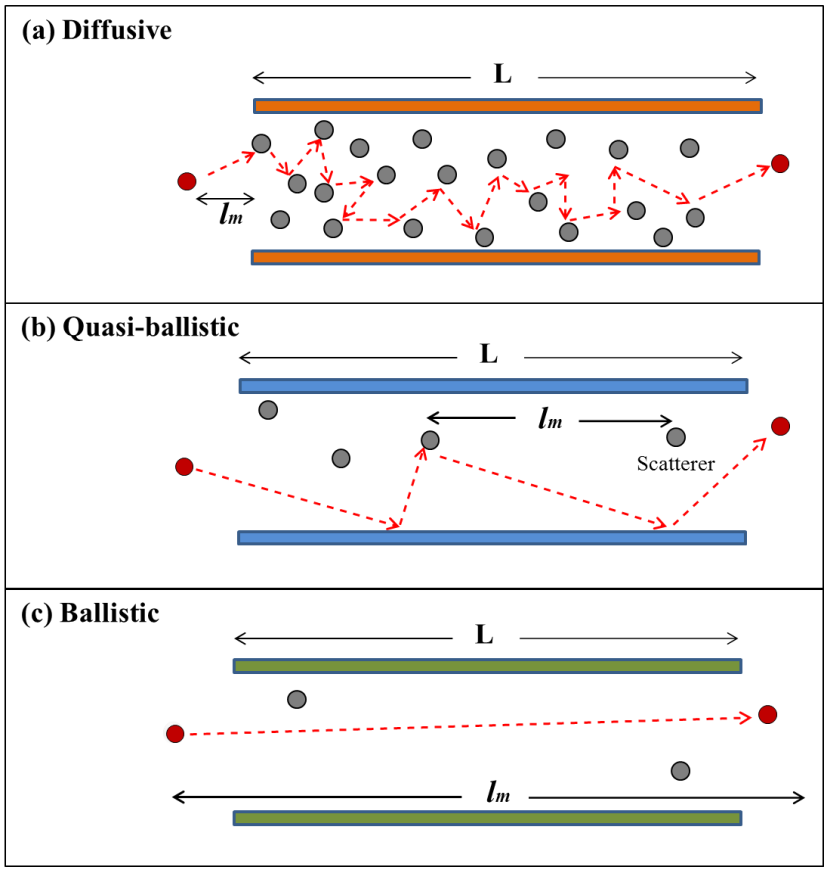

Figure 6.1: schematic of the Ballistic transport regime in the system

Ballistic transport has been studied in GaAs:AlGaAs heterostrutures where the mean free path of the charge carriers can reaches ~ 10μm [122,126].

We have studied the ballistic transport in our graphene boron nitride (GBN) heterostructure. Room temperature ballistic transport over 1μm has been observed for these devices using bend resistance measurements. At low temperature, for higher densities $n \approx 10^{12}\text{cm}^{-2}$, the bend resistance measurement reveals $l \approx 3\mu\text{m}$ for the measured GBN device. The graphene boron nitride encapsulated devices showed ballistic transport for a wide range of charge carrier concentration.

6.4 Bend Resistance

In graphene boron nitride devices, we studied the bend resistance R_B in order to investigate the behaviour of our sample in the ballistic limit.

Vander Pauw method [127] was used for calculating the resistance and resistivity of arbitrary geometry samples of semiconductor material. The resistance of the sample with four probe contact design as shown in Fig. 6.2, according to Vander Pauw method is given by:

$$R_B = R_{3421} = \frac{(\ln 2)}{\pi\sigma} \tag{6.5}$$

Where $R_{3421} = \frac{V_{34}}{I_{21}}$ and can be verified for different combinations in the device symmetry.

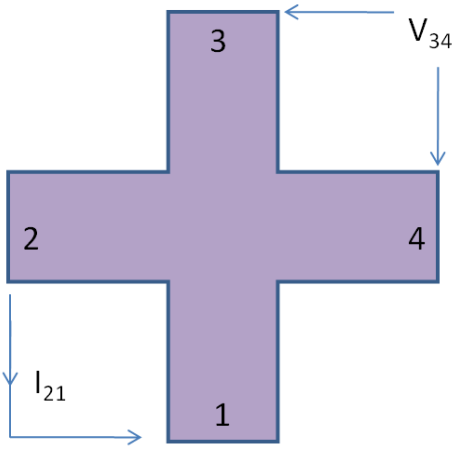

Figure 6.2: schematic of the four terminal geometry for measurement of bend resistance.

For a typical graphene sample the bend resistance can be calculated using Vander Pauw method [128] which uses the diffusive approximation and is given by eq. (6.5). In this case, current is provided between contacts 2 and 1 (I_{21}) and the corresponding voltage is measured between the contacts 3 and 4 (V_{34}). Different configurations in the sample should give the same value of the resistance measured. This formula fails for high mobility samples measured in our experiment as the charge carriers entering through the contact 2 reach directly to the contact 4 without being scattered. One can then assume that is ballistic transport condition is obtained and the measured bend resistance becomes negative. Bend resistance measurements were performed at temperature ranging from 2K to 250K.

In presence of a magnetic field, there is a change in the electron trajectories and chances for electrons to reach the correct contacts (like above contact 3 or 4 etc) increases. Therefore at high magnetic fields, a positive value of the bend resistance is recovered [31]. This forward transmission of electrons (ballistic transport) also affects the Hall voltage measured across the contacts of the device. The Hall resistance R_H is suppressed until the magnetic field is strong enough to guide the electrons to the right contacts and at this stage Hall resistance is recovered.

To check the influence of a magnetic field in high mobility devices, a magnetic field was applied perpendicular to graphene at constant gate voltage. The applied magnetic field made the trajectory of ballistic electrons curve and bend resistance R_B became positive as electrons could not reach the opposite contact ballistically. The magnetic field at which R_B changed its sign was ~0.1 T. The anomalous behaviour of Hall resistivity R_H was also observed with a prominent kink at 0.1 T which disappeared close to room temperature indicating the retrieval (restoring) of a diffusive regime from the ballistic regime. The negative bend resistance R_B, its magnetic field behaviour and anomalies in R_H discussed above all indicate the ballistic transport in our graphene boron nitride heterostructure.

For ballistic devices, boundary scattering of charge carriers is an important aspect of functioning of the device. As it is not possible to make a device with completely smooth edges, diffusive boundary scattering becomes more prominent rather than the specular scattering. In the limit of diffuse boundary scattering the mean free path of electrons is limited by width of the device thus limiting the ballistic transport [31]. The effective mean free path can be taken as the sum of the diffusive and bulk scattering in the device as:

$$\frac{1}{l_{eff}} = \frac{1}{l_0} + \frac{1}{l_b} \tag{6.6}$$

Where l_0 is the mean free path of a device with no boundaries (case of bulk scattering) and l_b is boundary scattering length taken as average distance a carrier travels before diffusive scattering at the boundary. The boundary scattering length $l_b \sim \frac{w}{1-p}$

where p is the number used to describe the scattering from the rough edge and varies between the values 0 to 1 and w is the width of the device. These lengths affect the resistivity of the device which can be given as:

$$\rho_{eff} = \rho_0 l_0 \left(\frac{1}{l_0} + \frac{1-p}{w}\right) \tag{6.7}$$

where ρ_0 is the resistivity of a large(what is large) device. From eq. (6.7) it is clear that the diffuse boundary scattering will dominate the resistance if $l_b \sim \frac{w}{1-p} < l_0$.

In our experiment we also calculated R_B theoretically by assuming that the boundary scattering is diffusive. By considering specular boundary scattering, the value of R_B could not reach such large negative values measured experimentally. The diffusive boundary scattering decreases the conductivity in ballistic devices but makes R_B more negative as a result of collimation effects. This effect was observed in the asymmetry of the conductivity and bend resistance curve for holes and electrons in our measurements. By using diffusive boundary scattering assumption, the measured value of R_B yields mean free path $l \approx 1.5\,\mu m$ near room temperature and $l \approx 3$µm below 50 K. Such negative values of R_B for charge carrier density $n \approx 4 \times 10^{11} \text{cm}^{-2}$ at mean free path $l \approx 3\mu m$ exhibit graphene mobility μ ~ 500 000 $\text{cm}^2\text{V}^{-1}\text{s}^{-1}$.

6.5 Device fabrication

Hexagonal boron nitride (hBN) is an alternate substrate to oxidised silicon as discussed in chapter 4, section 4.6. For this purpose hBN flakes are prepared on oxidised silicon surface by the micromechanical exfoliation technique fig.(6.4 a). Using an optical microscope, a flake of thickness ~30nm is selected for the substrate. Afterwards a graphene flake is made using mechanical cleavage on another PMGI-PMMA coated Silicon substrate (6.4 b) and transferred on top of hBN (substrate) by "dry flake transfer" technique (see chapter 5, section 5.4). The optical image of G-BN structure is in Fig 6.4(c). Figure 6.3 shows a schematic diagram of graphene-hBN (G-hBN) structure fabricated by this method.

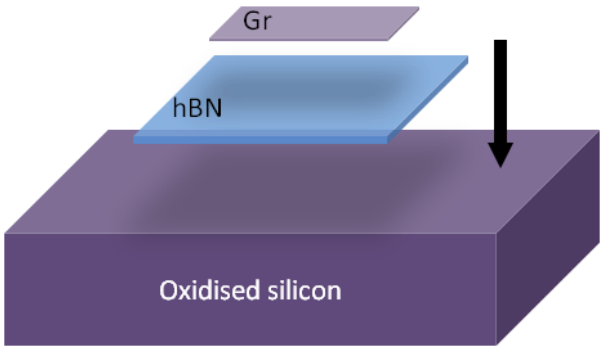

Figure 6.3: Schematic diagram of Graphene-hBN device assembly prepared on oxidized silicon substrate.Graphene layer transferred on the mechanically cleaved h-BN surface.

Figure 6.4: Sample fabrication for GBN hetero-structures. (a) light blue hBN flakes are ~ 30 nm thick (b) Graphene mechanically cleaved on PMGI-PMMA pre coated on Si/SiO_2 (c)Graphene flakes transferred on hBN flake.

Before proceeding towards device patterning, the sample is annealed in Ar-H_2 atmosphere at $300C^0$ in order to remove the organic contaminants. E-beam lithography is used to make

a standard Hall bar geometry for transport measurement. Figure 6.5 shows step by step process of device fabrication.

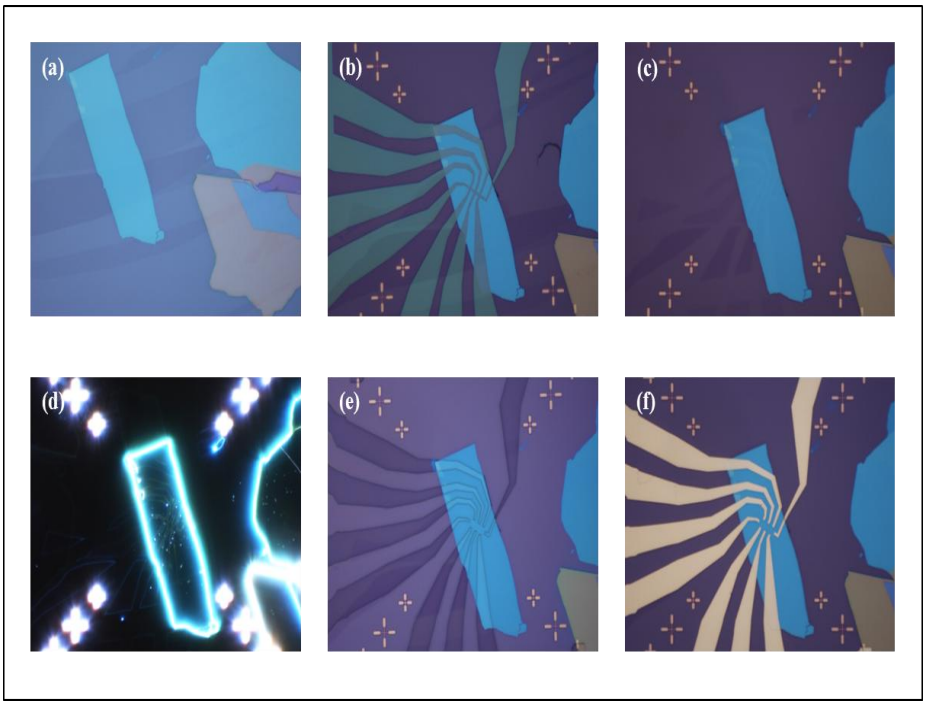

Figure 6.5: steps involved during the graphene device making on hBN substrate. (a) Bilayer PMMA resist spinning. (b) Etching mesa before the exposure for contacts layer. (c) Exposing to Ar-O_2 plasma for 2 min and washing the resist (d) Dark field image of graphene Hall bar etched on hBN substrate. (e) Spinning of bilayer PMMA resist and exposure for contacts and development. (f) Metal evaporation and lift-off.

The transport measurements of a graphene sample on hBN substrate show a significant improvement of the charge career's mobility in comparison with the devices on oxidised silicon substrate. For the device shown in Fig. 6.5, graphene mobility is ~ 50 000 cm^2v^{-1} S^{-1}. Another graphene device on oxidised silicon surface shows carrier mobility of ~8 000 cm^2v^{-1} S^{-1}. Figure 6.6 gives a comparison of graphene mobility on Si/SiO_2 substrate and on hexagonal boron nitride (hBN) substrate.

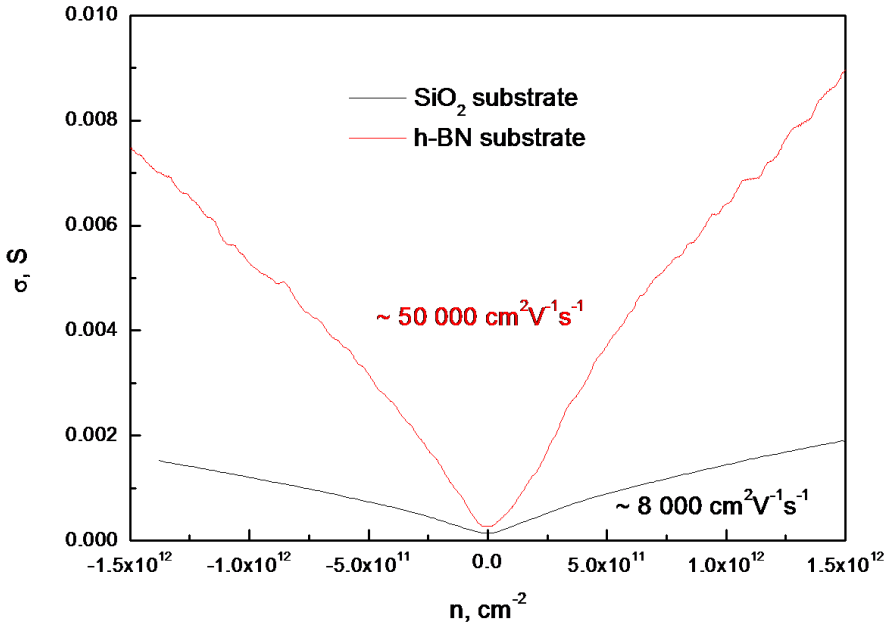

Figure 6.6: Conductivity as a function of carrier density for graphene device on Si/SiO_2 substrate (grey curve) and hBN substrate(red). The measured graphene mobility on hBN substrate is higher as compared to Si/SiO_2 substrate.

Improvements in graphene mobility was seen after annealing of the GBN device in Ar-H_2 atmosphere and mobilities up to 100 000 cm^2v^{-1} S^{-1} were measured in successive GBN devices. To isolate the device from the external contaminations that may reduce the mobility, the GBN heterostructure was encapsulated with another thick hBN flake (usually a thick hBN flake approximately 20-30 nm is used for this purpose). The schematic diagram of the encapsulated structure is presented in Fig. 6.7.

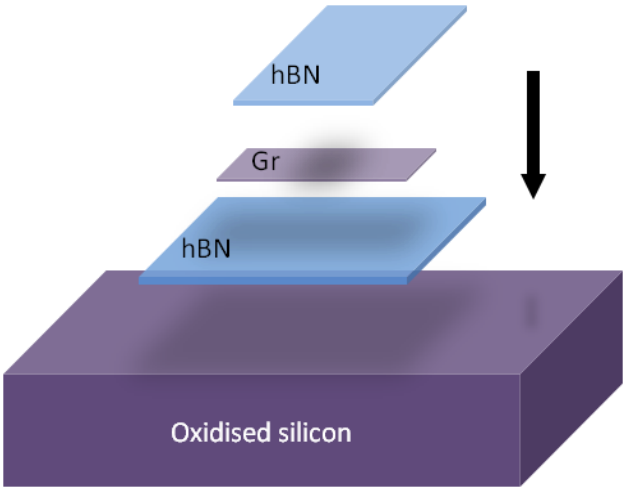

Figure 6.7: Schematic diagram of encapsulated Graphene-hBN device assembly. Thick hBN~ 20-30 nm (light blue optical contrast on 300nm SiO_2) is used for encapsulation.

A graphene device made on hBN substrate which was subsequently encapsulated with another hBN flake is shown in Fig. 6.8.

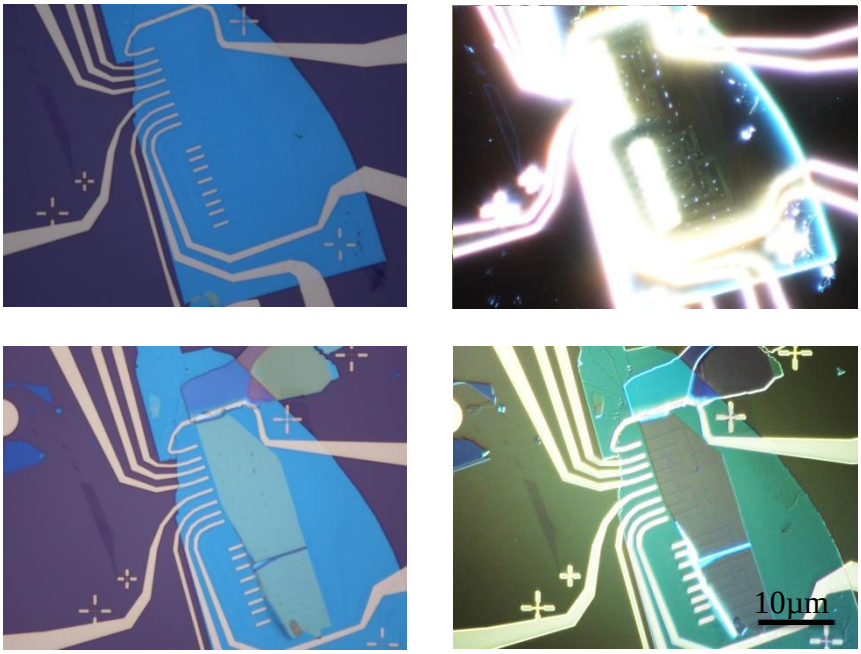

Figure 6.8: (a) optical image of a graphene device made on hBN substarte (before encapsulating). (b) Dark filed image of the GBN device. (c) optical image of GBN device after encapsulating with another hBN flake. (d) differential interference contrast image of encapsulated GBN device.

6.7 Results and Discussion

The results of this work have been published in ***Nano Letters*** in 2011. In order to best present our results, the original paper "**Micrometer-Scale Ballistic Transport in Encapsulated Graphene at Room Temperature"** (Nano Lett. 11(2011), P 2396-2399) is attached from the next page.

This work presented was carried out in collaboration with several colleagues of the University of Manchester. My contribution to this work includes the preparation of hexagonal boron nitride (hBN) and graphene flakes on oxidised silicon substrate by mechanical cleavage, precise graphene transfer on top of hBN for making graphene boron nitride heterostructures using the transfer techniques discussed in chapter 5 of this thesis, device fabrication of graphene boron nitride heterostructure and finally device encapsulation using boron nitride.

Micrometer-Scale Ballistic Transport in Encapsulated Graphene at Room Temperature

Alexander S. Mayorov, Roman V. Gorbachev, Sergey V. Morozov, Liam Britnell, **Rashid Jalil**, Leonid A. Ponomarenko, Peter Blake, Kostya S. Novoselov, Kenji Watanabe, Takashi Taniguchi, and A. K. Geim

Nano Lett., 2011, 11 (6), pp 2396–2399

Abstract

Devices made from graphene encapsulated in hexagonal boron-nitride exhibit pronounced negative bend resistance and an anomalous Hall effect, which are a direct consequence of room-temperature ballistic transport at a micrometer scale for a wide range of carrier concentrations. The encapsulation makes graphene practically insusceptible to the ambient atmosphere and, simultaneously, allows the use of boron nitride as an ultrathin top gate dielectric.

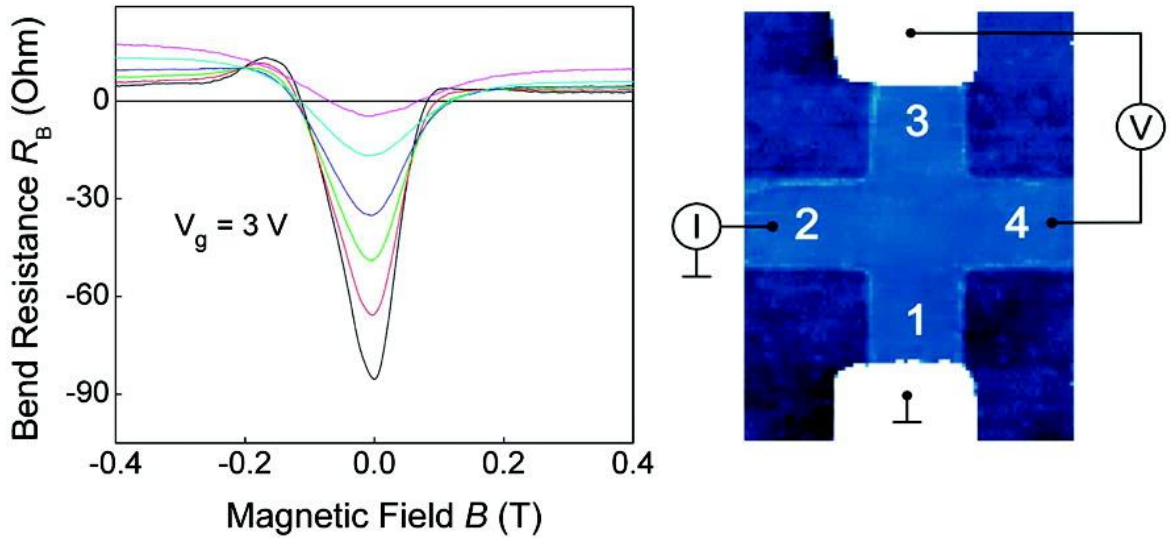

Keywords:

Boron nitride; encapsulated graphene; ballistic transport; negative bend resistance; top gate.

In search for new phenomena and applications, which are expected, predicted or to be uncovered in graphene, it is important to continue improving its electronic quality that is commonly characterized by charge carrier mobility μ. Graphene obtained by mechanical cleavage on top of an oxidized Si wafer usually exhibits μ ~10 000 $cm^2 V^{-1} s^{-1}$ (1). For typical carrier concentrations $n \approx 10^{12}$ cm^{-2}, such quality translates into the mean free path $l = (h/2e)\mu(n/\pi)^{0.5}$ of the order of 100 nm where h is Planck's constant and e is the electron charge. On the other hand, it has been shown that if extrinsic scattering in graphene is eliminated its mobility at room temperature (T) can reach ~200 000 $cm^2 V^{-1} s^{-1}$ due to weak electron–phonon interaction (2). Indeed, for $n \sim 10^{11}$ cm^{-2} μ exceeding 100 000 $cm^2 V^{-1} s^{-1}$ and 1 000 000 $cm^2 V^{-1} s^{-1}$ at room and liquid-helium T, respectively, were demonstrated for suspended graphene annealed by high electric current (3-5). However, suspended devices are extremely fragile, susceptible to the ambient atmosphere, and difficult to anneal in the proper four-probe geometry (the latter was not achieved so far). Furthermore, it requires a significant amount of strain to suppress flexural modes in suspended graphene and retain high μ up to room T (5). Most recently, a breakthrough was achieved by using hexagonal boron-nitride (hBN) as an atomically smooth and inert substrate for cleaved graphene (6) Such structures were shown to exhibit μ ~100 000 $cm^2 V^{-1} s^{-1}$ at n ~10^{11} cm^{-2}. Although μ achieved in graphene yield l approaching 1 μm, no ballistic effects on this scale have so far been reported.

In this Letter, we describe devices made from graphene sandwiched between two hBN crystals. The devices exhibit room-T ballistic transport well over a 1 μm distance, as evidenced directly from the negative transfer resistance measured in the bend geometry (7) At low $n \sim 10^{11}$ cm^{-2}, the devices exhibit mobility μ > 100 000 $cm^2 V^{-1} s^{-1}$ even at room T, as determined from their response to gate voltage (1-6). At higher $n \approx 10^{12}$ cm^{-2}, we find that our devices' longitudinal conductivity σ becomes limited by their width $w \approx 1$ μm rather than scattering in the bulk. To extract intrinsic μ and l in this ballistic regime, we employed measurements of bend resistance R_B that, unlike σ, continues being sensitive to l. Our analysis yields $l \approx 3$ μm for $n \approx 10^{12}$ $cm^{-2}$and at low T, which translates into μ ~ 500 000 $cm^2 V^{-1} s^{-1}$. In addition, the encapsulation has made graphene insusceptible to the environment so that long and repeated exposure to the ambient air was found to have little effect on remnant doping and μ.

The studied samples that we further refer to as graphene-boron-nitride (GBN) heterostructures were fabricated by using the following multistep technology. First, relatively thick (~10 nm) hBN crystals were mechanically deposited on top of an oxidized Si wafer (100 nm of SiO_2). Then, submillimeter graphene crystallites were produced by cleavage on another substrate precoated with a double layer polymer stack. The bottom polymer "release" layer was then dissolved from the sides and the resulting film with the graphene flake was transferred on top of the chosen hBN crystal. Similarly to ref 8, we have found that to achieve high mobility it was important not to expose the graphene surface (that goes into contact with hBN) to any solvent (dry transfer technique). Electron-beam lithography and oxygen plasma etching were then employed to define graphene Hall bars (see images in Figures 1 and 2). The deposition of graphene on hBN resulted in numerous "bubbles" containing trapped adsorbates (presumably hydrocarbons), and if present in the active part of our devices such bubbles caused significant charge inhomogeneity. This limited the achievable w to ~1 μm, as we tried to fit the central wire inside areas free from the bubbles. The second hBN crystal (~10 nm thick) was again transferred by using the same dry procedure. The top crystal was carefully aligned to encapsulate the graphene Hall bar but leave the contact regions open for depositing metal (Au/Ti) contacts. In some devices, the top hBN crystal was used as a dielectric for local gating. After each transfer step, the devices were annealed at 300 °C in an argon–hydrogen atmosphere to remove polymer residues and other contamination.

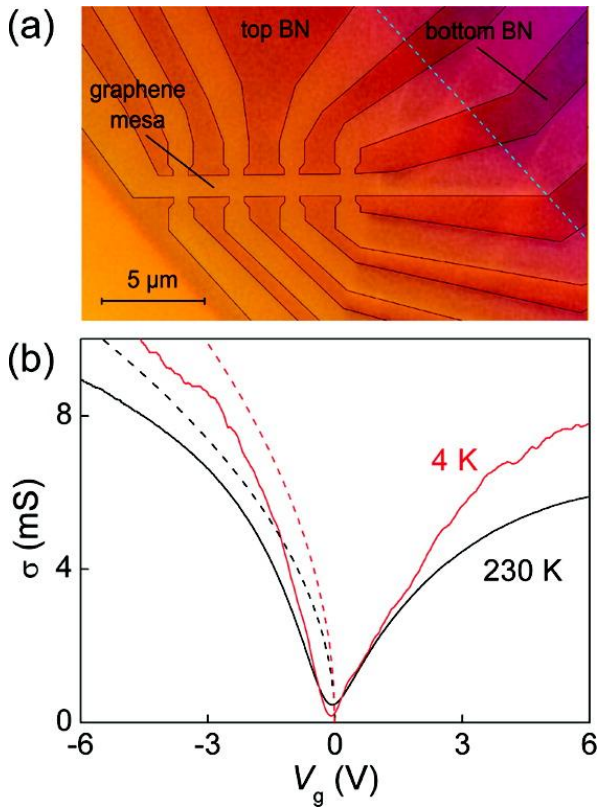

Figure 1 (a) Optical micrograph of one of our GBN devices. The plasma etching resulted in a few nanometers tall mesa that could be visualized by using the differential interference contrast. To improve the mesa's visibility, its contour is shown by the thin gray lines. The slanted dashed line indicates the edge of the top hBN crystal. (b) σ(*V*g) measured at two *T* (solid curves). The dashed curves are σ calculated by using the Landauer–Buttiker formula and numerical modeling of the transmission probability through a quantum wire with $w = 1$ μm. In the calculations, we assume diffusive boundary scattering and the intrinsic mean free path in the graphene bulk *l*i = 1.5 and 3 μm at 230 and 4 K, respectively, which are the values inferred from measurements of *R*B as described below. Note that the standard analysis for the extraction of the field-effect μ from σ(*n*) is valid only for the diffusive regime and fails at higher *n* where $l > w$.

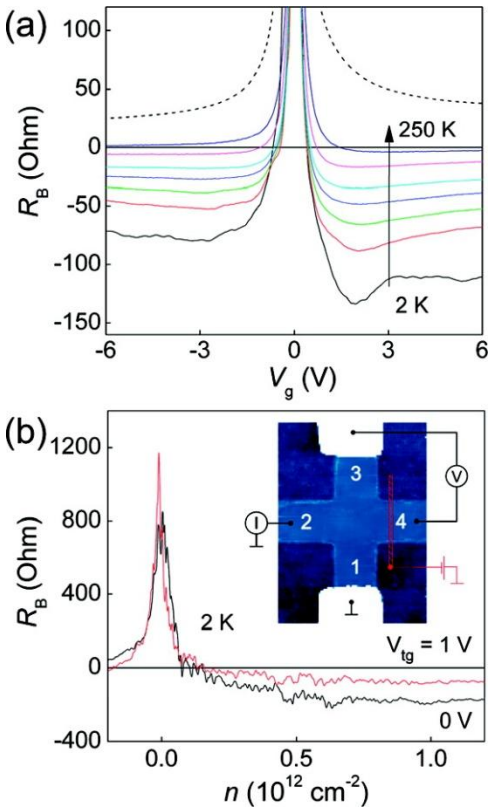

Figure 2. (a) Bend resistance at various T for the same device as in Figure 1b. The curves from bottom to top correspond to 2, 50, 80, 110, 140, 200, and 250 K, respectively. The dashed curve is RB calculated using σ(Vg) and the van der Pauw formula. (b) Inset: atomic force micrograph of one of our Hall crosses. The scale is given by the device width $w \approx 1$ μm. The drawings schematically depict the bend measurement geometry and a narrow top gate (in red) deposited across one of the leads at a later microfabrication stage. Main panel: RB(n) for a device with the such a top gate. The negative RB can be suppressed by applying top-gate voltage Vtg which creates an extra barrier and reflects electrons.

Figure 1b shows σ as a function of back-gate voltage V_g for a GBN device, measured in the standard four-probe geometry. The minimum in σ occurs at $V_g \approx -0.1$ V, indicating little extrinsic doping (~10^{10} cm^{-2}). At small hole concentrations $n \sim 10^{11}$ cm^{-2}, the slopes of σ(V_g) yield μ ≈ 140 000 and 100 000 cm^2 V^{-1} s^{-1} at 4 K and near room T, respectively (low-n μ is about 30% lower for electrons). The values are in agreement with the measured Hall mobility. In general, at low n our GBN devices exhibited μ between 20 000 and 150 000 cm^2 V^{-1} s^{-1}, tending to ≈100 000 cm^2 V^{-1} s^{-1} in most cases. This translates into a submicrometer mean free path, that is, less than our devices' width (w = 1 μm), which justifies the use of the diffusive transport formulas at low n.

A notable feature of Figure 1b is a relatively weak T dependence of $\sigma(V_g)$ away from the neutrality point, which is surprising because electron–phonon scattering is expected to start playing a significant role in graphene of such quality (2, 5, 9). Also, the strong sublinear behavior of $\sigma(V_g)$ is unusual for graphene measured in the four probe geometry. As shown below, these features are related to electron transport limited at high n by boundary scattering so that $\sigma = 2e^2/h(k_F l) \propto n^{1/2} \propto V_g^{1/2}$, where $l \sim w$ and, therefore, σ weakly depends on T. In the limit $l \geq w$, we cannot use the standard formulas to extract μ and l and a special care should be taken to interpret the $\sigma(n)$ behavior. The importance of boundary scattering in our devices can be immediately appreciated if we estimate transmission probability Tr through our 3 μm long device in Figure 1. To this end, the standard Landauer–Buttiker formula for quantum conductance $G = (4e^2/\pi h)(k_F w)\mathrm{Tr}$ yields at high n, Tr ≈ 0.4, which indicates quasi-ballistic transport (here, $k_F w/\pi$ is the number of propagating Dirac fermions modes).

To gain further information about electronic quality of the GBN bulk in the ballistic limit, we have studied bend resistance R_B (10). To this end, we applied current I_{21} between contacts 2 and 1 and measured voltage V_{34} between probes 3 and 4 (see Figure 2), which yielded $R_B = R_{34,21} = V_{34}/I_{21}$. Different bend configurations (e.g., $R_{14,23}$ and $R_{32,14}$) yielded similar $R_B(V_g)$. For a diffusive conductor, R_B should be equal to $(\ln 2)/\pi\sigma$ (11). The van der Pauw formula uses the diffusive approximation and can accurately describe $R_B(V_g)$ in the standard-quality graphene (10). However, the formalism completely fails in our high-μ devices. Indeed, R_B becomes negative, which shows that most of the charge carriers injected from, for example, contact 2 can reach contact 4 without being scattered. The counterintuitive negative resistance was observed in high-μ two-dimensional gases based on GaAlAs heterostructures and required $l_i \gg w$ where l_i is the mean free path in the bulk (7) Such ballistic propagation of charge carriers has not been reported in graphene before except for ref 12 where low-T nonlinear I–V characteristics were measured in 50 nm Hall crosses at a fixed n and interpreted in terms of ballistic transport.

In contrast to the measurements in the standard geometry as in Figure 1b, R_B in Figure 2a exhibits very strong T dependence, which is in agreement with the expectations for high-μ graphene (5, 9). Despite this extra phonon scattering, R_B remains negative at high n for all $T \leq 250$ K (our highest T in the experimental setup) and does not even approach the gate dependence expected in the diffusive regime (dashed curve in Figure 2a). This observation yields $l_i > w \approx 1$ μm even at room T, which is the condition essential for the observation of negative R_B (7, 13). The strong T dependence of R_B also signifies

that l_i grows substantially with decreasing T. Complementary evidence for ballistic transfer through the Hall cross comes from devices with an extra barrier placed across one of the potential leads (Figure 2b). When a voltage was applied to the narrow top gate, the potential barrier reflected some carriers back into the cross and, accordingly, suppressed negative R_B. Also, note that, in the low-n regime ($|V_g| < 0.5$ V) where we could determine μ from the linear dependence $\sigma \propto V_g$ as ~140 000 $cm^2V^{-1}s^{-1}$, R_B remains positive, as expected, because the corresponding $l = (h/2e)\mu(n/\pi)^{0.5} \leq 0.5$ μm is insufficient for causing the ballistic conditions and negative R_B.

To elucidate the micrometer-scale ballistic transport in our GBN heterostructures, Figure 3a shows R_B as a function of magnetic field B applied perpendicular to graphene at a fixed V_g (+3 V in this case). As expected,(7)R_B changes its sign with increasing B because injected electrons are bended by B and can no longer reach the opposite contact ballistically. This behavior is in agreement with the one reported in GaAlAs heterostructures (7, 14). The characteristic field B_0at which R_B changes sign in Figure 3a is ~0.1 T, which corresponds to a cyclotron orbit of radius$r_c = \hbar(\pi n)^{1/2}/eB \approx 1$ μm, that is equal to w, which is in agreement with theory (7, 14) ($n \approx 6 \times 10^{11}$ cm^{-2} in this case). Furthermore, ballistic transport is expected to cause an anomalous behavior of Hall resistivity R_H such that it is no longer a linear function of B. Figure 3b shows that, indeed, our devices exhibit nonlinear $R_H(B)$ with a notable kink at the same characteristicB_0. This anomaly is usually referred to as the last plateau and absent in diffusive systems (7). The kink almost disappears near room T (Figure 3b) indicating that we get closer to the diffusive regime. The functional form of $R_H(B)$ strongly depends on the exact shape of Hall crosses, and the anomaly becomes minor if a cross has sharp corners,(7, 14) as is the case of our devices (see image in Figure 2b).

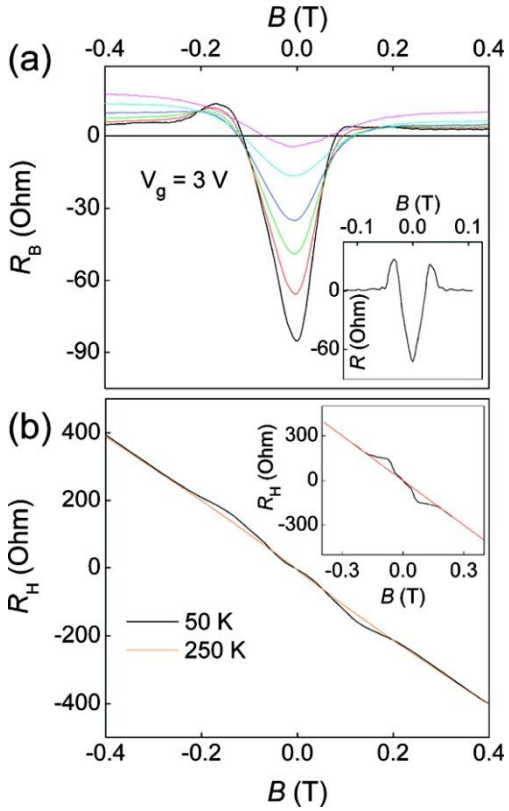

Figure 3. Ballistic transport in magnetic field. (a) *R*B(*B*) for a fixed $n \approx 6 \times 1011$ cm–2. *T* is 50, 80, 110, 140, 200, and 250 K (from bottom to top curves, respectively). Inset: *R*B(*B*) calculated for a Hall cross using the billiard-ball model(7) and scaled for the case of our graphene devices and the above *n*. (b) Hall resistance *R*H measured at 50 and 250 K. Inset: *R*H(*B*) found theoretically for rounded corners(7) and scaled for our case. The red line in the inset indicates the diffusive limit.

The negative R_B, its magnetic field behavior, anomalies in R_H, and the influence of the top gate unambiguously prove that in our Hall crosses charge carriers can reach the opposite lead ballistically without scattering. This yields *l* longer than 1 μm for all $|V_g| > 1$ V where the large negative R_B is observed ($|n| \geq 2 \times 10^{11}$ cm^{-2}). To appreciate such large values of *l*, let us mention that in suspended devices (3, 4) and graphene on BN (6) ultrahigh μ were reported only at low $n \sim 10^{11}$ cm^{-2}, which translates into submicrometer *l*, (3, 4) and $l \approx 1$ μm were achieved only in suspended devices with a million μ at low *T* (5).

For $l_i > w$, the boundary scattering makes σ only weakly dependent on the bulk quality of graphene, and to obtain a better estimate for l_i than just ≥1 μm as above we used numerical simulations. We calculated R_B by using the billiard-ball mode l(7) and assuming diffusive boundary scattering. If the scattering is assumed specular, calculated R_B cannot reach the large negative values observed experimentally. This agrees with general expectations that etched graphene edges are usually rough and scatter diffusively. Diffusive boundary

scattering decreases σ of a ballistic wire (transmission probability decreases) but makes R_B more negative due to collimation effects (15) This is consistent with our experiment that shows higher (more ballistic) σ for holes but more negative R_B for electrons and vice versa (cf. Figures 1 and 2). This asymmetry can be attributed to a larger degree of diffusivity in boundary scattering for electrons, which implies an extra charge that breaks the electron–hole symmetry of the boundary. Under the assumption of diffusive scattering, the measured R_B yield $l_i \approx 1.5$ μm near room T and ≈3 μm below 50 K for $|n| > 2 \times 10^{11}$ cm^{-2} ($|V_g| > 1$ V). Although the exact values are inferred by and assuming diffusive boundaries, such large l_i (of the order of a couple of micrometers) are essential to explain qualitatively both large negative R_B and its strong T dependence (for example, $l_i \leq$ 1 μm would be inconsistent with these observations). The inferred l_i also allow us to understand the behavior of σ and its weak T dependence, and the dashed curves in Figure 1b show $\sigma(V_g)$ calculated within the same model and parameters. Better agreement with the experiment could be achieved by modeling local doping profiles near edges but this goes beyond the accuracy of our simple billiard-ball model.

Finally, we note that for $n \approx 4 \times 10^{11}$ cm^{-2} where R_B reaches its most negative value $l_i \approx 3$ μm implies intrinsic μ ~ 500 000 cm^2 V^{-1} s^{-1}. It is an extremely high value for graphene but without it we would not be able to observe large negative R_B. Note that this is also consistent with μ ~150 000 cm^2 V^{-1} s^{-1} found from the standard field effect analysis at lower $n \approx 1 \times 10^{11}$ cm^{-2} where charge inhomogeneity remains significant. The latter regime corresponds to $l_i \leq 0.5$ μm and does not allow negative R_B at low n, which is in agreement in the experimental observations. To confirm the ultrahigh μ at high n by using the analysis of $\sigma(n)$, which has become conventional for graphene, would require GBN devices with $w > 5$ μm (diffusive regime). So far, we have been unable to achieve this because of the mentioned bubbles that result in charge inhomogeneity.

In conclusion, graphene encapsulated in hBN exhibits robust ballistic transport with a large negative transfer resistance and the mean free path exceeding ~3 μm at low T. Away from the neutrality point, (for carrier concentrations above 10^{11} cm^{-2}) the longitudinal conductivity of our 1 μm wide devices becomes limited by diffusive scattering at the sample boundaries rather than in the graphene bulk. The demonstrated graphene-boron-nitride heterostructures is a further improvement with respect to the devices reported previously, in terms of their environmental stability and the possibility of using the encapsulating hBN as a quality top dielectric. Our work also shows that it should be possible to achieve million mobilities for graphene on boron nitride.

Acknowledgment

This work was supported by the Körber Foundation, Engineering and Physical Sciences Research Council (U.K.), the Office of Naval Research, the Air Force Office of Scientific Research, and the Royal Society.

References

This article references 15 other publications.

1. Geim, A. K.; Novoselov, K. S.The rise of graphene *Nat. Mater.* **2007**, 6, 183– 191

2. Morozov, S. V.; Novoselov, K. S.; Katsnelson, M. I.; Schedin, F.; Elias, D. C.; Jaszczak, J. A.; Geim, A. K.Giant intrinsic carrier mobilities in graphene and its bilayer *Phys. Rev. Lett.***2008**, 100, 016602

3. Du, X.; Skachko, I.; Barker, A.; Andrei, E. Y.Approaching ballistic transport in suspended graphene *Nat. Nanotechnol.* **2008**, 3, 491– 495
4. Bolotin, K. I.; Sikes, K. J.; Hone, J.; Stormer, H. L.; Kim, P.Temperature-dependent transport in suspended graphene *Phys. Rev. Lett.* **2008**, 101, 096802
5. Castro, E. V.; Ochoa, H.; Katsnelson, M. I.; Gorbachev, R. V.; Elias, D. C.; Novoselov, K. S.; Geim, A. K.; Guinea, F.Limits on charge carrier mobility in suspended graphene due to flexural phonons *Phys. Rev. Lett.* **2010**, 105, 266601
6. Dean, C. R.; Young, A. F.; Meric, I.; Lee, C.; Wang, L.; Sorgenfrei, S.; Watanabe, K.; Taniguchi, T.; Kim, P.; Shepard, K. L.; Hone, J.Boron nitride substrates for high-quality graphene electronics *Nat. Nanotechnol.* **2010**, 5, 722– 726
7. Beenakker, C. W. J.; van Houten, H.Billiard model of a ballistic multiprobe conductor *Phys. Rev. Lett.* **1989**, 63, 1857– 1860
8. Dean, C. R.; Young, A. F.; Cadden-Zimansky, P.; Wang, L.; Ren, H.; Watanabe, K.; Taniguchi, T.; Kim, P.; Hone, J.; Shepard, K. L.Multicomponent fractional quantum Hall effect in graphene. arXiv:1010.1179, **2010**.
9. Hwang, E. H.; Das Sarma, S.Acoustic phonon scattering limited carrier mobility in two-dimensional extrinsic graphene *Phys. Rev. B* **2008**, 77, 115449
10. Blake, P.; Yang, R.; Morozov, S. V.; Schedin, F.; Ponomarenko, L. A.; Zhukov, A. A.; Grigorieva, I. V.; Novoselov, K. S.; Geim, A. K.Influence of metal contacts

and charge inhomogeneity on transport properties of graphene near the neutrality point *Solid State Commun.* **2009**, 149, 1068– 1071

11. van der Pauw, L. J.A method of measuring the resistivity and Hall coefficient on lamellae of arbitrary shape *Philips Tech. Rev.* **1958**, 20, 220– 224
12. Weingart, S.; Bock, C.; Kunze, U.; Speck, F.; Seyller, Th.; Ley, L.Low-temperature ballistic transport in nanoscale epitaxial graphene cross junctions *Appl. Phys. Lett.* **2009**, 95,262101
13. Gilbertson, A. M.; Fearn, M.; Kormányos, A.; Read, D. E.; Emeny, M. T.; Lambert, C. J.; Ashley, T.; Solin, S. A.; Cohen, L. F.Ballistic transport and boundary scattering in InSb/InxAl1-xSb mesoscopic devices *Phys. Rev. B* **2011**, 83, 075304
14. Timp, G.; Baranger, H. U.; de Vegvar, P.; Cunningham, J. E.; Howard, R. E.; Behringer, R.; Mankiewich, P. M.Propagation around a bend in a multichannel electron waveguide *Phys. Rev. Lett.* **1988**, 60, 2081– 2084
15. Blaikie, R. J.; Nakazato, J. R. A.; Cleaver, H.Ahmed. Enhancement of resistance anomalies by diffuse boundary scattering in multiprobe ballistic conductors *Phys. Rev. B* **1992**, 46,9796– 9799

6.7 Conclusions

Graphene sandwiched between hBN crystals exhibits room temperature ballistic transport. At room temperature mobility of graphene boron nitride devices reaches 100,000 $cm^2V^{-1}s^1$ for low charge density ~ 10^{11} cm^{-2}. The negative transfer resistance measured in devices gives mean free path over 1μm at room temperature and 3μm at low T. The diffusive scattering at the boundary of device restricts the longitudinal conductivity at high charge carrier density ~ 10^{12} cm^{-2}. The reported graphene devices on BN substrate are improved structures in terms of an additional BN layer used for encapsulation that not only protects from environmental effects but can also serve as a top dielectric. Therefore now it is possible to achieve ultrahigh mobilities of graphene on BN substrate.

Chapter 7

Summary and Outlook

This thesis presents the studies of two dimensional novel material graphene on two different substrates: oxidized silicon (Si/SiO_2) and hexagonal boron nitride (hBN or simply BN). Graphene devices were made on oxidized silicon using standard lithography techniques and their electrical transport measurements were performed. A study for the hunt of a better substrate than oxidized silicon for graphene was made using hexagonal boron nitride. Mechanically cleaved hBN layers were characterized by optical microscopy and Raman spectroscopy. A technique was established for an accurate transfer of graphene flakes using wet and dry transfer method. Graphene boron nitride (GBN) heterostrutures were made using a precise transfer method, and transport studies revealed high charge carrier mobility ~ 100,000 $cm^2V^{-1}S^{-1}$ at room temperature. Evidence of ballistic transport has been observed for these devices.

Since the discovery of graphene its electronic properties [96] has attracted much attention. For electrical measurements and studies, graphene devices are commonly made on standard Si/SiO_2 substrates [1,13,66,67]. The work described in this thesis includes the fabrication of graphene device on SiO_2 using laser writer and relevant electrical measurements of device.

Attempts were made to improve the electronic quality that is usually measured in terms of electrical mobility, for graphene devices made on SiO_2 substrate [20,21,101,129].

However, the intrinsic mobility of graphene [20,21,130] has not been achieved for substrate based graphene although suspended graphene devices have reached extremely high mobilities [15]. Using hexagonal boron nitride as a substrate for graphene has improved the mobilities an order of magnitude higher than on SiO_2 [24]. The isolation and characterization of BN layers is very important task for its proper utilization in graphene based devices. The use of BN as a substrate or a spacer (thin insulator) has been suggested [24] which require precise identification and thickness measurements of these layers. In the work presented here, BN flakes were successfully prepared on Si/SiO_2 surface by mechanical cleavage. The size of the BN flakes varied from (50-100μm). These layers were identified by optical microscopy using various filters due to the low optical

contrast of thin layers. Different oxide thickness of SiO_2 substrate were taken to mechanically exfoliate BN flakes and their percentage contrast analysis shows that oxide thicknesses of about 80±10 nm provide maximum optical contrast for BN layers. Atomic force microscopy was used to measure the thickness of the BN layers. Raman studies were also performed to characterize different layers on the basis of their Raman signature. The analysis shows that BN Raman characteristic peak ≈ 1366 cm^{-1} becomes weaker as the number of BN layers decreases. The position of the BN peak shifts for different layers as the monolayer tends to shifts at higher and bilayer along with other thick layers shift toward the lower frequencies with respect to the bulk BN peak position. Thus Raman spectroscopy has proven to be a useful tool for identification of the number of BN layers. It is possible to fabricate and identify monolayer BN, another two dimensional material and multilayers of large sizes can be used for different purposes in graphene based devices for fundamental studies and applications. A few possible uses of atomically flat BN layers are as a substrate for graphene [24], ultrathin top dielectric to gate graphene [30] and as a thin insulator for GBN heterostructures [25].

The remarkable properties of first member of the two dimensional material family, graphene, has been extensively studied by depositing it on oxidized silicon surface. In order to improve the electronic quality of graphene thereby enabling the study new phenomena in the system and exploring its technological applications in various fields, it is necessary to fabricate graphene devices on substrates other than SiO_2 [29,54–56]. The influence of substrate on the properties of graphene has been studied [20,107]and suggested that the high mobilities can only be obtained by minimizing substrate effects through suspended or atomically flat substrates. Due to ease of making graphene (mechanical cleavge) on SiO_2 and certain technical reasons, it was first made on SiO_2 and then transferred to other substrates at a desired location. In the next part of the thesis, a useful technique for the transfer of graphene flakes has been described. Graphene flakes were transferred from SiO_2 surface to another surface (BN, mica or TEM grid etc) at a particular position by using both the dry and wet transfer methods. Both methods used for transfer require a two step approach: lifting of the graphene from a substrate and precise transfer to another substrate using alignment procedures. The transferred graphene flakes were confirmed and analyzed by Raman spectroscopy and atomic force microscopy. Bubbles of a few nanometres in dimension containing hydrocarbon appear at the interface when graphene is transferred on BN. The annealing of these GBN structures results in large bubble free areas in the sample which are then suitable for device fabrication. A

close comparison of both wet and dry methods for transferring graphene flakes has been made showing that less bubbles appear in case of dry transfer however the success rate of flake transfer is more for wet method. The method of wet transfer has also been used to make TEM graphene samples. Transfer, using both dry and wet methods were used routinely not only for graphene, but other layered materials which can be exfoliated like BN, BSCOO, TaS_2, MoS_2 and mica. The electronic properties of graphene on hBN substrate have been studied in detail showing the highest ever achieved mobility for substrate based graphene [24,64]. Transfer techniques have been used to fabricate GBN heterostructures that allowed us to study ballistic transport [30], metal tuneable insulator transition in such systems [26] and also studies of field effect tunnelling transistor made from GBN layers [25].

The use of hBN as atomically flat substrate for graphene has increased the mobility μ of such devices as high as ~ 100,000 $cm^2V^{-1}S^{-1}$ at charge carrier density n~$10^{11}cm^{-2}$ [24] and these values yield the mean free path l ~ 1 μm. For these high quality devices no evidence of ballistic transport has been previously reported. In the last part of the thesis, the micrometre ballistic transport studies in a graphene layer sandwiched between two BN layers has been presented. We fabricated the GBN devices by transferring graphene on BN substrates and then encapsulating the devices by another BN layer which improves the environmental stability of GBN device. The measured devices exhibit room temperature μ > 100,000 $cm^2V^{-1}S^{-1}$ at low n ~ 10^{11} cm^{-2} and at higher n ~ 10^{12} cm^{-2} . The longitudinal conductivity of the devices was limited by the width of the device w =1 μm where the diffusive boundary scattering of charge carriers dominates rather than the bulk scattering in graphene. The bend resistance measurements were employed to study the ballistic transport in our devices. The negative bend resistance yields l over 1 μm indicating room temperature ballistic transport. At low temperature l reaches a value ~ 3 μm which translates into extremely high μ ~ 500,000 $cm^2V^{-1}S^{-1}$ mobility. The GBN devices with w > 5 μm working in diffusive regime are required to confirm such ultrahigh mobility at high charge carrier by conventional σ(n) measurements. The bubbles in GBN structures restrict the size of the device so efforts are in progress in minimize or get bubble free regions for further studies. Experiments have been made to confirm the nature/content of the bubbles. One possible solutions may include the pre annealing of BN substrate before depositing graphene on it, quick transfer of graphene to avoid the accumulation of hydrocarbons on BN surface or carrying the transfer process in a glove box.

References

[1] K. S. Novoselov, A. K. Geim, S. V. Morozov, D. Jiang, Y. Zhang, S. V. Dubonos, I. V. Grigorieva and A. A. Firsov, Science **306**, 666-69 (2004).

[2] J. Adams and D. Pendlebury, *Global Reserach Report Materials Science and Technology* (2011), pp. 1-16.

[3] "GRAF-TECH PROGRAMME," 2011. [Online] Available: http://www.ncbir.pl/gfx/ncbir/en/defaultaktualnosci/524/836/1/graftech.pdf.

[4] Cambridge IP, 2012. [Online] Available: http://www.cambridgeip.com/media/PR_CambridgeIP_Graphene-ReportonBoliven_Aprilupdate.pdf.Cambridge IP (2012).

[5] S. Bae, H. Kim, Y. Lee, X. Xu, J. S. Park, Y. Zheng, J. Balakrishnan, T. Lei, H. R. Kim, Y. I. Song, Y. J. Kim, K. S. Kim, B. Ozyilmaz, J. H. Ahn, B. H. Hong and S. Iijima, Nature Nanotechnology **5**, 574-78 (2010).

[6] Y. M. Lin, A. Valdes-Garcia, S. J. Han, D. B. Farmer, I. Meric, Y. Sun, Y. Wu, C. Dimitrakopoulos, A. Grill, P. Avouris and K. A. Jenkins, Science **332**, 1294-97 (2011).

[7] A. J. Hong, E. B. Song, H. S. Yu, M. J. Allen, J. Kim, J. D. Fowler, J. K. Wassei, Y. Park, Y. Wang, J. Zou, R. B. Kaner, B. H. Weiller and K. L. Wang, ACS Nano **5**, 7812-17 (2011).

[8] Z. Xu, G. Tai, Y. Zhou, F. Gao and K. H. Wong, arXiv:1203.0161v2 (2012).

[9] P. Blake, E. W. Hill, a. H. Castro Neto, K. S. Novoselov, D. Jiang, R. Yang, T. J. Booth and A. K. Geim, Applied Physics Letters **91**, 063124 (2007).

[10] R. V. Gorbachev, I. Riaz, R. R. Nair, R. Jalil, L. Britnell, B. D. Belle, E. W. Hill, K. S. Novoselov, K. Watanabe, T. Taniguchi, A. K. Geim and P. Blake, Small **7**, 465-68 (2011).

[11] K. S. Novoselov, D. Jiang, F. Schedin, T. J. Booth, V. V. Khotkevich, S. V. Morozov, and A. K. Geim, PNAS **102**, 10451-53 (2005).

[12] B. Radisavljevic, A. Radenovic, J. Brivio, V. Giacometti and A. Kis, Nature Nanotechnology **6**, 147-50 (2011).

[13] K. S. Novoselov, A. K. Geim, S. V. Morozov, D. Jiang, M. I. Katsnelson, I. V. Grigorieva, S. V. Dubonos and A. A. Firsov, Nature **438**, 197-200 (2005).

[14] A. K. Geim, K. S. Novoselov, S. V. Morozov, D. Jiang, Y. Zhang, S. V. Dubonos, I. V. Grigorieva and A. A. Firsov, Nature Materials **6**, 183-91 (2007).

[15] K. I. Bolotin, K. J. Sikes, Z. Jiang, M. Klima, G. Fudenberg, J. Hone, P. Kim and H. L. Stormer, Solid State Communications **146**, 351-55 (2008).

[16] Y.M. Lin, K. a Jenkins, A. Valdes-Garcia, J. P. Small, D. B. Farmer, P. Avouris, D. B. F. Yu-Ming Lin, Keith A. Jenkins, Alberto Valdes-Garcia and Joshua P. Small, Nano Letters **9**, 422-26 (2009).

[17] D. Y. Jeon, K. J. Lee, M. Kim, D. C. Kim, H.-J. Chung, Y. S. Woo and S. Seo, Japanese Journal of Applied Physics **48**, 091601 (2009).

[18] I. Meric, N. Baklitskaya, P. Kim, and K. L. Shepard, (IEDM) IEEE International 1-4 (2008).

[19] Y. Lin, C. Dimitrakopoulos, K. A. Jenkins, D. B. Farmer, H. Chiu, A. Grill and P. Avouris, Science **327**, 662 (2010).

[20] J. H. Chen, C. Jang, S. Xiao, M. Ishigami and M. S. Fuhrer, Nature Nanotechnology **3**, 206-9 (2008).

[21] S. Morozov, K. Novoselov, M. Katsnelson, F. Schedin, D. Elias, J. Jaszczak and A. K. Geim, Physical Review Letters **100**, 11-14 (2008).

[22] R. S. Shishir, D. K. Ferry, L. Fellow and S. M. Goodnick, IEEE 21-24 (2009).

[23] S. Fratini and F. Guinea, Physical Review B **77**, 1-6 (2008).

[24] C. R. Dean, A. F. Young, I. Meric, C. Lee, L. Wang, S. Sorgenfrei, K. Watanabe, T. Taniguchi, P. Kim, K. L. Shepard and J. Hone, Nature Nanotechnology **5**, 722-26 (2010).

[25] L. Britnell, R. V. Gorbachev, R. Jalil, B. D. Belle, F. Schedin, A. Mishchenko, T. Georgiou, M. I. Katsnelson, L. Eaves, S. V. Morozov, N. M. R. Peres, J. Leist, A. K. Geim, K. S. Novoselov and L. A. Ponomarenko, Science **335**, 947-50 (2012).

[26] L. a. Ponomarenko, a. K. Geim, a. a. Zhukov, R. Jalil, S. V. Morozov, K. S. Novoselov, I. V. Grigorieva, E. H. Hill, V. V. Cheianov, V. I. Fal'ko, K. Watanabe, T. Taniguchi and R. V. Gorbachev, Nature Physics **7**, 958-61 (2011).

[27] A. C. Ferrari, J. C. Meyer, V. Scardaci, C. Casiraghi, M. Lazzeri, F. Mauri, S. Piscanec, D. Jiang, K. S. Novoselov, S. Roth and A. K. Geim, Physical Review Letters **97**, 187401 (2006).

[28] A. Reina, H. Son, L. Jiao, B. Fan, M. S. Dresselhaus, Z. Liu and J. Kong, Journal of Physical Chemistry C **112**, 17741-44 (2008).

[29] W. Regan, N. Alem, B. Alemán, B. Geng, C. Girit, L. Maserati, F. Wang, M. Crommie and A. Zettl, Applied Physics Letters **96**, 113102 (2010).

[30] A. S. Mayorov, R. V. Gorbachev, S. V. Morozov, L. Britnell, R. Jalil, L. A. Ponomarenko, P. Blake, K. S. Novoselov, K. Watanabe, T. Taniguchi and A. K. Geim, Nano Letters **11**, 2396-99 (2011).

[31] K. Barnham and D. Vvedensky, *Low-Dimensional Semiconductor Structures: Fundamentals and Device Applications* (Cambridge University Press, 2008), pp. 1-393.

[32] "All Nobel Prizes in Physics." [Online] Available: http://www.nobelprize.org/nobel_prizes/physics/laureates/.

[33] P. R. Wallace, Phys. Rev. **71**, 622-34 (1947).

[34] J. C. Slonczewski and P. R. Wallace, Phys. Rev. **109**, 272-79 (1958).

[35] N. D. Mermin, Phys. Rev. **176**, 250-54 (1968).

[36] J. A. Venables, G. D. T. Spiller, and M. Hanbucken, Rep. Prog. Phys. **47**, 399-459 (1984).

[37] X. Du, I. Skachko, A. Barker and E. Y. Andrei, Nature Nanotechnology **3**, 491-95 (2008).

[38] B. G. Streetman and S. Banerjee, *Solid State Electronic Devices* (Pearson Prentice Hall, 2006), p. 581.

[39] A. Jorio, G. Dresselhaus, and M. S. Dresselhaus, *Topics in Applied Physics Volume III Carbon Nanotubes Advanced Topics in the Synthesis, Structure, Properties and Applications* (Springer Berlin Heidelberg, Berlin, Heidelberg, 2008), pp. 1-709.

[40] J. C. Charlier and S. Roche, Reviews of Modern Physics **79**, 677-732 (2007).

[41] J. C. Meyer, A. K. Geim, M. I. Katsnelson, K. S. Novoselov, T. J. Booth and S. Roth, Nature **446**, 60-63 (2007).

[42] A. J. Van Bommel, J. E. Crombeen and A. Van Tooren, Surface Science **48**, 463-72 (1975).

[43] C. Berger, Z. Song, T. Li, X. Li, A. Y. Ogbazghi, R. Feng, Z. Dai, A. N. Marchenkov, E. H. Conrad, P. N. First and W. A. D. Heer, Journal of Physical Chemistry B **108**, 19912-16 (2004).

[44] T. A. Land, T. Michely, R. J. Behm and J. C. Hemminger, Surface Science **264**, (1992).

[45] A. Nagashima, K. Nuka, H. Itoh, T. Ichinokawa and C. Oshima, Surface Science **291**, 93-98 (1993).

[46] J. Wintterlin and M. L. Bocquet, Surface Science **603**, 1841-52 (2009).

[47] X. Li, W. Cai, L. Colombo and R. S. Ruoff, Nano Letters **9**, 4268-72 (2009).

[48] N. O. Alexander, Nature Nanotechnology **4**, 212-13 (2009).

[49] C. Miao, C. Zheng, O. Liang, and Y. Hong Xie, in *Physics and Applications of Graphene-Experiments* (2011), p. 18.

[50] S. L. Hangstrom and G. A. Somorjai, Physical Review Letters **15**, 491-93 (1965).

[51] J. T. Grant and T. W. Haas, Surface Science **21**, 76-85 (1970).

[52] S. Chen, W. Cai, R. D. Piner, J. W. Suk, Y. Wu, Y. Ren, J. Kang and R. S. Ruoff, Nano Letters **11**, 3519-25 (2011).

[53] G. Nandamuri, S. Roumimov and R. Solanki, Nanotechnology **21**, 145604 (2010).

[54] K. S. Kim, Y. Zhao, H. Jang, S. Y. Lee, J. M. Kim, J. H. Ahn, P. Kim, J. Y. Choi and B. H. Hong, Nature **457**, 706-10 (2009).

[55] A. Reina, X. Jia, J. Ho, D. Nezich, H. Son, V. Bulovic, M. S. Dresselhaus and J. Kong, Nano Letters **9**, 30-35 (2009).

[56] J. W. Suk, A. Kitt, C. W. Magnuson, Y. Hao, S. Ahmed, J. An, A. K. Swan, B. B. Goldberg and R. S. Ruoff, ACS Nano **5**, 6916-24 (2011).

[57] W. S. Hummers, J R and E. O. Richard, J. Am. Chem. Soc., **80**, 1339 (1958).

[58] Y. Zhu, S. Murali, W. Cai, X. Li, J. W. Suk, J. R. Potts and R. S. Ruoff, Advanced Materials **22**, 3906-24 (2010).

[59] V. C. Tung, M. J. Allen, Y. Yang and R. B. Kaner, Nature Nanotechnology **4**, 25-29 (2009).

[60] C. Gómez-Navarro, J. C. Meyer, R. S. Sundaram, A. Chuvilin, S. Kurasch, M. Burghard, K. Kern and U. Kaiser, Nano Letters **10**, 1144-48 (2010).

[61] S. Pei and H. M. Cheng, Carbon **50**, 3210-28 (2012).

[62] M. Cheng, R. Yang, L. Zhang, Z. Shi, W. Yang, D. Wang, G. Xie, D. Shi and G. Zhang, Carbon **50**, 2581-87 (2012).

[63] P. Nemes-Incze, Z. Osvath, K. Kamaras and L.P. Biro, Carbon **46**, 1435-42 (2008).

[64] P. J. Zomer, S. P. Dash, N. Tombros and B. J. van Wees, Applied Physics Letters **99**, 232104 (2011).

[65] F. Schedin, A. K. Geim, S. V. Morozov, E. W. Hill, P. Blake, M. I. Katsnelson and K. S. Novoselov, Nature Materials **6**, 652-55 (2007).

[66] Y. Zhang, Y. W. Tan, H. L. Stormer and P. Kim, Nature **438**, 201-4 (2005).

[67] K. S. Novoselov, Z. Jiang, Y. Zhang, S. V. Morozov, H. L. Stormer, U. Zeitler, J. C. Maan, G. S. Boebinger, P. Kim and A. K. Geim, Science **315**, 1379 (2007).

[68] A. A. Balandin, S. Ghosh, W. Bao, I. Calizo, D. Teweldebrhan, F. Miao and C. N. Lau, Nano Letters **8**, 902-07 (2008).

[69] A. A Balandin, Nature Materials **10**, 569-81 (2011).

[70] F. Bonaccorso, Z. Sun, T. Hasan and A. C. Ferrari, Nature Photonics **4**, 611-22 (2010).

[71] C. Lee, X. Wei, J. W. Kysar and J. Hone, Science **321**, 385-88 (2008).

[72] T. Ramanathan, A. A. Abdala, S. Stankovich, D. A. Dikin, M. Herrera-Alonso, R. D. Piner, D. H. Adamson, H. C. Schniepp, X. Chen, R. S. Ruoff, S. T. Nguyen, I. A Aksay, R. K. Prud'Homme and L. C. Brinson, Nature Nanotechnology **3**, 327-31 (2008).

[73] R. A. Barton, J. Parpia and H. G. Craighead, Journal of Vacuum Science & Technology B: Microelectronics and Nanometer Structures **29**, 050801 (2011).

[74] R. R. Nair, P. Blake, A. N. Grigorenko, K. S. Novoselov, T. J. Booth, T. Stauber, N. M. R. Peres and A. K. Geim, Science **320**, 1308 (2008).

[75] X. Li, Y. Zhu, W. Cai, M. Borysiak, B. Han, D. Chen, R. D. Piner, L. Colombo and R. S. Ruoff, Nano Letters **9**, 4359-63 (2009).

[76] Z. Luo, P. M. Vora, E. J. Mele, a. T. C. Johnson, and J. M. Kikkawa, Applied Physics Letters **94**, 111909 (2009).

[77] G. Eda, Y. Y. Lin, C. Mattevi, H. Yamaguchi, H. A. Chen, I. S. Chen, C. W. Chen and M. Chhowalla, Advanced Materials **22**, 505-09 (2010).

[78] Y. Wu, Y. Ming Lin, A. A. Bol, K. A. Jenkins, F. Xia, D. B. Farmer, Y. Zhu and P. Avouris, Nature **472**, 74-78 (2011).

[79] T. Mueller, F. Xia and P. Avouris, Nat. Photon **4**, 297-301 (2010).

[80] "Graphene: Technologies, Applications, and Markets ." [Online] Available: http://www.bccresearch.com/report/AVM075A.html.

[81] K. Tahy, T. Fang, P. Zhao, A. Konar, C. Lian, H. G. Xing, M. Kelly and D. Jena, in *Physics and Applications of Graphene-Experiments* (2011), p. 28.

[82] Y. Lin, C. Dimitrakopoulos, K. A. Jenkins, D. B. Farmer, H. Chiu, A. Grill, and P. Avouris, Science **321,** 622 (2010).

[83] T. Placios, A. Hsu, and H. Wang, Institute of Electrical and Electronics Engineers **6**, 122-28 (2010).

[84] L. Liao, Y. C. Lin, M. Bao, R. Cheng, J. Bai, Y. Liu, Y. Qu, K. L. Wang, Y. Huang, and X. Duan, Nature **467**, 305-08 (2010).

[85] L. Liao and X. Duan, Materials Science and Engineering Reports **70**, 354-70 (2010).

[86] L. Liao, J. Bai, Y. Qu, Y. Chen Lin, Y. Li, Y. Huang and X. Duan, PNAS 1-5 (2010).

[87] F. Schwierz, Nature Nanotechnology **5**, 487-96 (2010).

[88] M. W. Lin, C. Ling, Y. Zhang, H. J. Yoon, M. M.-C. Cheng, L. a Agapito, N. Kioussis, N. Widjaja and Z. Zhou, Nanotechnology **22**, 265201 (2011).

[89] F. Xia, D. B. Farmer, Y. M. Lin and P. Avouris, Nano Letters **10**, 715-18 (2010).

[90] C. Liu, Z. Yu, D. Neff, A. Zhamu, and B. Z. Jang, Nano Letters **10**, 4863-68 (2010).

[91] J. R. Miller, R. a Outlaw, and B. C. Holloway, Science **329**, 1637-39 (2010).

[92] Y. Zhu, S. Murali, M. D. Stoller, K. J. Ganesh, W. Cai, P. J. Ferreira, A. Pirkle, R. M. Wallace, K. A. Cychosz, M. Thommes, D. Su, E. A. Stach and R. S. Ruoff, Science **1537**, (2011).

[93] X. Zhao, C. M. Hayner, M. C. Kung and H. H. Kung, Advanced Energy Materials **1**, (2011).

[94] H. Kim, S. Wook Kim, J. Hong, H. Dae Lim and S. Kim, Journal of The Electrochemical Society **158**, 930-35 (2011).

[95] M. Grundmann, *The Physics of Semiconductors*, Second (Springer Berlin Heidelberg, Berlin, Heidelberg, 2010), pp. 235-63.

[96] A. H. C. Neto, Reviews of Modern Physics **81**, 110-55 (2009).

[97] S. Franssila, *Introduction to Microfabrication (Google eBook)* (John Wiley and Sons, 2010), p. 534.

[98] M. Engineering, Microelectronic Engineering **6**, 77-84 (1987).

[99] H. Alloul and S. Translated by :Lyle, in *Introduction to the Physics of Electrons in Solids* (Springer-Verlag Berlin Heidelberg, 2011), pp. 111-33.

[100] M. O. Goerbig, arXiv:0909.1998v2 (2009).

[101] L. A. Ponomarenko, R. Yang, T. M. Mohiuddin, M. I. Katsnelson, K. S. Novoselov, S. V. Morozov, A. A. Zhukov, F. Schedin, E. W. Hill and A. K. Geim, Physical Review Letters **102**, 2066031-34 (2009).

[102] Z. H. Ni, L. A. Ponomarenko, R. R. Nair, R. Yang, S. Anissimova, I. V. Grigorieva, F. Schedin, P. Blake, Z. X. Shen, E. H. Hill, K. S. Novoselov and A. K. Geim, Nano Letters **10**, 3868-72 (2010).

[103] E. Hwang, S. Adam and S. Sarma, Physical Review Letters **98**, 2-5 (2007).

[104] J. H. Chen, C. Jang, S. Adam, M. S. Fuhrer, E. D. Williams and M. Ishigami, Nature Physics **4**, 377-81 (2008).

[105] E. H. Hwang and S. D. Sarma, Physical Review B **77**, 6 (2007).

[106] M. I. Katsnelson and A. K. Geim, Philosophical Transactions. Series A, Mathematical, Physical, and Engineering Sciences **366**, 195-204 (2008).

[107] M. Ishigami, J. H. Chen, W. G. Cullen, M. S. Fuhrer and E. D. Williams, Nano Letters **7**, 1643-48 (2007).

[108] C. H. Lui, L. Liu, K. F. Mak, G. W. Flynn and T. F. Heinz, Nature **462**, 339-41 (2009).

[109] R. Decker, Y. Wang, V. W. Brar, W. Regan, H. Zon Tsai, Q. Wu, W. Gannett, A. Zettl and M. F. Crommie, Nano Letters **11**, 2291-95 (2011).

[110] K. Watanabe, T. Taniguchi and H. Kanda, Nature Materials **3**, 404-09 (2004).

[111] R. E. Peierls, Ann. Inst. Henri Poincare **5**, (1935).

[112] L.D. Landau and E.M. Lifshitz, "Statistical Physics Part I Pergamon, oxford," 1980, Secs. 137 and 138.

[113] H. O. Pierson, *Handbook of Refractory Carbides and Nitrides: Properties, Characteristics, Procrssing and Applications* (Noyes publications, 1996).

[114] H. O. Pierson, *Handbook of Carbon, Graphite, Diamond and Fullerenes, Noyes Publications, Park Ridge, NJ(1993).*

[115] C. H. R. Geick and Perry, Physical Review **146**, 543-47 (1966).

[116] T. Taniguchi and K. Watanabe, Journal of Crystal Growth **303**, 525-29 (2007).

[117] "Cubic boron nitride." [Online] Available : http://www.nano-ss.com/index.php?option=com_content&view=article&id=10&Itemid=77&lang=en

[118] L. Britnell, R. V. Gorbachev, R. Jalil, B. D. Belle, F. Schedin, M. I. Katsnelson, L. Eaves, S. V. Morozov, A. S. Mayorov, N. M. R. Peres, A. H. C. Neto, J. Leist, A. K. Geim, L. A. Ponomarenko, K. S. Novoselov and A. H. Castro Neto, Nano Letters **12**, 1707-10 (2012).

[119] S. Stankovich, D. A. Dikin, G. H. B. Dommett, K. M. Kohlhaas, E. J. Zimney, E. A. Stach, R. D. Piner, S. T. Nguyen and R. S. Ruoff, Nature **442**, 282-86 (2006).

[120] T. Ando, Journal of the Physics Society Japan **75**, 74716 (2006).

[121] M. Lundstrom, *Fundamentals of Carrier Transport* (Cambridge University Press, 2000), p. 440.

[122] D. K. Ferry, *Quantum Transport in Ultrasmall Devices* (Plenum Press, 1995), p. 544.

[123] T. Ihn, *Semiconductor Nanostructures: Quantum States and Electronic Transport* (Oxford University Press, 2009), p. 552.

[124] R. Landauer, IBM Journal of Research and Development **32**, 306-16 (1988).

[125] M. Buttiker, Physical Review Letters **57**, 6-9 (1986).

[126] G. L. Timp and R. E. Howard, Proceedings of the IEEE **79**,1188-1207 (1991).

[127] L. J. Van Der Pauw, Philips Technical Review **20**, 220-24 (1958).

[128] P. Blake, R. Yang, S. V. Morozov, F. Schedin, L. a. Ponomarenko, A. A. Zhukov, R. R. Nair, I. V. Grigorieva, K. S. Novoselov and A. K. Geim, Solid State Communications **149**, 1068-1071 (2009).

[129] F. Chen, J. Xia, D. K. Ferry and N. Tao, Nano Letters **9**, 2571- 74 (2009).

[130] R. S. Shishir and D. K. Ferry, Journal of Physics: Condensed Matter **21**, 344201 (2009).

Appendix

List of Publications

1. L. Britnell, R. V. Gorbachev, **R. Jalil**, B. D. Belle, F. Schedin, M. I. Katsnelson, L. Eaves, S. V. Morozov, A. S. Mayorov, N. M. R. Peres, A. H. C. Neto, J. Leist, A. K. Geim, L. A. Ponomarenko, K. S. Novoselov and A. H. Castro Neto " Electron tunneling through ultrathin boron nitride crystalline barriers" *Nano Letters* **12**, 1707-10 (2012).
2. V. G. Kravets, F. Schedin, **R. Jalil**, L. Britnell, K. S. Novoselov and A. N. Grigorenko "Surface Hydrogenation and Optics of a Graphene Sheet Transferred onto a Plasmonic Nanoarray"*J. Phys. Chem. **C**.* **116**, 3882-3887 (2012).
3. L. Gong, R. J. Young, I. A. Kinloch, I. Riaz, **R. Jalil** and K. S. Novoselov "Optimizing the Reinforcement of Polymer-Based Nanocomposites by Graphene" *ACS Nano* **6**, 2086-2095 (2012).
4. L. Britnell, R. V. Gorbachev, **R. Jalil**, B. D. Belle, F. Schedin, A. Mishchenko, T. Georgiou, M. I. Katsnelson, L. Eaves, S. V. Morozov, N. M. R. Peres, J. Leist, A. K. Geim, K. S. Novoselov and L. A. Ponomarenko "Field-Effect Tunneling Transistor Based on Vertical Graphene Heterostructures" *Science* **335**, 947-950 (2012).
5. C. Pan, R. Nair, U. Bangert, Q. Ramasse, **R. Jalil**, R. Zan, C. Seabourne and A. Scott "Nano scale electron diffraction and plasmon spectroscopy of single and few-layer boron nitride" *Physical Review* **B** 85, 1-7 (2012).
6. R. G. S. J. Haigh, A. Gholinia, **R. Jalil**, S. Romani, L. Britnell, D.C. Elias, K. S. Novoselov, L. A. Ponomarenko and A. K. Geim "Graphene-based heterostructures and superlattices: Cross-sectional imaging of individual layers and buried interfaces"Accepted; *Nat. Mat*. (2012).
7. Otakar Frank, Milan Bousa, Ibtsam Riaz, **Rashid Jalil**, Kostya S. Novoselov, Georgia Tsoukleri, John Parthenios, Ladislav Kavan, Konstantinos Papagelis and Costas Galiotis “Phonon and structural changes in deformed Bernal stacked bilayer graphene” *Nano Letters* **12**(2), 687 – 693(2012).

8. A. S. Mayorov, R. V. Gorbachev, S. V. Morozov, L. Britnell, **R. Jalil**, L. A Ponomarenko, P. Blake, K. S. Novoselov, K. Watanabe, T. Taniguchi and A. K. Geim "Micrometer-Scale Ballistic Transport in Encapsulated Graphene at Room Temperature" *Nano Letters* **11**, 2396-9 (2011).
9. R. J. Young, L. Gong, I. A. Kinloch, I. Riaz, **R. Jalil** and K. S. Novoselov "Strain mapping in a graphene monolayer nanocomposite" *ACS Nano* **5**, 3079-84 (2011).
10. L. A. Ponomarenko, A. K. Geim, A. A. Zhukov, **R. Jalil**, S. V. Morozov, K. S. Novoselov, I. V. Grigorieva, E. H. Hill, V. V. Cheianov, V. I. Fal'ko, K. Watanabe, T. Taniguchi and R. V. Gorbachev "Tunable metal–insulator transition in double-layer graphene heterostructures" *Nature Physics* 7, 958-961 (2011).
11. O. Frank, M. Mohr, J. Maultzsch, C. Thomsen, I. Riaz, **R. Jalil**, K. S. Novoselov, G. Tsoukleri, J. Parthenios, K. Papagelis, L. Kavan and C. Galiotis "Raman 2D-band splitting in graphene: theory and experiment" *ACS Nano* **5**, 2231-9 (2011).
12. R. V. Gorbachev, I. Riaz, R. R. Nair, **R. Jalil**, L. Britnell, B. D. Belle, E. W. Hill, K. S. Novoselov, K. Watanabe, T. Taniguchi, A. K. Geim and P. Blake "Hunting for monolayer boron nitride: optical and Raman signatures" *Small* **7**, 465-8 (2011).
13. V. G. Kravets, R. R. Nair, P. Blake, L. A. Ponomarenko, I. Riaz, **R. Jalil**, S. Anisimova, A. N. Grigorenko, K. S. Novoselov and A. K. Geim in Physical Properties of Nanosystems, edited by J. Bonca and S. Kruchin (SPRINGER, PO BOX 17, 3300 AA DORDRECHT, NETHERLANDS, 2011),pp. 3-9.
14. O. Frank, G. Tsoukleri, J. Parthenios, K. Papagelis, I. Riaz, **R. Jalil**, K. S. Novoselov and C. Galiotis "Compression behavior of single-layer graphenes" *ACS Nano* **4**, 3131-8 (2010).
15. R. R. Nair, W. Ren, **R. Jalil**, I. Riaz, V. G. Kravets, L. Britnell, P. Blake, F. Schedin, A. S. Mayorov, S. Yuan, M. I. Katsnelson, H.-M. Cheng, W. Strupinski, L. G. Bulusheva, A. V. Okotrub, I. V. Grigorieva, A. N. Grigorenko, K. S. Novoselov and A. K. Geim "Fluorographene: a two-dimensional counterpart of teflon" *Small* **6**, 2877-84 (2010).
16. L. Gong, I. A. Kinloch, R. J. Young, I. Riaz, **R. Jalil** and K. S. Novoselov "Interfacial stress transfer in a graphene monolayer nanocomposite" *Advanced Materials* **22**, 2694-7 (2010).
17. T. Mohiuddin, A. Lombardo, R. Nair, a. Bonetti, G. Savini, **R. Jalil**, N. Bonini, D. Basko, C. Galiotis, N. Marzari, K. Novoselov, A. K. Geim and A. C. Ferrari

"Uniaxial strain in graphene by Raman spectroscopy: G peak splitting, Gruneisen parameters, and sample orientation" *Physical Review* **B 79**, 1-8 (2009).

18. G. Tsoukleri, J. Parthenios, K. Papagelis, **R. Jalil**, A. C. Ferrari, A. K. Geim, K. S. Novoselov and C. Galiotis "Subjecting a graphene monolayer to tension and compression" *Small* **5**, 2397-402 (2009).
19. M. S. Rafique, M. Khaleeq-Ur-Rahman, I. Riaz, **R. Jalil**, and N. Farid "External magnetic field effect on plume images and X-ray emission from a nanosecond laser produced plasma" *Laser and Particle Beams* **26**, 217-224 (2008).